Interaction of cosmic particles with matter

from volcanoes to satellites

PhD Thesis

Gábor Galgóczi
ELTE Doctoral School of Physics
Wigner Research Centre

Supervisor:

Dezső Varga PhD
Wigner Research Centre

27/05/2023, Budapest

Contents

1 Prologue

This PhD dissertation covers the interaction of cosmic particles with matter from satellites to muography. The common theme among the sections is understanding how particles interact with particle detectors. Six topics are covered: three describes the residual background and the signal to noise ratio in satellites. One covers the residual background in volcano muography. The fifth one describes a novel material analysis method using cosmic muons. The last topic covers the residual background in a novel neutron detector.

The exponential growth of the microelectronics industry in the twenty-first century made it possible to develop cost affordable and sufficiently small particle detectors and read out electronics for scientific researchers to open new frontiers in high energy particle physics.

The idea of using cosmic muons to reveal the inner structure of large scale objects (muography) is not new. Luis Alvarez in the 1960s proved that muons can be used to determine the inner structure of the second pyramid of Giza. He utilized the so called spark chambers. Since then several other detector types have proven their capability of measuring cosmic muons.

In recent years the focus of the muography community has remained on the study of volcanoes. Forecast of volcano eruptions has so far relied on seismological and topographical data. With the help of muography the inner structure of the volcanoes and the state of the magma chamber can be understood. This poses a novel challenge since due to the changing dynamic of the volcano time resolution is needed.

Our research group at the Wigner Research Centre has developed a cost effective detector system Muography Observatory System (MOS). It consists of several multi-wire chambers and lead absorbers between them to suppress particle background. Several of these systems have been monitoring the Sakurajima volcano in Japan for $\sim$4 years. We have proven that the detector is capable of revealing changes of the inner structure of the volcano. As described in *Section 2.* we have developed an artificial intelligence tool to further suppress the current particle background in order to achieve a higher signal-to-noise ratio.

Our research group works together with the group led by prof. Bikit at the University of Novi Sad developed a novel concept for material analysis with cosmic muons. In *Section 3.* I describe how we have proven that cosmic muons crossing a target produce different amounts of electrons and gamma-ray depending on the density and the atomic number of the material. This novel technique could be used to analyze the material composition of objects which contain metal (therefore can not be investigated by X-rays) and can not be irradiated with hadrons due to activation concerns, eg. meteorites.

Cosmic rays are widely studied in astrophysics as well as a tool to understand the high-energy universe. In recent years the detection of $\sim$ 100 gravitational waves led to the renaissance of high energy astrophysics since the afterglow of the neutron-neutron (or black hole-neutron star) star mergers provides additional information on the source of the waves. Since the atmosphere is not transparent to gamma-ray, satellites with expensive large detectors were developed. Until recent years there were only a handful of satellites equipped with gamma-ray detectors. Due to the fact that gamma-rays are hard to focus and have a long mean free path in material the angle resolution of these detectors is very low.

In recent years several private entities have started to offer space for CubeSats on their rockets for Low Earth Orbit (LEO). This has pushed down the cost of sending a small satellite to orbit to $\sim$ 100 000 \$. This has made launching satellites affordable and therefore led to a "space race" for scientific missions. Currently there are several collaborations working on CubeSats for the detection of gamma-ray transient sources. An international collaboration led by Prof Werner consisting of Czech, Japanese, Slovak and Hungarian researchers developed and launched one of the first of such satellites called GRBAlpha which is the precursor of the planned CAMELOT mission.

In *Section 4.* I describe how we have proven that such CubeSats are able to detect several astrophysical transient sources. GRBAlpha and CAMELOT satellites both rely on novel solid state detectors called Multi-Pixel Photon Counters (MPPCs). These are coupled to dense CsI(Tl) scintillators in which optical photons are created by extraterrestrial gamma-rays. Due to their limited size and weight new challenges have emerged. Older satellites were protected from high energy proton induced activation with shielding which can not be included in our satellites. Therefore it is a must to understand the level of activation and its contribution to the background.

In *Section 5.* I describe the software toolkit for the simulation of activation background for high energy detectors onboard satellites that I have developed. The framework employs direct Monte Carlo and analytical calculations allowing computations two orders of magnitude faster and more precise than a direct Monte Carlo simulation. The framework was developed in a way that the model of the satellite can be replaced easily. Therefore the framework can be used for different satellite missions. As an example, the proton induced activation background of the HERMES CubeSat is quantified.

Not only CubeSats but also flagship missions face background issues. For example, 40% of observations of the XMM-Newton telescope is significantly contaminated by soft proton induced background flares. It was not foreseen that protons with very low kinetic energy can scatter through the X-ray optics into the detector of the satellite. In order to minimize the background from

such low-energy protons for the next generation of flagship X-ray satellites: Advanced Telescope for High ENergy Astrophysics (ATHENA) introduced a novel concept, the so called Charged Particle Diverter (CPD). It is an array of magnets in a Hallbach design, which deflects protons below 76 keV before they would hit the Wide Field Imager (WFI) detector. In *Section 6.* I describe how I have proved that the level of background "leaking" into the detectors will be below the required level.

Residual background has to be taken into account at the several detectors which were designed for the cutting edge neutron source, located at the European Spallation Source European Research Infrastructure Consortium (ESS ERIC). It is currently under construction in Lund, Sweden, and aspires to become the most powerful pulsed neutron source in the world. The produced neutrons are destined to serve a variety of instruments for reflectometry, diffraction, spectrometry and imaging purposes. Reflectometry is an experimental technique present at every neutron source. Hence, two of the first instruments approved for construction at ESS are reflectometers. It is expected that the peak instantaneous rate of the neutron detectors could reach 100 kHz/mm which causes new challenges. In *Section 7.* I describe in my work how I have quantified the background of the planned detectors due to the scattering of neutrons on different parts of this novel detector.

2 Background suppression for volcano muography with machine learning

2.1 Muography of volcanoes

Muography (imaging with "cosmic" muons) was applied to a large-scale structure first in the 1960's by Luis W. Alvarez [1]. He proved that muons can be used to determine the inner structure of the pyramids by measuring the muon flux and calculating expected one. The excess in flux can be attributed to voids in the structure where the material does not absorb muons.

The muons utilized are called "cosmic" because they are created as a result of the interaction of high energy protons with the upper atmosphere. These collisions yield air showers that mostly consist of hadronic cascades. The end product of these interactions contain kaons and pions which then decay into muons in the following processes:

$\pi^{\pm} \longrightarrow \mu^{\pm} + \nu_{\mu}/\overline{\nu}_{\mu}$
$K^{\pm} \longrightarrow \mu^{\pm} + \nu_{\mu}/\overline{\nu}_{\mu}$
$K_L \longrightarrow \pi^{\pm} + e^{\pm} + \nu_e/\overline{\nu}_e$
$K_L \longrightarrow \pi^{\pm} + \mu^{\pm} + \nu_{\mu}/\overline{\nu}_{\mu}$
$K_S \longrightarrow \pi^{+} + \pi^{-}$

The energy spectrum of the muons depends on the zenith angle as can be seen in figure 1. Since the amount of air the muons need to pass through is the least from the zenith, the spectrum will be the softest in that case. Gaisser et al. [2] derived the "classic", probably currently most used model for muon energy spectrum as follows:

$$\frac{dN_{\mu 0}}{dE_{\mu 0}d\Omega} \approx \frac{0.14E_{\mu 0}^{2.7}}{cm^2srsGeV}\left\{\frac{1}{1+\frac{1.1E_{\mu 0}cos\theta}{115}} + \frac{0.054}{1+\frac{1.1E_{\mu 0}cos\theta}{850}}\right\} \tag{1}$$

where $E_{\mu 0}$ is the measured muon energy in units of GeV and Ω is the angle between the incoming particle and the normal of the upper atmospheric layer. However for the low energy regime ($\leq$ 100 GeV) this model overestimates the number of muons. Tang et al. [3] modified the model because of the latter reason and the original one ignored the curvature of the atmosphere, which causes deviations at large zenith angles.

$$\frac{dN_{\mu 0}}{dE_{\mu 0}d\Omega} \approx A\frac{0.14E_{\mu 0}^{\gamma}}{cm^2srsGeV}\left\{\frac{1}{1+\frac{1.1\bar{E}_{\mu 0}cos\theta^*}{115}} + \frac{0.054}{1+\frac{1.1\bar{E}_{\mu 0}cos\theta^*}{850}} + r_c\right\} \tag{2}$$

,

where γ is the power index and A is the overall scaling factor. r_c is the ratio of prompt muons to pions.

$$cos\theta^* = \sqrt{\frac{(cos\theta)^2 + p_1^2 + p_2(cos\theta)^{p_3} + p_4(cos\theta)^{p_5}}{1 + p_1^2 + p_2 + p_4}} \tag{3}$$

where p_1=0.102573, p_2=-0.068287, p_3=0.958633, p_4=0.0407253, and p_5=0.817285.

$\bar{E}_\mu 0 = E_\mu 0 + 2.06 \cdot 10^{-3}\left(\frac{950}{cos\theta^* - 90}\right)$. The value of r_c and A depends on the muon energy as follows:

	A	r_c	$E_{\mu 0}$
$100cos\theta^{*-1} < E_{\mu 0}$ GeV	1	0	$E_{\mu 0}$
$cos\theta^{*-1} \leq E_{\mu 0} < 100cos\theta^{*-1}$ GeV	$1.1\left(\frac{90\sqrt{cos\theta+0.001}}{1030}\right)^{\frac{4.5}{E_{\mu 0}cos\theta^*}}$	10^{-4}	$E_{\mu 0}$
$E_{\mu 0} < cos\theta^{*-1}$ GeV	$1.1\left(\frac{90\sqrt{cos\theta+0.001}}{1030}\right)^{\frac{4.5}{E_{\mu 0}cos\theta^*}}$	10^{-4}	$\frac{3E_{\mu 0} - 7sec\theta^*}{10}$

Muons interact with material through four interactions. Ionization, Bremsstrahlung, pair production and photonuclear interactions. The cross-section of these processes depends on the muon energy. For medium and lower energy muons (<300 GeV) the energy loss is mainly due to ionization (see fig. 30).

Muography uses the absorption of cosmic muons in order to determine the amount of material the muon has passed through similar to an X-ray device. For a large scale object one needs to calculate the average density of the object and the length the muon travels in it. Assuming that the muon loses energy by only ionization the continuoes slowing down approximation [4] can be applied to calculate the energy the muon will lose. Assuming that all muons with an initial energy larger than the latter will pass through the object one can calculate the expected flux by integrating the initial muon spectrum from the cutoff. Subtracting the expected flux from the measured one we can derive how much material is missing from the large scale objects, eg. hidden chambers in pyramids or magma chambers in volcanoes.

Muographic images have been taken of several volcanoes and in recent years this technique proved that it is capable of showing changes in volcanoes before and after an eruption. Asama, Japan [5], Satsuma-Iwojima, Japan [6], Showa-shinzan, Japan [7], Usu, Japan [8], Unzen, Japan [9], La Sourfiere, France [10], Puy de Dome, France [11], Stromboli, Italy [12] and Etna, Italy [13].

In general there are three main detector types that are being used in muography of large scale objects: scintillators, gaseous detectors and nuclear emulsion detectors. The latter one is the best choice when time resolution is not needed. Nuclear emulsion does not require any kind of on site support,

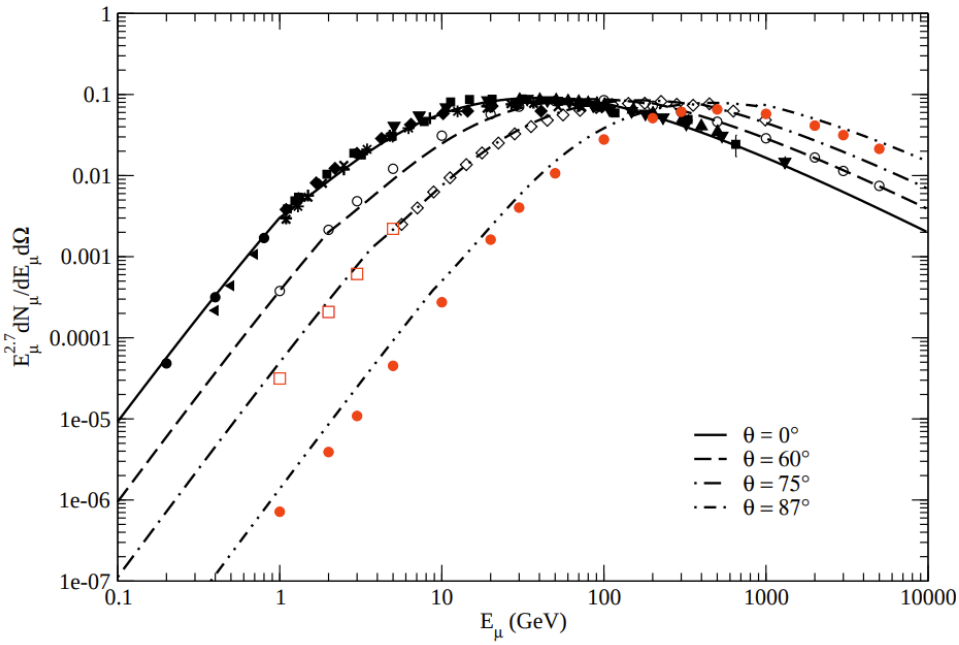

Figure 1: Cosmic muon spectrum for different zenith angles [3]. Muons coming from the zenith have a softer energy as they have to cross less air.

no electricity and no inert gas. They can be left at any place for months and once collected read out layer by layer. Gas detectors are generally lighter and cheaper compared to scintillator detectors. They can also be transported easier. Their only drawback is that they require constant gas flow. Our group has proven that the gas flow can be reduced to ≤ 1 lh^{-1} making it possible to operate for months without human intervention. Although there are a few applications, eg. borehole detector where only scintillators can be considered with the current technology.

Our research group has developed a detector system called Muography Observation System (MOS) [14, 15]. There are 7-9 multi-Wire Proportional Chambers (MWPCs) which register the direction of the incoming particles. Each detector has a set of wires in one direction and a set of pads segmented in the other one. This way we cost-effectively register the 1D projection of the track in both directions. In most cases Argon-Carbon dioxide gas is used in the detectors. Between the MWPC detectors a set of lead absorbers are placed. This is needed for background suppression which is detailed in the following subsection.

More than ten detectors of our group have been working on-site at the Sakurajima volcano providing insight into the volcano [17]. The system has

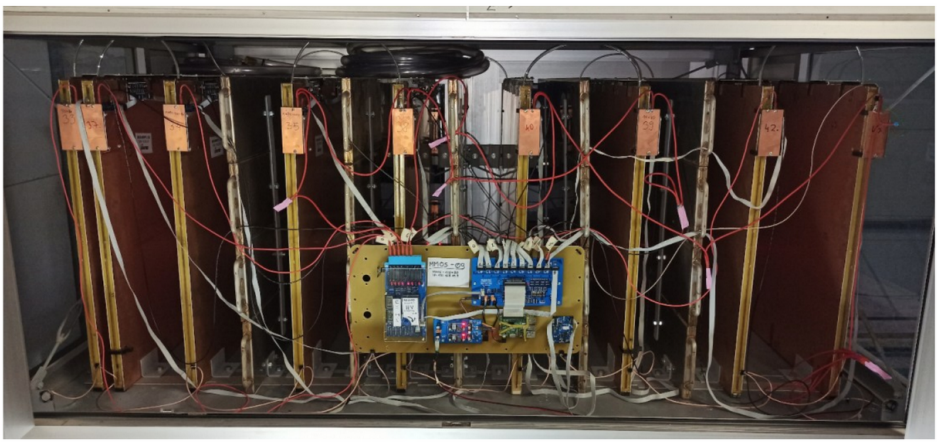

Figure 2: The MOS-09 system working at the Sakurajima volcano. 9 MWPC detectors and 5 lead absorbers are visible together with the readout electronics.

captured the formation of a volcanic plug beneath the Showa crater using only muography [16].

2.2 Determining flux from measurements

In order to obtain the material composition of a target we need to understand the flux of muons for a specific direction. Furthermore we need to calculate the acceptance and the tracking efficiency of our detector system. In the previous subsection we described how the expected flux can be calculated. In this subsection we detail the relevant detector effects. The number of detected muons are the following:

$$N = FtA_{eff}\Omega\tau, \tag{4}$$

where N is the detected muons, F is the flux of muons, t is the measurement time, A_{eff} is the effective detector area and Ω is the solid angle. τ is the live versus dead time ratio, which was 1 in our case as there are few triggers each second and dead time is below 1 ms. A_{eff} was not calculated from theory but from the measurements. This was needed as A_{eff} can change due to dead channels or any misalignment of the detectors. The detection efficiency of each wire is calculated one by one. Then in each solid angle pixel the detector efficiency of all possible hit wires is integrated out. The effective area of the MOS-08 detector system that this work uses is plotted in figure 3.

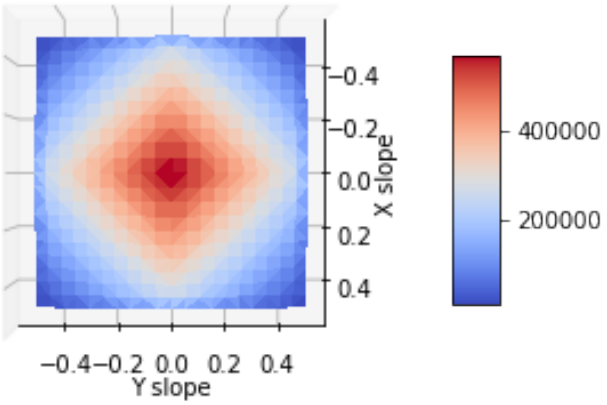

Figure 3: Effective area of the MOS-08 detector system in mm^2 depending on the direction of the incoming muon.

2.3 Background sources in volcano muography

Background suppression in muography is an exceptionally important field, since the most important volumes of the volcanoes are not close to the surface but at a depth of $\sim$ 1 km. Only a fraction ($\sim$ 1 %) of muons have enough energy to go through 1 km of material. Nishiyama et al showed that [18] the background consists mostly of protons, electrons and scattered muons. The spectra can be seen in figure 4. The bottom left subfigure shows the spectra for the thinner part of the volcano while the right one for the thicker part. There is almost no background above 1 GeV. While most of the penetrating muons (the signal) start around 2-10 GeV depending on the thickness of the traversed rock. Therefore if we could distinguish between particles below 1 GeV and above, we would almost completely suppress the background.

There were several attempts to understand and minimize the background particles. Rodriguez et al. [20] utilized TOF to distinguish between different particles and different energy ranges for muons. They have concluded that the electromagnetic background has a median energy of 0.3 GeV while the median energy for muons is $\sim$ 3 GeV. Protons have two orders of magnitude lower flux than muons in the 1-100 GeV energy range.

Unfortunately muons are not only absorbed by the volcano but are also

scattered. This blurs out the muography images and also adds background since low energy muons $\sim$ 1 GeV can scatter around 15°. Gómez et al. has shown [21] that high energy muons which are our signal scatter far less than 1°. Their results show that 22.70% of muons below 5 GeV with an incidence zenith angle greater than 85° will undergo forward scattering while 30% of them will scatter more than 5° in the azimuth angle.

The amount of scattering of muons strongly depends on their energy. Fig. 30 shows the cross-section of all possible interactions. For lower to medium energy muons, multiple Coulomb scattering is the leading cause of scattering. The probability density function of scattering is described by the Molière theory [22], which is roughly a Gaussian,

$$\frac{dN}{d\alpha} = \frac{1}{\sqrt{2\pi}\alpha_{MS}} e^{-\frac{\alpha^2}{2\alpha_{MS}^2}} \tag{5}$$

probability density function is symmetrical as expected and it is centered around zero, having a standard deviation α_{MS}:

$$\alpha_{MS} = \frac{13.6MeV}{\beta cp} Q \sqrt{\frac{x}{X_0}} \left(1 + 0.038 ln\left(\frac{x}{X_0}\right)\right) \tag{6}$$

β is the relativistic factor, x is the material thickness, p is the muon momentum and Q is the absolute electric charge of the muon. α_{MS} also depends on the radiation length (X_0) which is empirically given by

$$X_0 \approx \frac{716.4\frac{g}{cm^2}}{\rho} \frac{A}{Z(Z+1)log\left(\frac{287}{\sqrt{Z}}\right)} \tag{7}$$

with Z and A the atomic and mass numbers respectively and ρ is the material density.

Our research group designed the MOS system with a total of 10 cm of lead for background suppression. Assuming the background in fig. 4 this amount of material is sufficient to stop all electrons (3 cm CSDA range for 500 MeV energy) and scatter ones with higher energy to be thrown away by the tracking algorithm. For protons the maximum possible background energy is 1 GeV. The respective stopping power for these protons is 1.186 MeVcm^{2}g^{-1}. Therefore they can penetrate 10 cm lead and still have 750 MeV energy. Since they interact mostly through ionization as muons they will behave similarly. The main difference is that they are less relativistic due to their higher rest mass. Therefore they scatter more inside the detectors according to eq. 6 and behave similarly to low energy muons.

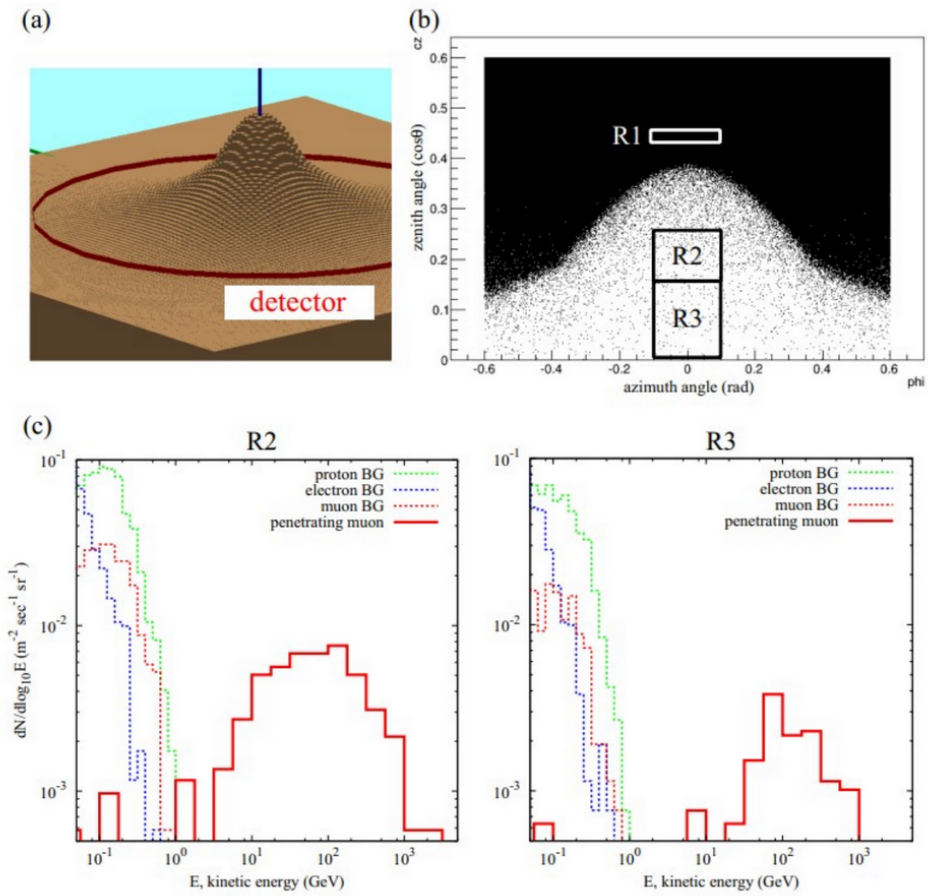

Figure 4: (a) Virtual mountain and detector constructed in GEANT4 computational space. (b) Angular distribution of particles arriving at the virtual detector, showing three angular regions R1, R2 and R3 defined for quantitative analysis. (c) Number histogram of particles arriving at the virtual detector. The energy distributions of the penetrating muons and background (BG) particles are drawn with solid lines and dashed lines, respectively. [18]

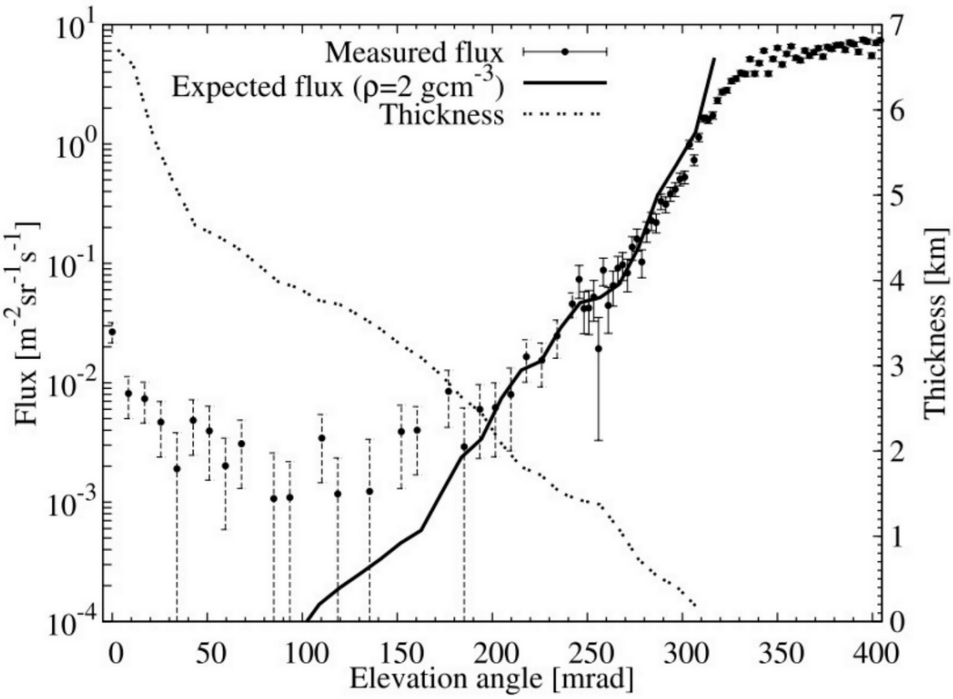

Figure 5: The comparison of measured and expected fuxes. The measured flux with 1σ error bars is plotted as the function of elevation angle within ± 10.9 mrad horizontal angle range. A dotted and solid line respectively indicates the rock thickness and the flux calculated by assuming an average rock density of 2 gcm^{-3}. [19]

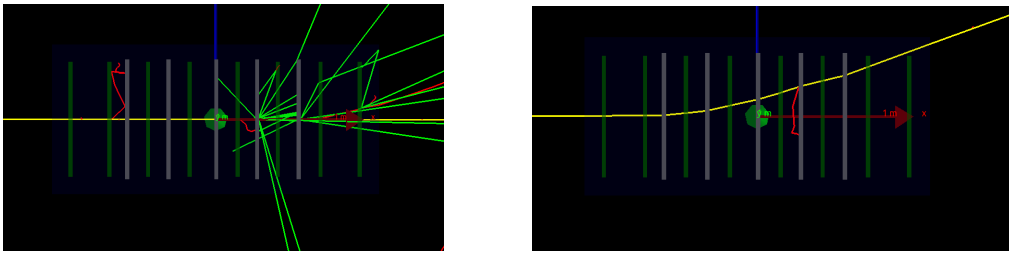

Figure 6: Two muons simulated in the MOS8-detector. On the left a muon with 50 GeV initial energy crosses the detector without scattering and produces several γ-rays and electrons. On the right a 500 MeV muon crosses the detector while scattering substantially. Yellow tracks are muons, red ones are electrons, blue ones positrons and green ones are γ-rays.

2.4 Simulation of the detector system

The detector system developed by our research group was simulated in Geant4 (version 10.5). The Physicslists chosen were the prebuilt "General", and two custom built ones for muons. The latter ones included ionisation, Bremsstrahlung, pair production, multiple scattering and capture for muons as interactions. For the rest of the particles the electromagnetic processes defined were: photoelectric effect, Compton scattering, pair production (for γ), pair production, ionisation and multiple scattering for electrons and positrons. Decays and other interactions for hadrons and ions were included in the "General" PhysicsList. The "cut" value that defines what secondary particles are created in the simulation was set to 0.1 mm.

The detectors included the printed circuit boards that form the base of each detector including the copper on top. The gaseous volume of the detectors consisting of Argon and Carbon dioxide was segmented into cubic volumes of $20\times12\times12$ mm^3. The energy deposition in these volumes was registered in the simulation. The effect of the read-out electronics was included from measurements (for details see subsection 2.7). Five lead absorbers with thickness of 2 cm and lateral dimensions of 80 cm and 80 cm were placed after the second, third, fourth, fifth and sixth detector. They had a steel cover with a 4 mm thickness as can be seen in figure 6. Muons were generated with a logarithmic energy distribution starting from 100 MeV up to 1 TeV. The origin of the muons were randomly chosen on a sphere and then shifted in the perpendicular plane with the size of the detectors. The individual wires were triggered above a 1 keV energy deposition limit.

2.5 Tracking algorithm

Gergő Hamar developed the tracking algorithm for the MOS detectors which I have utilized in my work. This code decouples the horizontal and the vertical directions (namely X and Y). The tracking starts with the clusterization of the hits. A straight line is fit to all permutations of the centers of the clusters. χ^2 is calculated for each fit and the smallest one is chosen. When the cluster is large, one can assume the presence of a δ-electron or an other particle. In this case the cluster is split up into two ones.

In order to maximize the tracking efficiency one can set the algorithm to try to fit the straight line to sets of clusters that contain one or two clusters less than the number of chambers. To give an example: for MOS-08 there are 8 chambers and each wire has a triggering efficiency of $\approx 95\%$. Therefore if we searched for muons which created a hit in all detectors the tracking efficiency would be 66%. However if we look for 7 clusters in the 8 detectors the tracking efficiency will improve to $\approx 94\%$.

The tracking efficiency and the effective area is calculated on the fly from measurements. Events containing excellent tracks are chosen. Each wire that is in the fitted line is checked whether it was considered a hit or not. The effective area is calculated from integrating over the detection efficiency of the wires in the full solid angle.

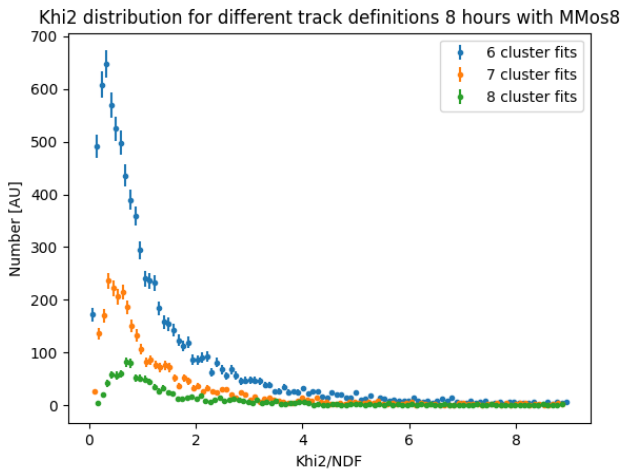

Figure 7: χ^2 distributions of 8 hours of measurements performed at the Sakurajima volcano. Events from all directions are shown. Three different settings are shown, in one the straight line was fitted to only 6 clusters from the eight detectors. In the remaining scenarios sets of 7 and 8 clusters were used for the fitting respectively.

In fig. 7 the χ^2 distributions of 4 hours of measurements performed at the Sakurajima volcano with different settings are plotted. One can see that there are the most tracks when we require to have a cluster in only 6 chambers out of the 8. There are two reasons for this: we have a higher acceptance since our potential field is larger in this case. The other reason is that we keep more lower energy muons and other background events with this permissive setting.

In the following part of this work we have chosen to use the tracking algorithm with the "N-1" setting, where the tracking uses 7 clusters from the 8 detectors. With this we obtain a tracking efficiency of $\approx$ 94 %, while still suppressing the low energy muons.

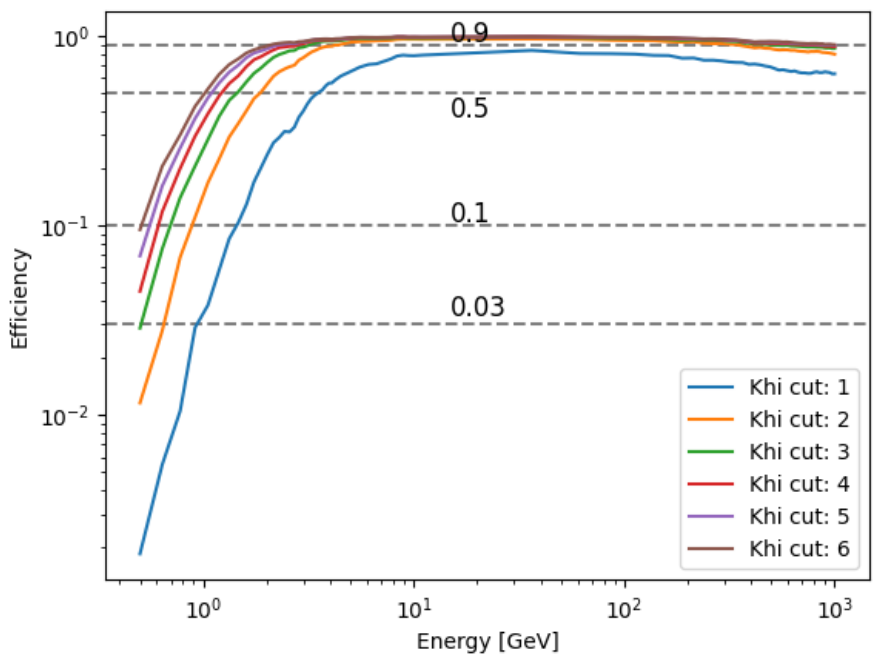

Figure 8: Efficiency (acceptance rate) of muons with different initial energies from Geant4 simulation for different χ^2 cuts. This plot focuses on the background suppression. Eg. a cut at 2 in χ^2 suppresses 80% of 1 GeV events.

A dedicated simulation of muons and the detailed MOS-8 system was carried out. 100 000 muons were simulated isotropically from different directions. Only those muons were simulated that would hit the middle half of the first and last detectors if they went straight (using geantinoes).

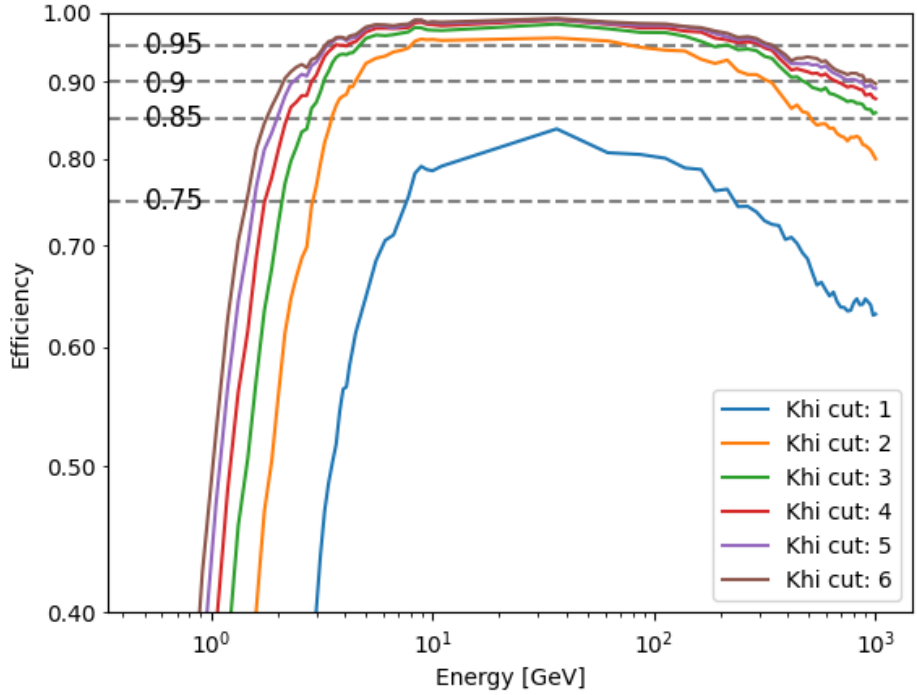

Figure 9: A zoomed in plot of figure 8. Efficiency (acceptance rate) of muons with different initial energies from Geant4 simulation for different χ^2 cuts. This plot focuses on the medium and high energy regime. A cut at 2 in χ^2 keeps 95% of 10-100 GeV events, which are the most important signal but drops to 80% at 1 TeV.

Events with known initial muon energy from the Geant4 simulation were processed with the tracking algorithm in order to understand what fraction of muons are detected depending on muon energy. In general muons below 1 GeV are considered background in volcano muography and should be discarded as shown in figure 4.

For the muon identification, introducing a cut in the χ^2 value is necessary to suppress the low energy muons that tend to have a high χ^2. In figure 9 the efficiency of the tracking can be seen for different cuts and different initial muon energies. A cut at 4 was utilized in the following work as we wanted to maximize the tracking efficiency.

2.6 Validation of the simulation

The simulation was validated in two ways. The χ^2 distribution was calculated for muons with energy ranges between 2-5 GeVs and 5 GeV-1 TeV. The results were compared with measurements taken with the detector at the Sakurajima volcano. Muons coming from the open sky with low elevation angle (0-150 mrad) have a harder spectrum since the mass of the air in this direction is very high. On the other hand, muons with an elevation of 300-400 have a softer spectrum (see fig. 1).

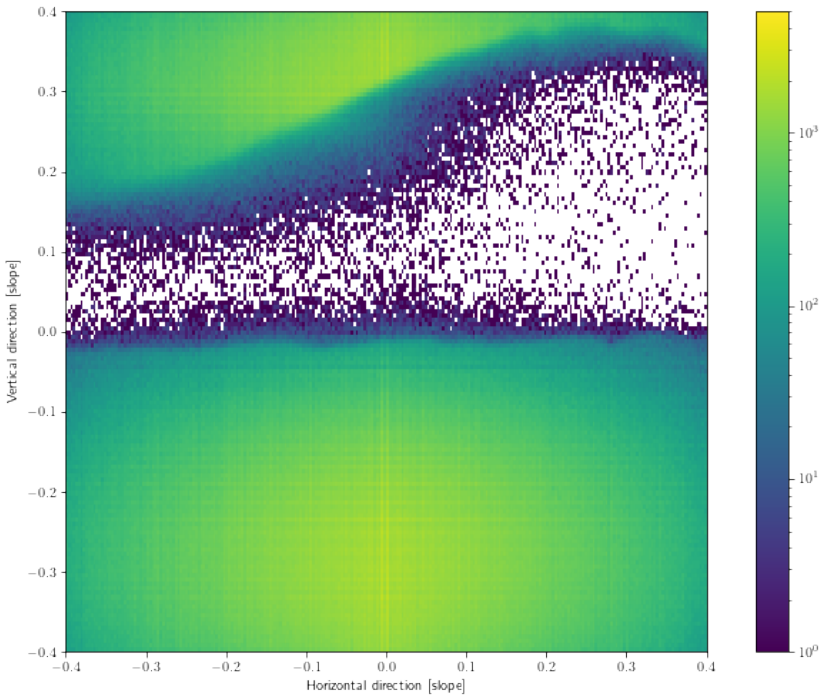

Figure 10: Number of muons detected between 25 August 2019 to 22 January 2023 with MOS-08 system at the Sakurajima volcano. The shadow of the volcano is visible.

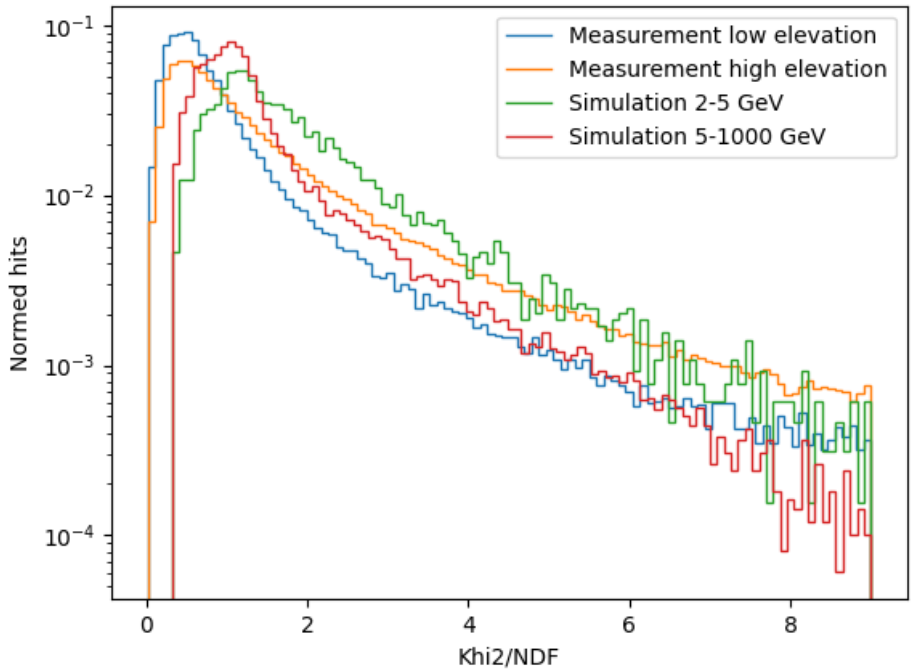

Figure 11: Comparison of χ^2 distributions of measurement with simulation. The simulation describes the long tail of the distribution that is known to be a notoriously hard problem.

2.7 Including detector effects into the simulation

Three effects of the detector could not be simulated and were determined from the measurements performed at the Sakurajima volcano: detector efficiency, changes in the gain and cluster size. After being quantified these were included in the results of the simulation before being used to feed the machine learning algorithm. Without taking these effects into account the neural network performed significantly worse.

The measured energy deposition depends on a wide variety of factors (temperature, humidity, pressure, set voltage, potential short circuits in the detector). Figure 12 shows how much the gain can change. Since the neural network assumes that the gain is fixed for all detectors we simply fit a Landau distribution (with the PyLandau package[23]) to each chamber's energy deposition distribution and normalize it to have the gain of the simulation. In figure 13. such an example can be seen. Each chamber has slightly different gain. After fitting the Landau distribution to the measurements (left), the gain becomes the same (right plot). The fit converged for 99.9 % of the measurements.

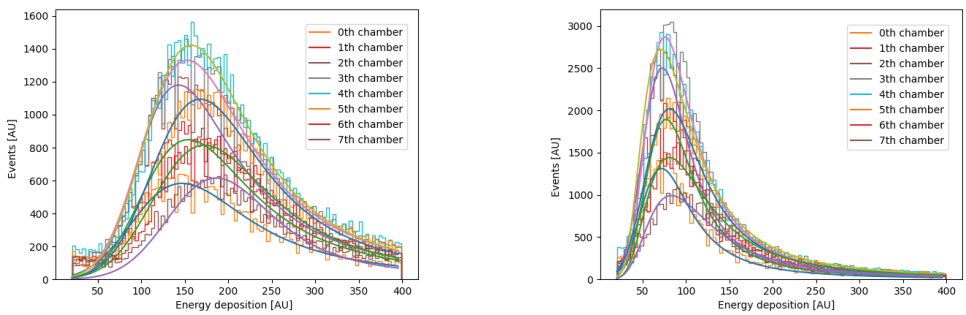

Figure 12: An illustration on how much the energy deposition changes for different measurements. The gain of the system changed more than a factor of two between the measurements of the left and the right plots. Landau distributions were fitted to the distribution of each channel.

In the detectors in one direction three wires are connected. Therefore the energy deposition close to one will create a signal in all of them. Therefore the cluster size is mostly three in that direction. In the other direction two pads are connected. For the latter direction we expect two pads to fire. In the simulation the energy deposition is registered in individual voxels. Therefore the number of wires and pads in the results of the simulation were increased using the distribution derived from the measurements, see figure 16.

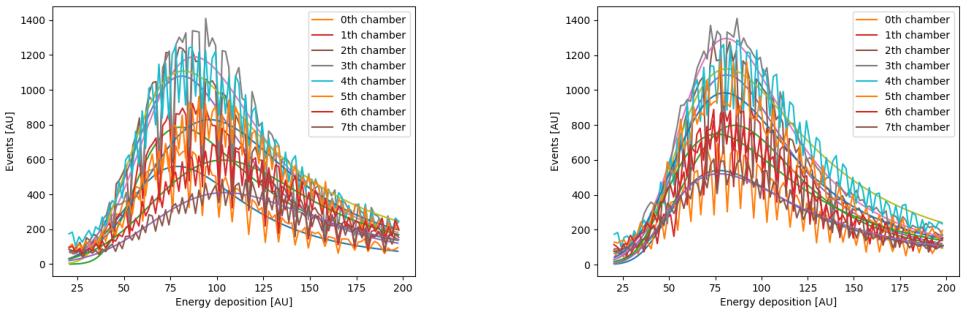

Figure 13: On the left the energy deposition distribution in each of the eight chambers of the MOS-8 acquired 14 June 2021 from 6 pm until 2 am the next day. Landaus distributions were fitted to each distribution and the fits are plotted. On the right the same distributions are plotted after being scaled to have the same position for the peak that we had in the simulations.

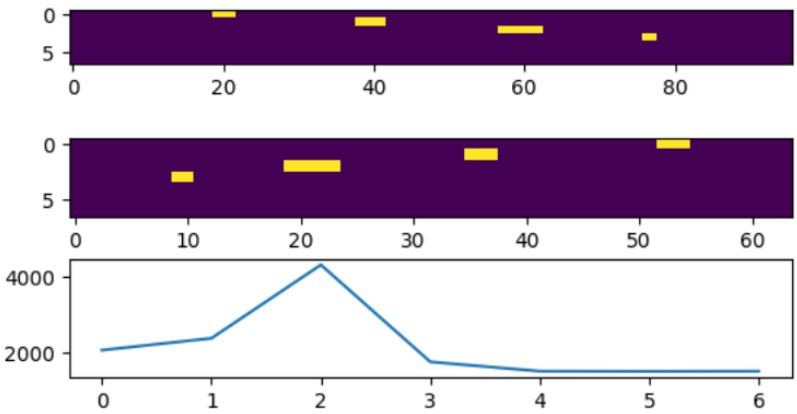

Figure 14: An example event recorded at the Sakurajima volcano with MOS-08. The top subplot shows the wires hit in the horizontal direction for each MWPC. The second one is the hit wires in the vertical direction. The third subplot is the energy deposition in each chamber. TODO: add axes labels

In the direction where wires are connected the chance that one wire fires is 38 % two wires fire is 53 %, three of them is 9 %. In the other direction these values are the following: 50%, 43 % and 7 %. The individual detector efficiency is almost 100 % in the simulation. While in reality it is around 97% [14]. There are two major reasons for this: dead channels, some structural holders in the detectors. This was taken into account in the simulation by

randomly throwing away hits with a 3 % probability.

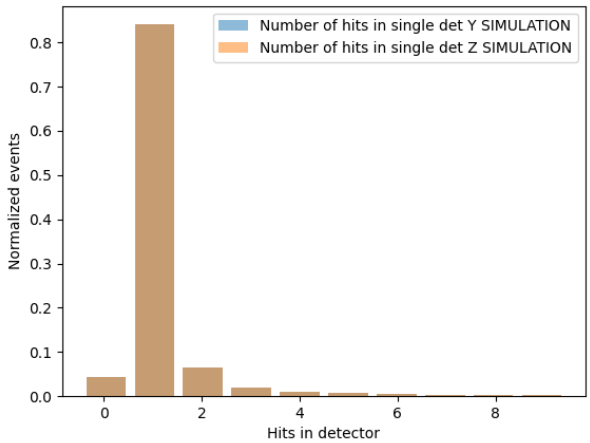

Figure 15: Number of hits in the detectors in the Geant4 simulation. For each detector the number of wires that fired were counted. Since the simulation does not take into account the effects of the readout, these were included from the measurements.

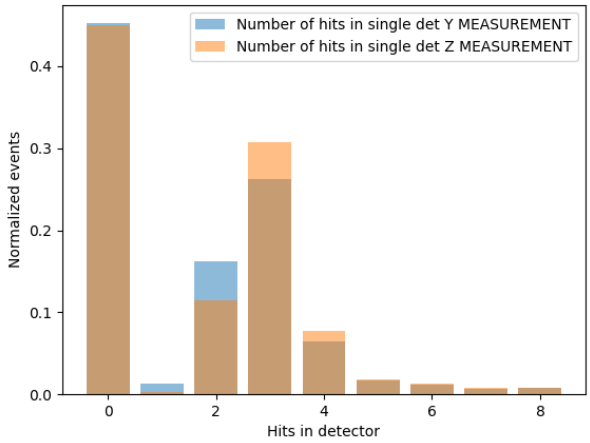

Figure 16: Number of hits in the detectors during a four hour long data taking run of the MOS-08 at Sajurajima volcano. For each detector the number of wires that fired were counted. The distribution is different in the two directions as the read-out is different.

2.8 Neural network

The traditionally used tracking algorithms in muography use the χ^2 method. A straight line is fitted to the hit coordinates in each detector and the square of the deviation from the fitted line is summed up. The problem with this method is that it does not take into account the correlation between the scattering in different absorber layers. It also does not use the energy deposition in the detectors which provide information on the number and type of the created secondaries.

We have chosen the deep neural networks (DNNs) to predict whether the observed particle had high energy (signal) or it was a background particle (muon or proton). TensorFlow version 2.11.0. was used. Fig. 17 shows the architecture diagram of our neural network. The input data is fed into three separate neural networks. Their results are concatenated and a fourth subnetwork draws the final decision. We have utilized a similar network before but for a different purpose. For an other detector system a network predicted the energy of the muons [24].

By using a subnetwork for each type of input data the performance of the network increased significantly. The reasoning behind this is that the direction of the track in the Y dimension is independent from the Z. This way we help the network to connect neurons to each other that forward relevant information.

input_3 consisted of the eight energy depositions, one in each detector of the MOS system. input_1 and input_2 were a list of Y and Z wire firings. The latter were a list of 512 and 512 binary values respectively. Residual layers were introduced into each subnet which helped with the classification significantly.

The data before being fed into the network was processed as described in subsection 2.7. An additional operation was performed. For each event the hits were "rolled" into the middle of the detector. In the Y and Z direction the minimum and maximum hit positions were recorded and all hits were moved so the tracks were centered. The reasoning behind this transformation is that parallel muons with the same energy hitting the detector are expected to behave similarly. Therefore the neural network did not try to distinguish them since they were moved into the center of the detector by the center of the track.

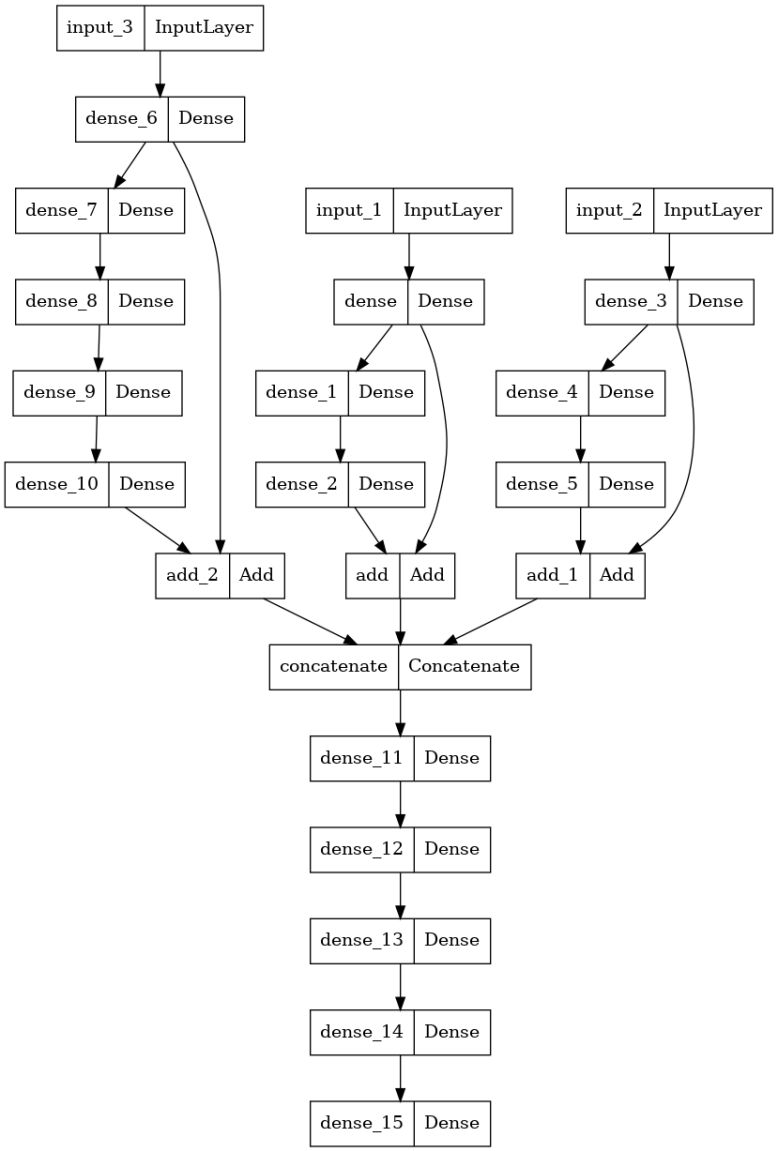

Figure 17: Architecture diagram of the neural network used to distinguish the low energy background from the high enery muons. input_3 is the energy deposition inside the detectors while input_1 and input_2 are the hit positions in the Y and Z directions respectively.

2.8.1 Teaching the neural network

The output data of the Geant4 simulation was preprocessed to include the detector effects described in section 2.7. The resulting data was written out in Tensorflow Record data format (TFRecord), which is the own binary storage format of Tensorflow. It can be used to read in data several times faster compared to plain text files. Multithread reading of these files were used.

1000 epochs of teaching was performed in 10 hours. The goal of the neural network was to discriminate between the low energy muons from the high energy muons. There were two different networks taught. The only difference between them was the cut in the energy that separated the low and high energy samples. For the first network a cut at 2 GeV was chosen, while for the other one a cut at 5 GeV. The loss function that the network minimized was the sum of the binary crossentropy of all data samples that can be written in the following way:

$$H = -\frac{1}{N}\sum_{i=1}^{N} y_i \cdot log(y_{pred}) + (1 - y_i) \cdot log(1 - y_{pred}), \tag{8}$$

where y_i is 0 or 1 depending on whether the ith data point belongs to the first or the second class. y_{pred} is the score value that the network assigns to that specific event. (It is not the probability of the event to belong to one of the classes.) It is a value between 0 and 1 for each event. For a "perfectly" taught network it would become the same as y_i.

Different metrics were evaluated to quantify the performance of the neural network. Table 1. shows the evaluated metrics, firstly the Area Under the Curve (AUC) of the Receaver Operating Curve (ROC). It is one of the most widely used universal metrics in the case of binary classification. A value of 0.5 is the same performance as a random choice. A score 0.5–0.7 is considered poor. Scores between 0.7–0.9 are considered fine, while a score above 0.9 is considered exceptional [25].

Besides the ROC-AUC metric we have calculated several other metrics including accuracy, true positive rate (TPR), true negative rate (TNR). The latter metrics are calculated from the elements of the confusion matrix. The values of this matrix are also included in table 1.

	Acc.	AUC_R	AUC_P	TPR	TNR	TP	TN	FP	FN
5 GeV cut	0.900	0.952	0.973	0.954	0.786	66396	25784	7001	3219

Table 1: All metrics were evaluated on a validation dataset that was independent from the test and teaching datasets. AUC_R is ROC-AUC, AUC_P is PR-AUC. Acc. stands for accuracy. The true positive rate (TPR), true negative rate (TNR) are also included with the elements of the confusion matrix.

2.8.2 Testing the background suppression with the neural network

In fig. 18 the efficiency of the neural network for simulated muons can be seen. It suppresses 1 GeV muons 4 times more than the classical χ^2 method, which is shown in fig. 8. Furthermore the efficiency for high energy muons does not decrease like for the classical algorithm. Eg. for muons with 1 TeV energy the efficiency is 99.8 % versus 87 % (χ^2 cut of 4).

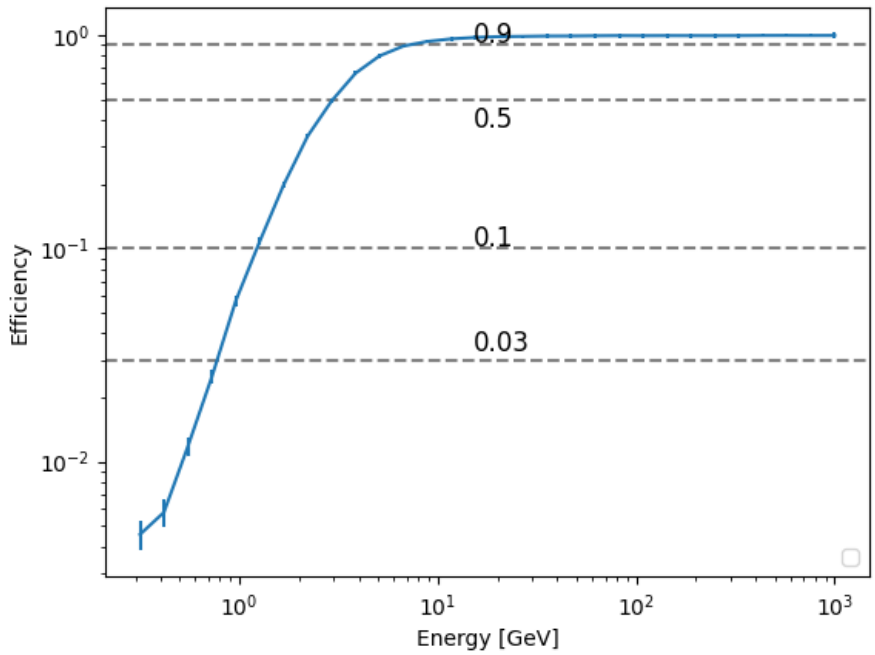

Figure 18: Efficiency (acceptance rate) of the simulated muons using the neural network with different initial energies. This plot focuses on the background suppression.

2.8.3 Applying the neural network to measurements taken at the Sakurajima volcano

Three and half years of measurements were analyzed with the tracking algorithm to determine the direction of the muons and then the neural network was used to predict which muons have low and which muons have high energy. The data analyzed in this work was taken by the MOS-08 system at the Sakurajima volcano from 25 August 2019 to 22 January 2023. There were 895 896 272 events all together. The network applied to the data was taught to discriminate at 5 GeV (described in 2.8.1).

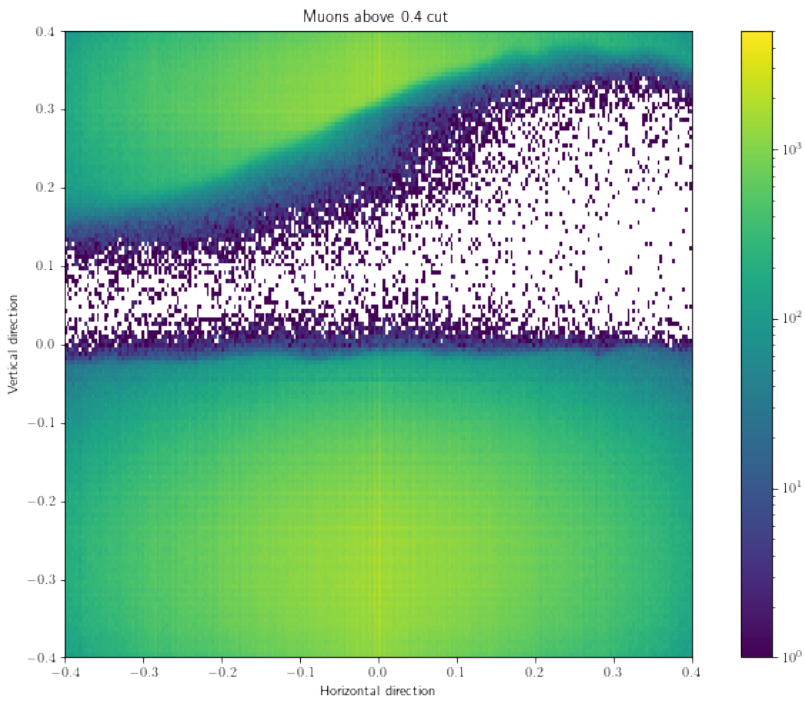

Figure 19: Number of detected muons between 25 August 2019 to 22 January 2023 with MOS-08 at the Sakurajima volcano. The tracks were filtered with the neural network to contain only the high energy ones. The used neural network was the one that discriminated at 5 GeV.

Two areas of interest were chosen to quantify the performance of the networks. The first area was where the volcano was so thick that no muons could penetrate it, therefore in that direction we expect the majority of muons to have low energy. This was the X $\in$ [0.1,0.4] and Y $\in$ [0.1,0.2]. The other area was the low elevation angle open sky: X $\in$ [-0.4,0.4] and Y $\in$ [-0.1,-0.3]. In figure 20. the predicted score of the network that was taught to discriminate at 5 GeV can be seen. As expected the network accepts the majority of muons from the area where high energy muons are arriving and throws away the ones from the direction where we expect low energy ones.

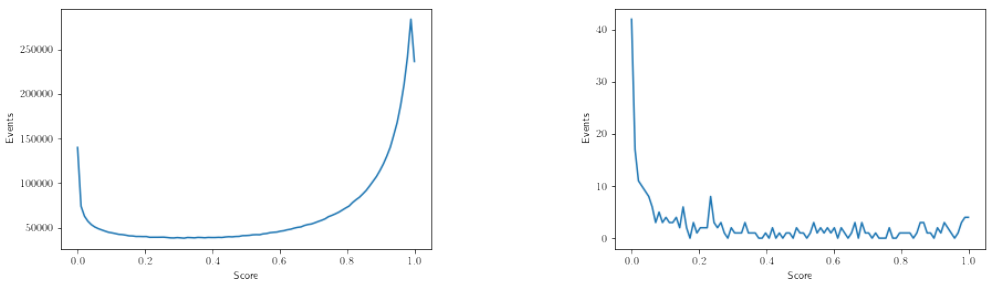

Figure 20: The predicted score of muons close to the horizon (left) and the where the volcano is at least 3km thick (right). The used neural network was the one that discriminated at 5 GeV.

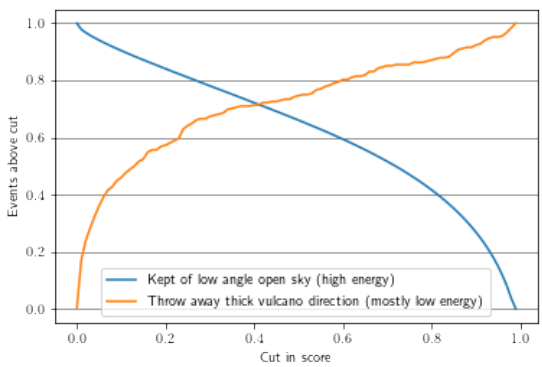

Figure 21: Fraction of accepted muons for two regions depending on what value we choose for the cut in score for the classification. The neural network was taught to cut at 5 GeV. Open sky muons with low elevation where the majority of muons have 5 GeV $\leq$ energy, while the direction of the thick volcano has below 2 GeV muons as described in fig. 4.

The muons that have higher than 0.4 score were accepted and the ones below 0.4 were thrown away. In figure 22. the proportion of the accepted vs. all muons are shown. In figure 23. the thrown away muons are shown.

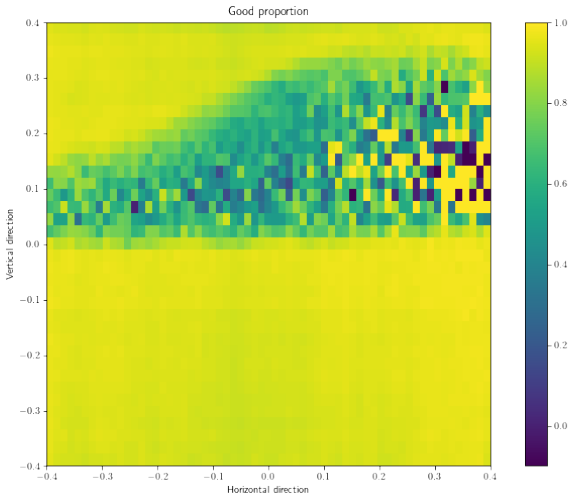

Figure 22: Fraction of muons that the neural network predicted to have a higher energy than 5 GeV versus all tracks. The network used here was taught to discriminate at 5 GeV.

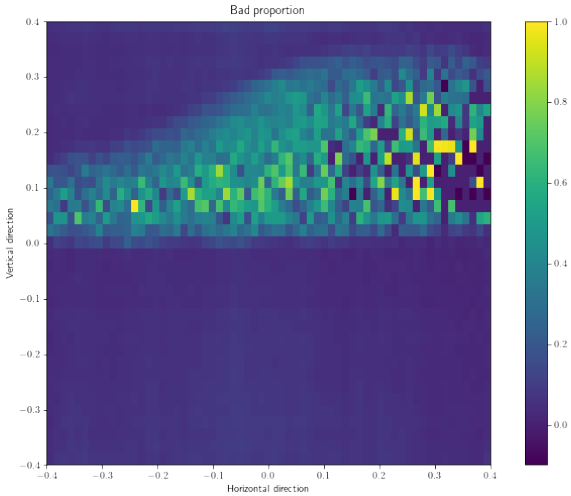

Figure 23: Fraction of muons that the neural network predicted to have a lower energy than 5 GeV versus all tracks. The network used here was taught to discriminate at 5 GeV.

In order to calculate the fluxes from the number of muons in each voxel from figure 19. we have done the normalization by taking into account the effective area (described in subsection 2.2). The measured fluxes along the vertical axis before applying the neural network and afterwards can be seen on figure 24 plot together with the thickness of the rock. In the horizontal direction the hits between X $\in$ [0.2,0.3] were taken into account where the thickness of the rock is very similar along the vertical axis. Above 2.5 km rock thickness only the background remains. The neural network tought to distinguish at 5 GeV between muons throws away 80 % of muons Y $\in$ [0.07,0.2]. While it retains 81 % of muons at Y $\in$ [0.07,0.2].

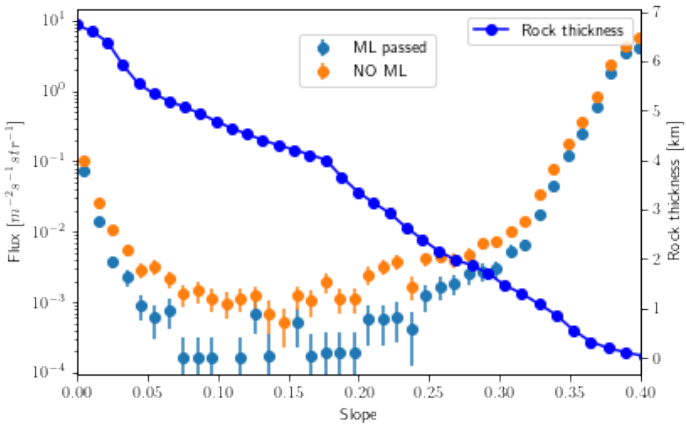

Figure 24: Flux measured with the MOS-08 detector in 3.5 years time with respect to the vertical direction. The rock thickness in the field of view is plotted as well. The developed machine learning (neural network model) suppresses the background.

2.8.4 Understanding how the neural network draws decisions

One of the techniques that helps to understand how a neural network draws decisions are the Shapley values. This approach originates from cooperative game theory and its concept earned the Nobel prize to its inventor Lloyd Shapley. It was designed to understand how individual members of a team contribute to the output of the team. Since there are correlations between impact of the individuals it is not straightforward to quantify their contribution. The rough idea behind the Shapley values is to remove several of the inputs to the model and evaluate the output for each set of inputs removed. In eq. 9 the Shapley value of the ith input.

$$\Phi_i(v) = \sum_{S \subseteq N \setminus \{i\}} \frac{|S|!(|N| - |S| - 1)!}{|N|!} (v(S \cup \{i\}) - v(S)) \tag{9}$$

S the "coalition" is the set of some of the inputs. $v(S)$ is considered as the total gain or collective output that the inputs in that coalition can obtain including their correlations. The number of elements in the coalition (S) is denoted by |S| and the number of permutations |S|!. The sum of the SHAP values of all inputs is equal to the difference between the output of the model for a specific event and the expectation value (which in our case is the average of all outputs). We have utilized SHAP values to understand which input parameters are the most relevant and to understand the underlying physics that the network learnt.

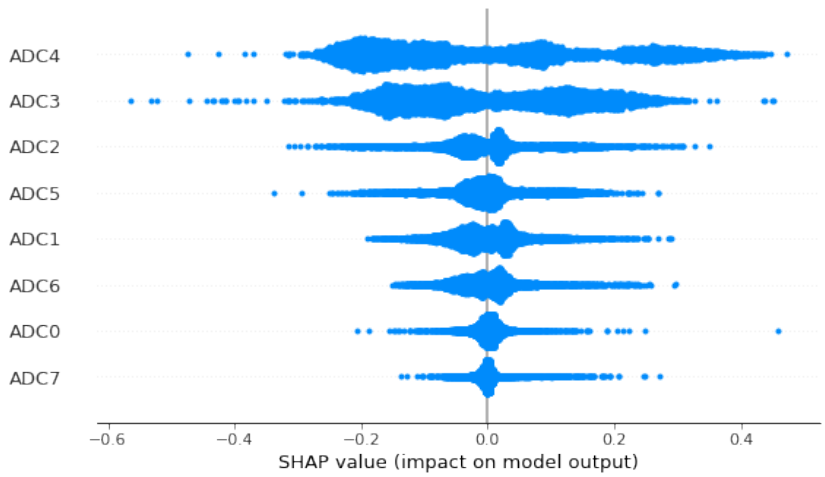

Figure 25: SHAP values for the energy deposits in the detectors. The chambers after the lead layers are the most important in the decision making.

Shapley values are both sufficient to be applied to individual events and

to draw conclusions on the whole set of data that the model is applied to. We had 8 ADC values as input, one for each chamber and 1024 wires as inputs. We have selected 1000 events randomly to plot the SHAP values. In fig. 27 the SHAP values for the deposited energies in the chambers are plotted. One can notice that these values range between -0.6 and 0.5 which means that the neural network uses them extensively. To give an example: the expectation value for our data sample was roughly ≈ 0.6 as we had a little more muons above 5 GeV than below. A single SHAP value of -0.6 means that if only that input existed the output of the model would be 0 which meant that the network predicts that that specific event was below 5 GeV with a very high probability. It is expected that the energy deposits after the lead absorbers are more important as the secondaries created in the absorbers are present there.

In fig. 28 the Shapley values of the wires can be seen. These values are an order of magnitude lower but it is expected as there are two orders of magnitude higher than ADC values.

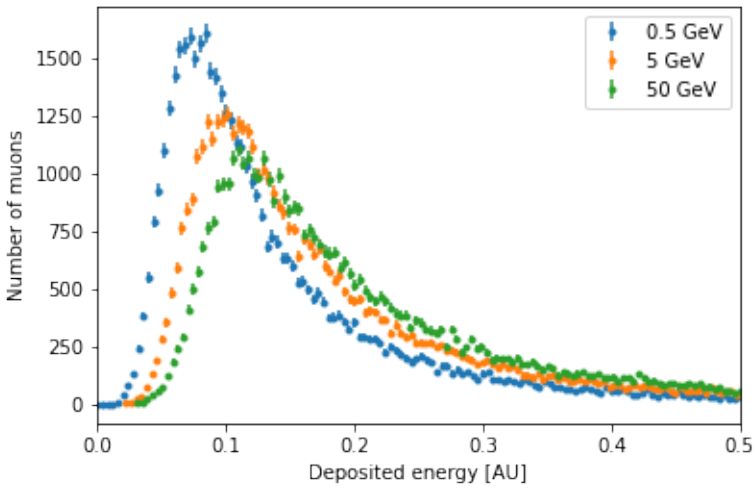

Figure 26: Energy deposition histogram in a single detector that is placed 14 cm from a lead absorber. 100 000 muons monoenergetic muons were simulated for each energy. The peak of the Landau curve shifts due to different stopping power in the gas. XXX beleirni

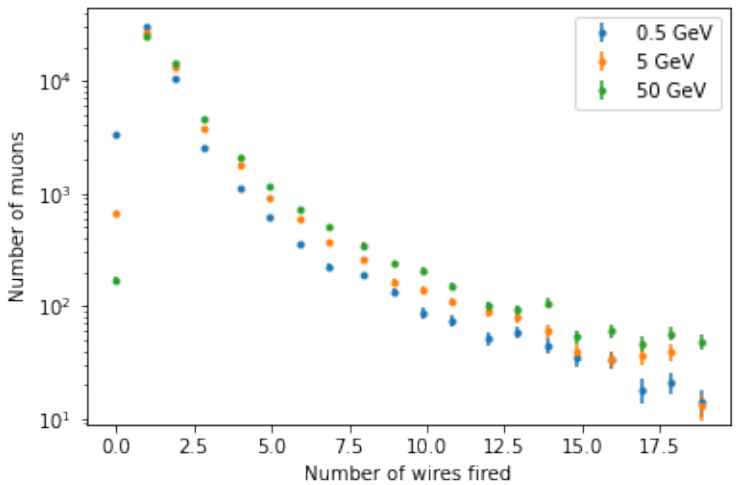

Figure 27: Number of wires fired in a single detector that is placed 14 cm from a lead absorber. 100 000 muons monoenergetic muons were simulated for each energy. For muons with higher energy more secondary particles are created. (The effect of the readout electronics was not included here.) XXX beleirni

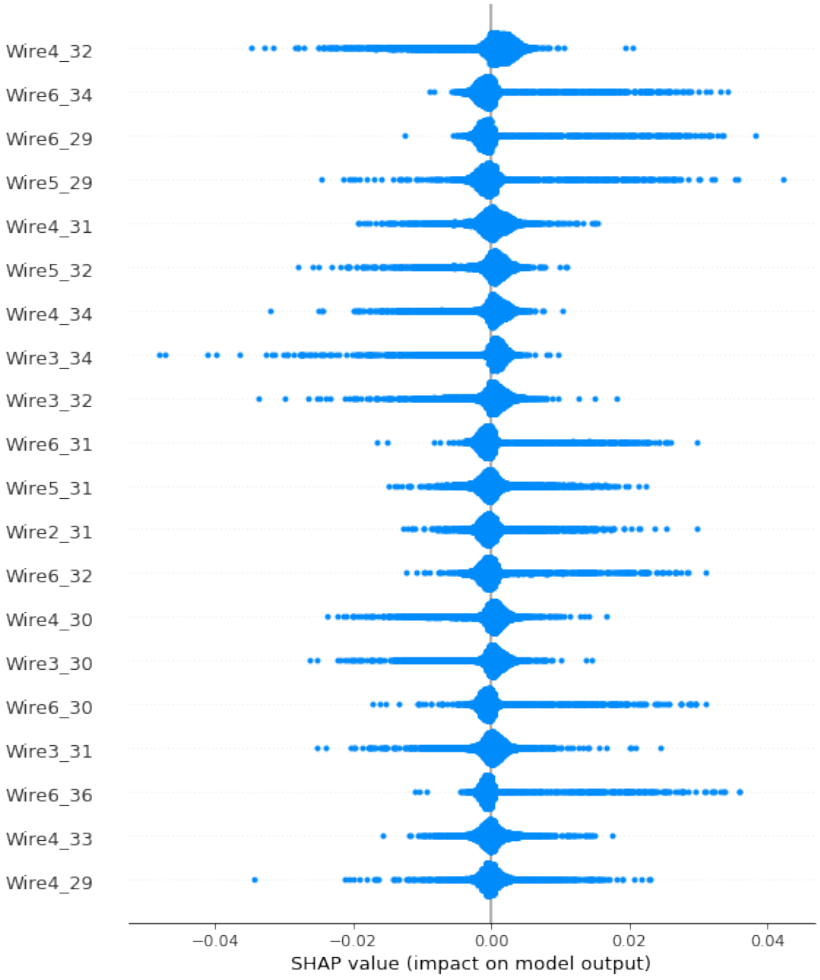

Figure 28: SHAP value for the 20 wires with highest SHAP values. The number of the detector is shown after the Wire name, while the number of the wire is the second number.

2.9 Achieving a better background suppression with neural networks

In this chapter we described a novel method of background suppression in muography of volcanoes. We have proven that the developed solution is capable of suppressing the low energy muons and protons more than the "classical" tracking algorithm that fits a straight line of all the permutations of the detected clusters and searches for the smallest χ^2 value among all permutations. We also understand what input parameters the neural network utilizes and why by calculating the SHAP values of the input data.

Besides developing a novel way to suppress the low energy background, the developed Geant4 simulation was also used to characterize the "classical" tracking algorithm. This is very important since our detector system does not have a spectrometer, therefore the algorithm can not be quantified with measurements.

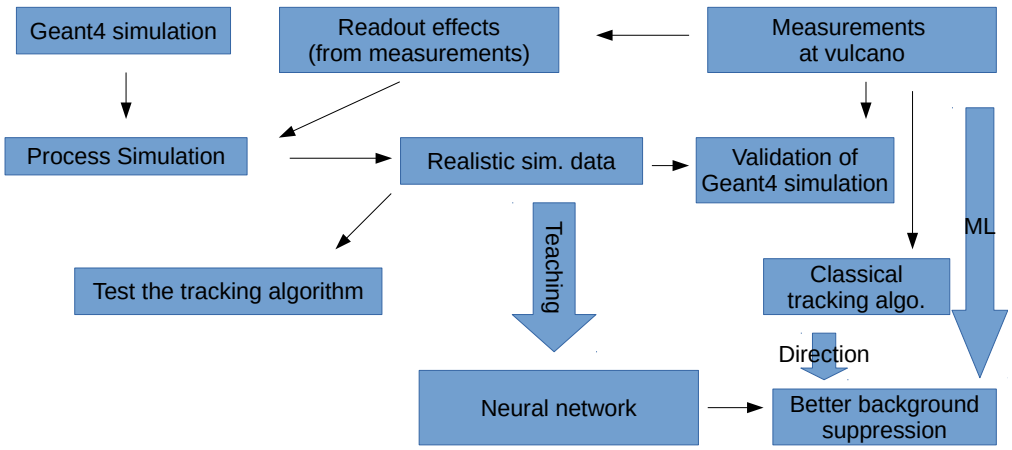

Figure 29: The outline of this work. The Geant4 simulation output is processed to include the readout effects from the measurements. Then it is validated by the measurements. Afterwards the tracking algorithm is characterized with the verified simulations. In the end a neural network is taught with the "realistic" simulation data and is used to achieve a better background suppression than with the classical algorithm.

3 Material analysis with muons and their secondary particles

3.1 Introduction

Muography is a well established method to obtain 3D images of large objects (e.g. volcanoes and large buildings) without any additional particle source, taking advantage of the presence of cosmic muons. The underlying principle of muography is the measurement of individual muon tracks and the determination of their absorption or scattering. These processes depend on the material that they have travelled through. The novel method discussed is based on the measurement of the muon tracks and of the corresponding particles that were produced by the muons themselves in the investigated target. As muons pass through matter they interact with matter by ionization, bremsstrahlung, pair production and nuclear interactions. Our experimental setup is designed in a way to measure both the primary muons and the created secondaries (mostly electrons and gammas). The tracks of the muons are determined by a special kind of Multi-Wire Proportional Chambers (MWPC) called CCC (Close Cathode Chamber). The secondary particles produced in the target are measured by four plastic scintillators placed around the target. The CCC chambers and the scintillators are used in coincidence in order to gather data about muons that passed through the target. As cross sections of the described processes vary by the density and the atomic number of materials this technique could be used to investigate the material content of the target.

For some particle physics experiments cosmic muons are a background which needs to be taken into account. However in the last 50 years the presence of cosmic muons has been used also as a tool to obtain 3D images of large objects, e.g. pyramids and volcanoes [26, 27, 28]. In our experiment we have the aim to prove that secondary particles created by cosmic muons upon crossing matter could be used to distinguish different materials [29, 30]. This could be useful for small scale objects that other non-invasive methods (e.g. X-ray) are not able to penetrate, for example meteorites. Our experimental setup consists of a set of trackers to identify cosmic muons and large area scintillators to detect the secondary gammas and electrons created by the interaction of the muons with matter.

3.2 Secondaries produced by cosmic muons

By measuring the number, the energy and the type of the secondary particles we can gain information about the material that the muon passed through. Muons interact with matter by ionization, pair production, bremsstrahlung and nuclear interaction.

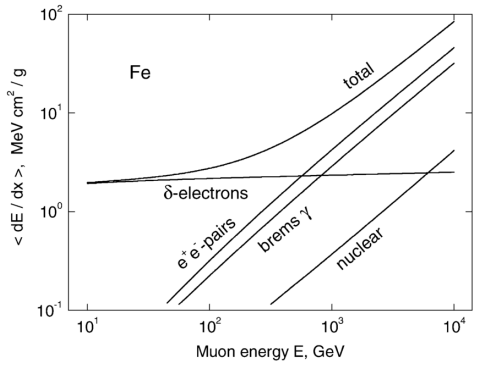

Figure 30: Energy loss of muons due to different interactions inside iron [31].

In fig. 30 the average energy loss of muons due to different processes is shown. In practice in our case muons at sea level, with an average energy of 3-4 GeV, have an energy almost always less than 100 GeV. Therefore nuclear interaction is not relevant. For the primary muon energy presented in this paper (1 GeV) muons lose energy mostly by ionization in all types of matter. For higher energies above 10 GeV in low-Z materials, delta-ray production leads to most detections. On the other hand, for higher energies in high-Z materials Bremsstrahlung yields the majority of the detections.

3.3 MUon CAmera (MUCA)

The MUon CAmera (MUCA) [32, 33] consists of a tracker system and a set of scintillators. The former is on the top of the target volume and the latter is around it. The tracker system consists of a set of Close Cathode Chambers (CCCs) [34] and its aim is to detect cosmic muons passing through the target volume. The scintillators placed around the target cover 75% of the solid angle in order to detect the secondary particles produced by muons inside the target volume. The scintillators and the tracker system are read out in coincidence.

Using coincidence between the detectors with 200 ns time resolution lowers the gamma background to almost zero. The required acquisition time depends on the density and atomic number of the target material. It varies from hours to days.

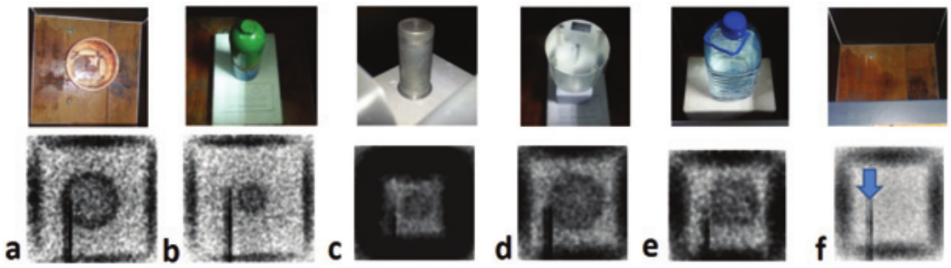

Figure 31: (a) Cu cylinder (b) Iron cap (c) Aluminum cap (d) Headphantom (e) Water in plastic bottle (f) Background image (empty imaging volume): the arrow indicates an artifact due to elec- tronic noise in the tracker's layer. The dark areas on the sides of the images are due to muons crossing the scintillators. Acquisition time 1-2 days [32].

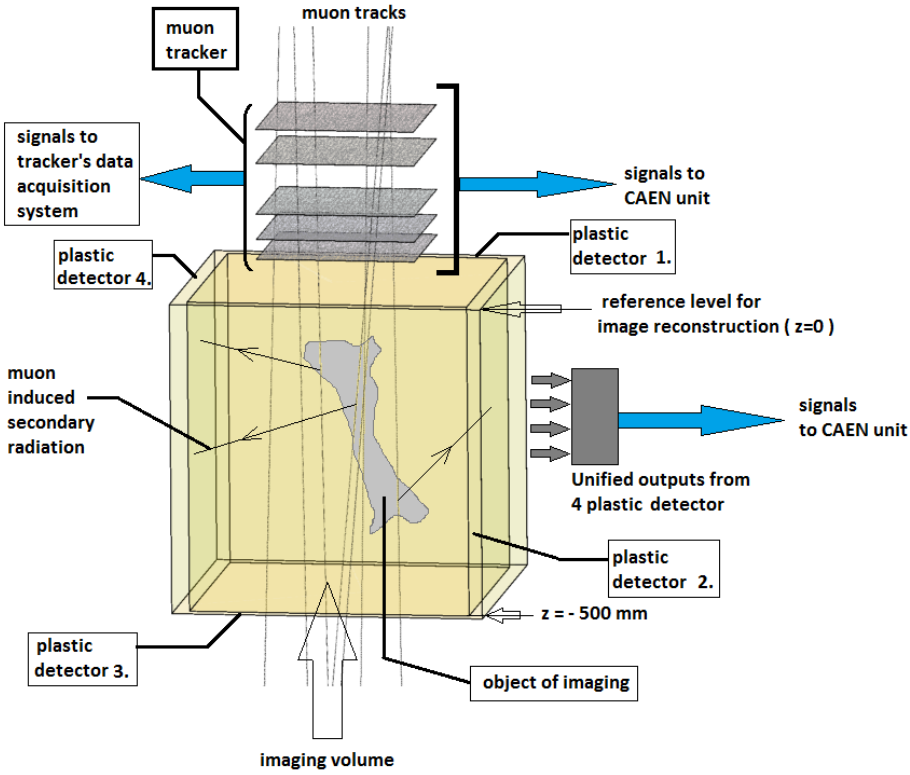

Figure 32: The schematic drawing of the MUCA system examining a bone [32]. Tracker layers above the target identify muons and the scintillators on the sides detect the secondaries produced inside the target [28].

A wide variety of materials were investigated by the MUCA system [32] including materials with high and low atomic number and also with very different densities. A few examples can be seen in fig. 31. The secondaries produced by cosmic ray muons were measured by four scintillators surrounding the target.

The main difference between our experimental setup and the currently existing projects observing muons with cosmic origin is the fact that we take advantage of detecting the secondary particles produced by the muon interacting with the target material.

3.4 Geant4 simulations

A wide variety of materials were investigated by the MUCA system [**?**] including materials with high and low atomic number and also with very different densities. A few examples can be seen in fig. 31 The energy spectrum of the secondary particles produced by the cosmic muons currently measured by the four scintillators surrounding the target. A series of Geant4 [36] simulations were developed to understand what particles are produced in different materials and also to take into account the energy deposition and the optical light propagation inside the scintillators.

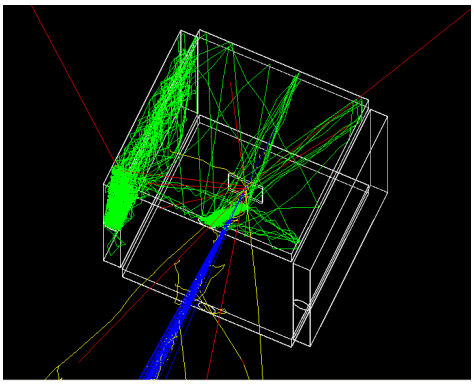

Figure 33: Geant4 simulation of a 10x10x0.5 cm3 lead brick in the middle hit by 50 muons with energy of 1 GeV. [37]

In fig. 33 the secondary particles produced inside the target lead brick and the optical photons produced inside the scintillators can be seen. Yellow tracks represent electrons, the red ones gammas. The green ones stand for optical photons and the blue ones are the primary muons. Only those optical photons are plotted, which were detected by the PMTs.

3.5 Validation of the simulations

The optical parameters which define the way the optical photons created in the scintillator needed to be calibrated in the simulation. The three main optical parameters in Geant4 are reflectivity, absorption length and light yield (created optical photons per depleted energy). In figure 34 the experimental setup that was used to do this at Wigner RCP can be seen. We have placed a CCC above the scintillator to track the cosmic muons which crossed the scintillator.

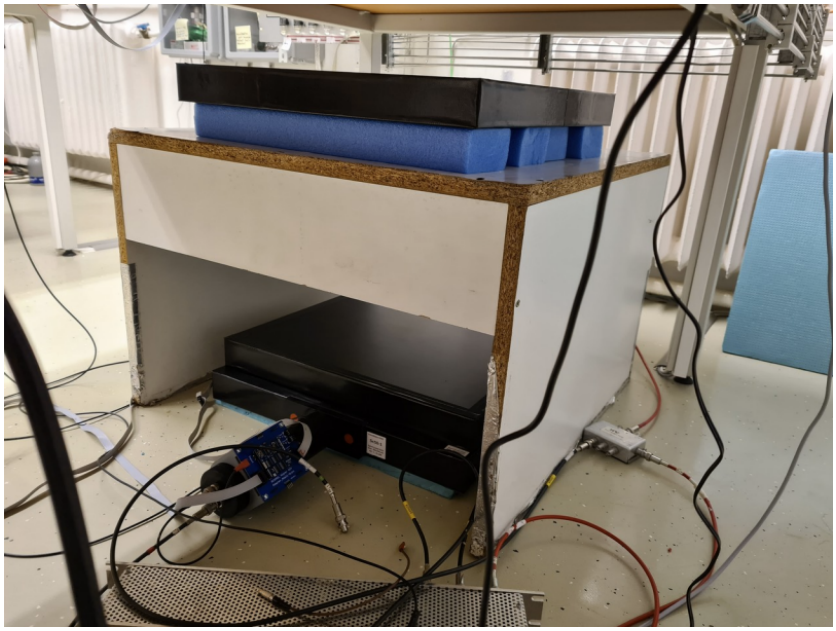

Figure 34: Measurements performed for the calibration of the optical parameters of the scintillators. On top there is a CCC based tracker which records muon tracks. Below in coincidence we record the energy deposition in the scintillator.

The energy deposition in the scintillator was recorded along the axis perpendicular to the PMT that read out the signal. By setting the absorption length to 240 cm and the reflectivity to 99.995 % we have reproduced the measured distribution. In figure 35 the simulation with this setting and the measurements can be seen. The muons that pass through the scintillator closer to the PMT yield a higher number of detected photons for two reasons: the photons have to travel a shorter distance to the PMT and the solid angle of the surface of the PMT is larger too. The light yield directly could not have been calibrated this way as the read out ADC depends on the gain of the PMT as well which was not known.

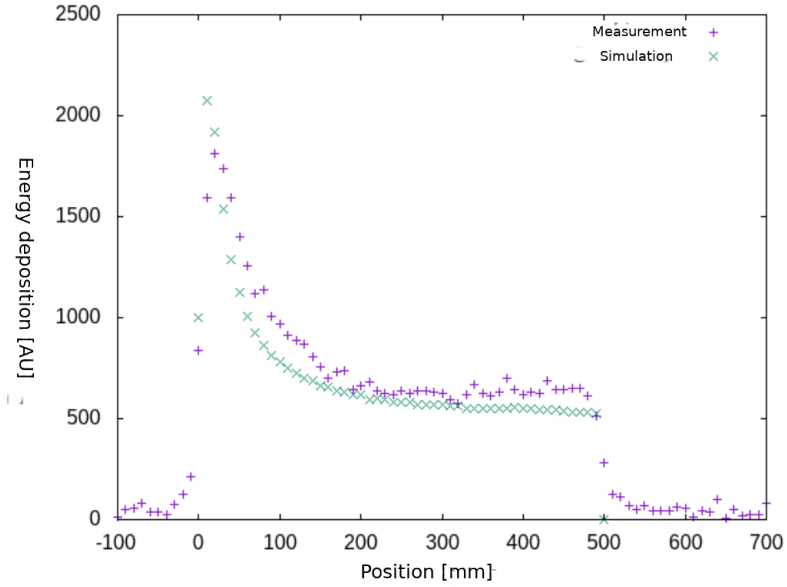

Figure 35: The energy deposition in the scintillator was recorded along the axis perpendicular to the PMT that read out the signal. The optical parameters of the simulation were set to reproduce the dependence of the signal on the position.

3.6 Results

3.6.1 Secondaries created and exiting the target volume

From an experimental point of view, the directional momentum distribution of the created secondary particles is extremely relevant as the flux of cosmic muons is low. Therefore to keep the required time of measurement with the MUCA system within realistic values one needs to capture as many secondaries as possible. In fig. 36 the polar angle of the created electrons and gammas is plotted. Secondaries favour the forward direction due to the relativistic energy of the cosmic muons. Another reason why secondaries exiting the volume favour the forward direction is that there is less material to be crossed in this direction.

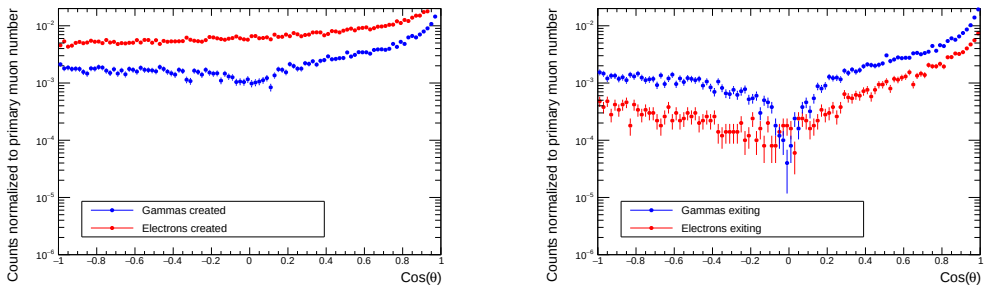

Figure 36: The polar angle distribution of all created secondary particles (left) and the polar angle distribution of secondaries exiting a lead target with a size of 10 x 10 x 0.5 cm^3 (right).[37]

The spectrum of the produced secondary particles can be seen in fig. 37 for a muon energy of 1 GeV and a lead target. Note that the drop at low energy in the electron and the gamma spectra on the left is due to the production cut in the simulation in order to keep computational time affordable. This specific cut was chosen to be lower than the required energy for electrons to exit the target and to arrive to the scintillators. This is the energy which is needed for the detection of electrons. Figure 37 right shows the spectra of particles leaving the same target. Secondary electrons lose much more energy therefore they are more suppressed.

3.6.2 Distinguishing materials by the produced secondaries

Our simulations show that a simple way to distinguish materials is to measure the ratio and number of gamma particles and electrons detected. In table 2 the probability of secondary particles exiting with the corresponding energy threshold is shown. The target was chosen to be 10x10x0.5 cm^3.

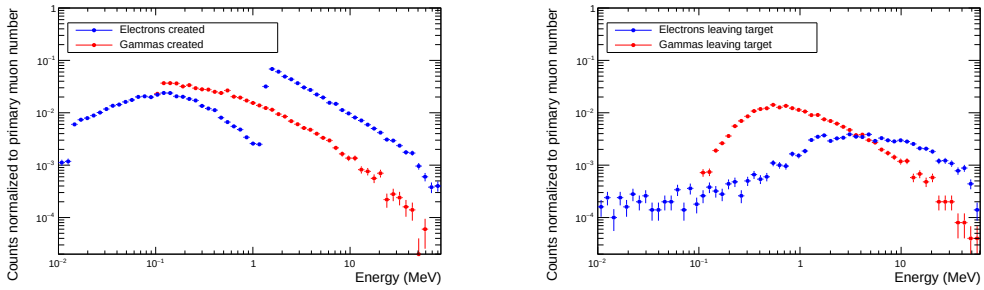

Figure 37: The energy distribution of all created secondary particles (left) and the energy distribution of secondaries exiting a lead target with a size of 10 x 10 x 0.5 cm^3(right).[37]

This energy threshold was chosen to be 0.1 MeV for gammas and 1 MeV for electrons as this is roughly the minimal energy that is required to arrive to the scintillators and be detected. The ratio of gammas and electrons varies by more than 2 orders of magnitude for different materials investigated.

	Lead	Copper	Water	Polystyrene
γ, E $\geq$ 0.1 MeV	20.7 %	10.6 %	0.14 %	0.14 %
e^-, E $\geq$ 1 MeV	6.68 %	13.1 %	6.08 %	4.7 %

Table 2: Fraction of secondaries leaving the target volume per incoming muon. Arbitrary threshold of 0.1 MeV for gammas and 1 MeV for electrons were used in the simulation. These energies were chosen as particles leaving the target roughly above these energy can be detected in the scintillators.[37]

In the case of lead every fifth muon produces a gamma with more energy than 100 keV and for polystyrene only one from one thousand muon produces a gamma with at least 100 keV. It is interesting to mention that the number of gammas produced in low Z material are similar but the number of electrons is different. For water there are 25% more electrons produced than for polystyrene.

3.6.3 Conclusions

A novel muography technique that takes advantage of the secondaries produced by cosmic muons and is sensitive to low Z targets was discussed. Geant4 simulations were performed to understand the particle production by muons, optimize the detector, and understand which kind of information the secondaries give on the target material.

4 Expected signal and background of gamma-ray sources by large field-of-view detectors aboard CubeSats

4.1 Introduction

Particle background is a considerable constraint for satellites, particularly those aiming to investigate the high-energy Universe. It is especially important for instruments without an anti-coincidence shield, e.g. for the increasingly large number of CubeSats which have recently been proposed for scientific missions.

A dedicated Geant4 [36] software has been developed including the simulation of the optical light propagation inside the scintillators used as detectors. This way the detector response can be taken into account. In order to include the effects of scattering, photon conversion and other interactions happening between background particles, X-ray photons and the materials of the satellite, a computer-aided design (CAD) model of the whole satellite was included in the simulations.

The spectra of high energy photons and particles which contribute to the overall detected background were used as an input to the Geant4 simulations. These components of the external background include cosmic X-rays/γ-rays, cosmic ray particles, geomagnetically trapped particles and albedo (secondary) particles produced in the Earth's atmosphere.

In order to validate the background simulations, a set of dedicated experiments were carried out at the Hiroshima University in order to obtain the scintillator optical parameters (e.g. reflectivity of the surfaces and absorption length) which determine the position dependence of signal collection efficiency.

The developed simulation, spectra of the X/γ-rays and particle background as well as example spectra of high-energy photon transients were applied on one 3U CubeSat belonging to the planned Cubesats Applied for MEasuring and LOcalising Transients (*CAMELOT*) constellation [40, 41, 42]. This simulation framework can be also helpful for other CubeSat and SmallSat missions with gamma-ray detectors in preparation by other teams, e.g. *BurstCube* [43, 44], *BlackCAT* [45], Gravitational wave high-energy Electromagnetic Counterpart All-sky Monitor (*GECAM*) [46], Gamma-Ray Integrated Detectors (GRID) [47], *Glowbug* [48], High Energy Rapid Modular Ensemble of Satellites - Scientific Pathfinder (*HERMES-SP*) [49], Satellite

Polarimeter for High eNergy X-rays (*SPHiNX*) [50], *SkyHopper*[1], Space Industry Responsive Intelligent Thermal satellite, (*SpIRIT*)[2].

This chapter is organized as follows: Sec. 4.2 describes the astrophysical sources whose detectability is investigated, Sec. 4.3 overviews various background components, Sec. 4.7 describes the *CAMELOT* satellites and the detector system, Sec. 4.8 details the validation of Geant4 simulations and the calibration of the detector's optical parameters, Sec. 4.9 describes the performed Geant4 simulations, Sec. 4.10 presents the results of Geant4 simulations and Sec. 4.12 summarizes the conclusions.

4.2 Expected X-ray/γ-ray Transient Sources

The main scientific goal of the *CAMELOT* satellites is to detect (s)GRBs [51, 52]. sGRBs emit gravitational waves as well. This is extremely important as gamma-rays can only be detected in space and the field of view of current satellites do not cover the whole sky. For multi-messenger astronomy it is important to cover the gamma-ray, the neutrino, the optical and the gravitational wave domain together.

Short GRBs (sGRBs) originate from a merger of two neutron stars and possibly also from a merger of a neutron star and a black hole [53, 54, 55, 56]. Their length are usually characterized by the typical duration T_{90} (the time during which the cumulative counts increase from 5 % to 95 %) of their prompt gamma-ray emission. It is mostly $\lesssim 2\,\mathrm{s}$ in the observer frame [57] and their gamma-ray energy flux peaks at $\sim 600\,\mathrm{keV}$. On the other hand long GRBs (lGRBs) originate in the gravitational collapse of fast-spinning massive stars and their typical duration is $\gtrsim 2\,\mathrm{s}$. The prompt spectra of lGRBs are on average softer then the sGRB spectra with their energy flux peaking at $\sim 200\,\mathrm{keV}$.

The *CAMELOT* satellites might be sensitive also to other astrophysical X-ray transients such as soft gamma repeaters with typical duration of individual peaks in their light curves $\sim 0.2\,\mathrm{s}$ and with X-ray energy flux peaking at around 20 keV (see Sec. 4.2.2). Note that a hard component above 100 keV has been observed as well [58, 59]. Also the gamma-ray phenomena produced in the Earth's atmosphere during thunderstorms [60] called terrestrial gamma-ray flashes might be observed. These events are typically shorter than 1 ms and have gamma-ray spectra reaching energies of several MeV [61]. The following subsections describe in detail the fluxes expected from these sources. Fig. 38 summarizes the spectra of the

[1] https://skyhopper.research.unimelb.edu.au
[2] https://spirit.research.unimelb.edu.au

X-ray/γ-ray transient sources which we study in this section.

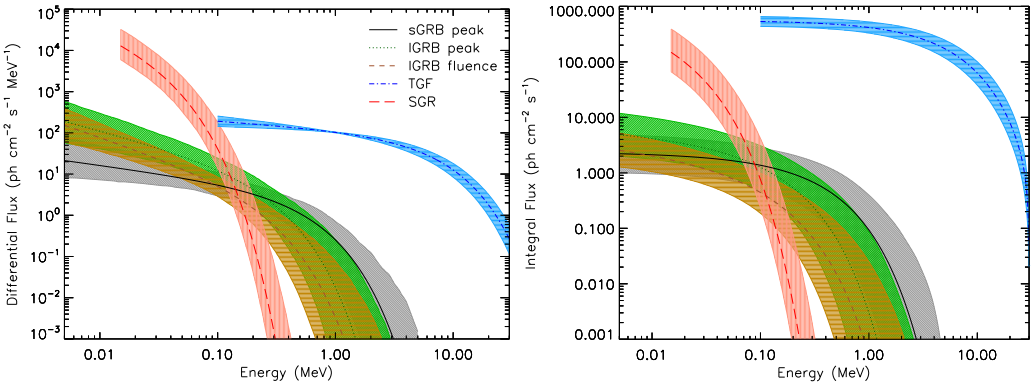

Figure 38: Differential (left) and integral (right) spectra of typical GRBs, SGR and TGF. The black solid curve shows a typical peak spectrum of a sGRB. The black dotted curve shows a typical peak spectrum of a lGRB and the black dashed line shows a typical fluence spectrum of a lGRB accumulated over the duration of the burst. The blue solid curve shows an average spectrum of a TGF based on measurements from the *AGILE* satellite. The red solid curve shows a typical spectrum of a burst from a SGR based on measurements from the Konus experiment. The shaded regions correspond to 68 % CL.[38]

4.2.1 Typical Short and Long Gamma-Ray Burst Spectra

Since the main objective of the *CAMELOT* mission is the detection of GRBs, we run Monte Carlo (MC) simulations using the typical spectra of sGRBs and lGRBs in order to estimate the expected signal-to-noise ratio. The typical spectra were constructed using the *Fermi* GBM Burst Catalog (FERMIGBRST[3]). For detailed information about the catalog see Ref. Gruber2014, vonKienlin2014, NarayanaBhat2016, vonKienlin2020. For sGRBs, we used the so called peak flux spectrum which is accumulated over the peak of the GRB (typically over 64 ms or 1024 ms). In the case of lGRBs, we used the peak flux spectrum and the so called fluence spectrum, which is accumulated over the whole duration of the burst.

Note that the 64, 256 and 1024 ms timescales of measured peak fluxes reported in the catalog do not match all the trigger timescales used by *Fermi*/GBM. The triggering system employs 120 possible sets of trigger algorithms (not all actively employed at a time and approximately 60 trigger

[3] https://heasarc.gsfc.nasa.gov/W3Browse/fermi/fermigbrst.html

algorithms are currently active[62]) consisting of eight set of energy bands, ten time scales 16, 32, 64, 128, 256, 512, 1024, 2048, 4096, 8192 ms and different time offsets for two phases of selected time interval. Most frequently, GBM triggers on 5 time scales from 16 to 4096 ms [63].

The typical spectra of sGRB and lGRB were constructed in the following way. First, we checked what was the most common best fit spectral model in the catalog. For peak flux spectra of sGRBs it was the power law model (PL). For the peak flux and fluence spectra of lGRBs it was the Comptonized model (CPL, exponential cutoff power law). For detailed information about the different spectral models see Ref. Gruber2014.

Although PL model was the most frequent one for peak spectra of sGRBs in the FERMIGBRST catalog, we use the second most frequent model, i.e. CPL. The reason is that sGRBs dim in peak flux are most frequently best fit by PL whereas brighter sGRBs are most frequently fit by CPL model. A likely explanation is that short GRB have Comptonized spectra, and that weak sGRBs produce insufficient signal in the instrument to distinguish the models.

Then in case of the peak spectra, we used the median best fit spectral parameters and then we tuned the normalizations A of the spectra to obtain the values of the integral fluxes in the range of $10 - 1000$ keV equal to the median 1024 ms, 256 ms and 64 ms timescale peak fluxes obtained from the catalog. The median peak fluxes for sGRBs for 1024 ms, 256 ms and 64 ms time scales and in the $10 - 1000$ keV range are 2.0, 4.8 and 7.5 ph cm^{-2}s^{-1}, respectively. Note that the median power law index for PL model for sGRBs peak spectra is $\alpha = -1.4$ which is unphysical [64] and that is also the reason why we use CPL model for sGRB spectra. In case of lGRBs the median peak fluxes for 1024 ms, 256 ms and 64 ms time scales and in the same energy range are 4.1, 5.2 and 6.7 ph cm^{-2}s^{-1}, respectively. For the fluence spectra of lGRBs, we used the median best fit spectral parameters, including the normalization, from the catalog. The obtained spectral parameters are in Table 3. The pivot energy $E_{\rm piv}$ is fixed at 100 keV. Figure 38 shows the typical GRB spectra with shaded regions corresponding to 68 % CL. These 68 % CL were obtained from the measured spectral parameters separately for short and long GRBs in the FERMIGBRST catalog and using the CPL spectral model.

4.2.2 Soft Gamma Repeaters

Soft gamma repeaters and anomalous X-ray pulsars (AXPs) are believed to be neutron stars with extremely strong magnetic fields of up to $B \sim 10^{14} - 10^{15}$ G called "magnetars" [65, 66, 67]. For reviews see

GRB type	Spec. type	A_{1024}	A_{256}	A_{64}	A	α	$E_{\rm peak}$ (keV)
sGRB	pflx	$0.0068^{+0.0090}_{-0.0035}$	$0.016^{+0.021}_{-0.008}$	$0.025^{+0.033}_{-0.013}$	—	$-0.38^{+0.34}_{-0.30}$	669^{+574}_{-350}
lGRB	pflx	$0.020^{+0.036}_{-0.012}$	$0.026^{+0.045}_{-0.015}$	$0.033^{+0.058}_{-0.019}$	—	$-0.75^{+0.37}_{-0.30}$	235^{+269}_{-117}
lGRB	flnc	—	—	—	$0.009^{+0.010}_{-0.004}$	$-0.96^{+0.37}_{-0.31}$	183^{+250}_{-89}

Table 3: Spectral parameters of typical GRB spectra. The spectral parameters are for the peak flux spectra (pflx) and the fluence spectra (flnc) of typical short and long GRBs. The normalizations A_{1024}, A_{256} and A_{64} are for the 1024 ms, 256 ms and 64 ms timescale peaks, respectively, A is the normalization for the fluence spectrum and all normalizations are in units of $\mathrm{ph\,cm^{-2}s^{-1}keV^{-1}}$. Parameters α and $E_{\rm peak}$ are respectively the power law index and the peak energy of the Comptonized model. The uncertainties correspond to 68 % CL.[38]

Refs. Lewin2006, Kaspi2007, Mereghetti2008, Enoto2019. First observations date to 1979 [68] with several magnetar bursts detected up to now, see e.g. Refs. Kouveliotou1998, Mereghetti2005a, Molkov2005, Yamaoka2017. For example a giant flare of magnetar SGR 1806-20 on 27 December, 2004 was observed by several satellites [69, 70, 71, 72, 73] and it was so bright that it saturated detectors.

SGR giant flares are rare and it is essential for their better understanding to observe and monitor all of them. The all sky coverage provided by future networks of nano-satellites will ensure that all future SGR outbursts will be detected and their behaviour will be monitored.

The SGR spectra are in soft gamma-ray region and well represented by a single blackbody (BB) or two-temperature BB model [59]. Above ~ 30 keV the spectra are well modeled by optically thin thermal bremsstrahlung (OTTB) [74].

In our simulations we analyze the response to regular SGR bursts. For an example spectrum of a regular SGR we utilize the Konus catalog of SGRs detected from 1978 to 2000 [75]. The catalog contains bursts from SGR 0526-66, 1627-41, 1801-23, 1806-20 and 1900+14 observed using detectors on board Venera 11–14, Wind, and Kosmos 2326 spacecrafts. The SGR photon spectra in the catalog are modeled by optically thin thermal bremsstrahlung using:

$$F(E) = AE^{-1}e^{-\frac{E}{kT}}, \tag{10}$$

where kT (keV) is the spectral parameter, E (keV) is the photon energy and

A (ph cm^{-2}s^{-1}) is the normalization factor.

We took 81 spectral fits from the catalog and derived the normalization factor A from each spectrum. Figure 39 shows the distribution of the kT parameter and the normalization A. The median values are $kT = 22^{+8}_{-3}$ keV and $A = 384^{+493}_{-300}$ ph cm^{-2}s^{-1}. The uncertainties correspond to 68 % CL. The typical duration of SGR bursts in the catalog is ~ 0.2 s. We use these parameters for an example SGR spectrum used in our MC simulations in the energy range of $15 - 500$ keV. The spectrum is shown in Figure 38 with the shaded region corresponding to 68 % CL which was calculated using MC simulations and the aforementioned values of kT and A parameters with their uncertainties.

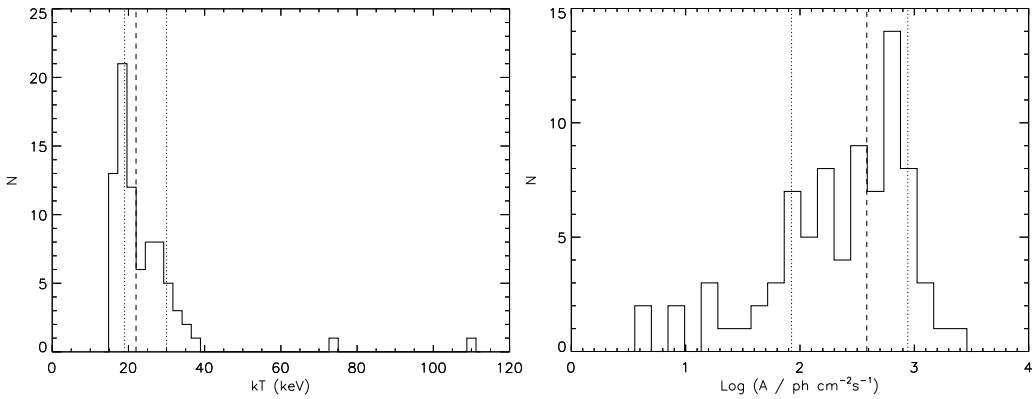

Figure 39: Distribution of the spectral parameter kT (left) and normalization A (right) from the Konus SGR catalog [75] for 81 spectral fits. The dashed lines mark the median values and the regions delimited by dotted lines correspond to 68 % CL.[38]

4.2.3 Terrestrial Gamma-Ray Flashes

Terrestrial gamma-ray flashes, brief bright bursts of multi-MeV gamma-rays, which are believed to be emitted by thunderclouds and generated, via bremsstrahlung, by the relativistic runaway electrons accelerated by electric fields in the atmosphere [61]. They were discovered by the Burst and Transient Source Experiment (BATSE) aboard Compton Gamma-ray Observatory (*CGRO*) [76]. Plentiful observations have also been provided by other astrophysical instruments such as the Reuven Ramaty High Energy Solar Spectroscopic Imager (*RHESSI*) [77, 78], the Gamma Ray Burst Monitor (GBM) on board the *Fermi* satellite [79, 80, 81], and the Astrorivelatore Gamma ad Immagini Leggero (*AGILE*) satellite [82, 83, 84].

The *AGILE* satellite was launched to 550 km altitude with inclination of 2.5°. The Mini-Calorimeter (MCAL) is composed of 30 CsI(Tl) scintillator bars with each crystal of dimension of $15 \times 23 \times 375\,\mathrm{mm}^3$ giving the detector a sensitivity from 300 keV to 200 MeV and the effective area of $200 - 1200\,\mathrm{cm}^2$ [85]. Although this makes *AGILE*/MCAL a more sensitive instrument for TGF detection than what is foreseen for *CAMELOT*, which is expected to be launched to polar LEO with detectors composed of 5 mm thick CsI(Tl) crystals, we use the *AGILE*/MCAL observations of TGFs as a reference for our simulations because the mission accumulated a large and high quality TGF database in orbit. For their TGF observations see the 3rd *AGILE* TGF catalog [60, 86] and the corresponding online catalog[4].

The duration of TGFs is typically below 1 ms with the peak of the distribution around $100-200\,\mu$s [82, 83, 84]. *AGILE* measurements show that the cumulative spectrum of 228 single-pulse TGFs in the range $0.4 - 30$ MeV can be fitted by a power law with exponential cutoff [83]:

$$F(E) = K \left(\frac{E}{1\,\mathrm{MeV}} \right)^{-\alpha} e^{-\frac{E}{E_\mathrm{C}}}, \tag{11}$$

where $\alpha = 0.20^{+0.12}_{-0.13}$ and $E_\mathrm{C} = 5.5^{+0.7}_{-0.6}$ MeV. The cumulative spectrum is a rough approximation because of the effects due to atmospheric absorption from different source regions and due to the direction-dependent detector response which in the cumulative spectrum are smeared out. For analysis of instrumental effects and their impact on energy spectra see [87].

The fluence distribution can be represented with a power law with an index of -2.2 to -2.4 [83, 88]. Therefore, there is no typical observed TGF fluence. However, for a reference we can consider a typical TGF fluence at the threshold level of *AGILE* which is around $0.05\,\mathrm{ph\,cm^{-2}}$ over the full energy range of *AGILE*/MCAL $0.3 - 30$ MeV and this typical fluence is emitted over an average duration T_{50} of less than $100\,\mu s$ (M. Marisaldi, private communication) [84]. The normalization K corresponding to this fluence integrated over $0.3-30$ MeV and within $100\,\mu s$ is $K = 123\,\mathrm{ph\,cm^{-2}s^{-1}MeV^{-1}}$. We assume this normalization in our MC simulations. The spectrum extrapolated to 100 keV is shown in Figure 38 with the shaded region corresponding to 68 % CL which was calculated using MC simulations and the aforementioned values of α and E_C parameters with their uncertainties. We assume that the published uncertainties of α and E_C correspond to 68 % CL. Normalization K was kept fixed because it corresponds to the fluence detection threshold of TGFs by *AGILE*.

[4] https://www.ssdc.asi.it/mcal3tgfcat/

4.3 Components of Cosmic, Albedo and Trapped Particle Radiation

There are several external background components at Low-Earth Orbits (LEO) which need to be considered in a study of the expected detected background count rate by an instrument with large field-of-view (FOV). The various components include extragalactic gamma-rays, cosmic-ray particles, secondary gamma-rays and particles produced in the Earth's atmosphere and the Galactic gamma emission. For overview see publications Refs. Jursa1985, Armstrong1992, Gehrels1992, Dean2003, Barth2003, Mizuno2004, Zombeck2007, Fioretti2012, Campana2013, Xapsos2013, Zabori2018, Cumani2019, Mate2019. The following subsections describe each component in detail and Fig. 40 shows a comparison of the in-orbit expected background fluxes which we use in our Geant4 simulations involving the mass model of one 3U *CAMELOT* CubeSat and its detectors.

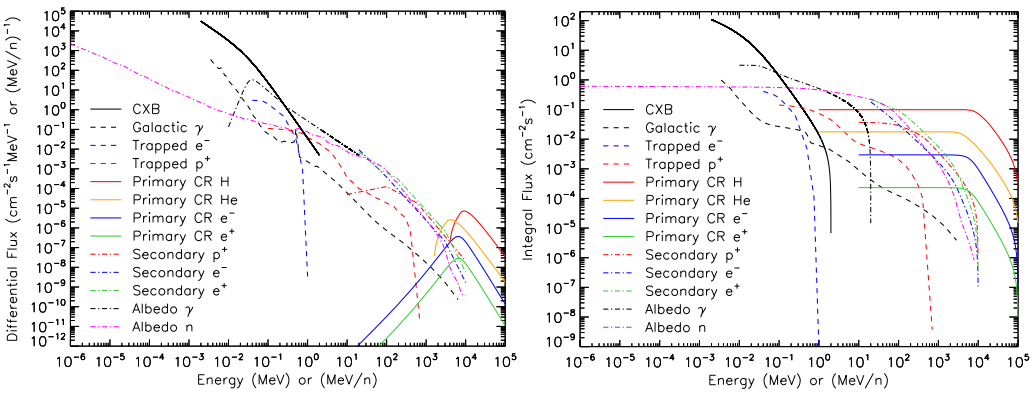

Figure 40: An overview of various background components. *Left:* The differential photon flux multiplied by the solid angles of the incident radiation valid for the expected altitude of the satellite of 500 km and for all-sky field-of-view. Trapped particle, primary CR H and He fluxes are for the orbital inclination $i = 20°$. Primary CR e^- and e^+ fluxes are for the geomagnetic latitude $\theta_M = 29.6°$. Secondary p^+ flux was obtained from the combination of data for 0.3 rad $\leq \theta_M \leq$ 0.4 rad and for 1.0 $\leq$ L-shell $\leq$ 1.7, where L-shell is the McIlwain L-parameter. Secondary e^- and e^+ fluxes were obtained from the combination of data for 0 rad $\leq \theta_M \leq$ 0.3 rad and for 1.0 $\leq$ L-shell $\leq$ 1.2. Albedo γ flux is for $i = 20.6°$. Albedo n is for cutoff rigidity $R_{cut} = 5$ GV or $\theta_M = 37°$. Details are described in Sec. 4.3. *Right:* The integral photon flux for the same models also multiplied by the same solid angles.[38]

4.4 Cosmic X-ray/γ-ray Background

The cosmic X-ray/γ-ray background (CXB) was discovered by a sounding rocket in 1962 [89]. It is nearly isotropic emission detected over a wide range of energies from few keV to few 100 GeV [90, 91, 92, 93, 94, 95, 96, 97, 98, 99, 100, 101, 102, 103, 104, 105, 106, 107, 108, 109]. It is composed of high-energy emission from various extragalactic sources (active galactic nuclei, quasi-stellar objects, supernovae Ia, galaxy clusters, starburst galaxies, X-ray binaries, hot intergalactic gas) [110, 111, 112, 113, 114, 115, 116, 117, 98, 99, 118, 104, 119, 120, 121, 122]. Some authors also argue that the diffuse γ-ray radiation originates in Cosmic Microwave Background [123] being inverse Compton scattered on cosmic-ray electrons [124, 125].

There are several empirical models used to describe the measured flux [90, 96, 126, 104, 127]. In our simulations we compare two models: the model introduced by Gruber et al. (1999) [126] and the one derived by Ajello et al. (2008) [104] (see Sec. 4.10).

The Gruber et al. (1999) model [126] fits the low-energy as well as the high-energy part of the CXB measurements obtained by *HEAO-1* [128], *CGRO*/COMPTEL and *CGRO*/EGRET [129] instruments across a wide energy range spanning from 3 keV to 100 GeV. This empirical model is used as a standard in modeling of the CXB flux for planning space missions. The differential photon flux $F(E) \equiv dN/dE$ in units of $\mathrm{ph\,cm^{-2}s^{-1}sr^{-1}keV^{-1}}$ is: for energies $E = 3 - 60\,\mathrm{keV}$

$$F(E) = 7.877 \left(\frac{E}{1\,\mathrm{keV}}\right)^{-1.29} e^{-\frac{E}{41.13\,\mathrm{keV}}} \tag{12}$$

and for energies $E > 60\,\mathrm{keV}$ it is

$$F(E) = \frac{0.0259}{60}\left(\frac{E}{60\,\mathrm{keV}}\right)^{-6.5} + \frac{0.504}{60}\left(\frac{E}{60\,\mathrm{keV}}\right)^{-2.58} + \frac{0.0288}{60}\left(\frac{E}{60\,\mathrm{keV}}\right)^{-2.05}. \tag{13}$$

Ajello et al. (2008)[104] derived a CXB model which is in a good agreement with measurements from *Swift*/BAT[104], *HEAO-1*[126], *INTEGRAL*[101], *BeppoSAX*[102] instruments and other missions in the 2 keV – 2 MeV energy range. The differential photon flux $F(E) \equiv dN/dE$ in units of $\mathrm{ph\,cm^{-2}s^{-1}sr^{-1}keV^{-1}}$ is:

$$F(E) = \frac{C}{(E/E_\mathrm{B})^{\Gamma_1} + (E/E_\mathrm{B})^{\Gamma_2}}, \tag{14}$$

where the parameters with $1\,\sigma$ errors are $C = (10.15 \pm 0.80) \times 10^{-2}$, $\Gamma_1 = 1.32 \pm 0.018$, $\Gamma_2 = 2.88 \pm 0.015$ and $E_\mathrm{B} = 29.99 \pm 1.1\,\mathrm{keV}$.

The CXB flux is omnidirectional and for 500 km altitude it irradiates a satellite from a solid angle of 8.64 sr (3.93 sr are occulted by the Earth). The CXB spectra for different models, including the two previously discussed, are shown in Figure 41. The integral flux, i.e. the integrated flux for energies above a given energy threshold, for the Gruber et al. (1999) model [126] and for $E > 10$ keV is 30.3 ph cm^{-2}s^{-1} whereas for the Ajello et al. (2008) model the integral flux at the same low-energy threshold is 33.7 ph cm^{-2}s^{-1}.

Concerning the *CAMELOT* CubeSats, the detectors are 5 mm thick CsI(Tl) scintillators (as described in Sec. 4.7) with effective area having maximum at $\sim$ 100 keV (see Figure 55). The scintillator is relatively transparent to gamma-rays above 2 MeV. For example the effective area at 1 MeV is a factor of about 7 lower than at 100 keV. Although some gamma-rays can cause pair-production or Compton scatter in the material of the satellite and then lower-energy gamma-rays can reach the scintillator, the CXB flux above 2 MeV is much lower than at few tens of keV or at 100 keV. Therefore, the high-energy gamma-ray component (above few MeV) included in the Gruber et al. (1999) model [126] is not essential for the *CAMELOT*'s detectors.

Ajello et al. (2008)[104] discusses that the normalization of the *Swift*/BAT CXB spectrum at 30 keV (CXB peak) is $\sim$ 8 % higher than the *HEAO-1*[126] measurement and consistent with the *INTEGRAL*[101] one. Also, the *HEAO-1* measurement has 10 % precision at the CXB peak. Therefore, we use both CXB models to simulate the expected detected background by *CAMELOT*, however, for a more detailed analysis, e.g. detected count rate as a function of energy threshold, we choose a more conservative approach and use the Ajello et al. (2008) model which gives $\sim$ 9 % higher integral flux in the energy range of $20 - 500$ keV, which is approximately the sensitivity range of *CAMELOT*'s detectors.

4.5 Galactic Emission

The Galactic gamma emission [130, 131] which consists of diffuse continuum [132] and resolved sources has been widely observed by many instruments, e.g. by *SAS-2* [133, 134, 93, 135], *OSO-3* [136], *COS B* [137, 135], *INTEGRAL* [138, 101, 139, 140, 107, 141, 142] satellites, COMPTEL, EGRET and OSSE instruments [143, 98, 144, 145, 146] aboard the *CGRO* satellite, *Fermi*/LAT [109, 147, 148, 149], *RXTE*/PCA [150] and *Swift*/BAT [151] instruments.

For our MC simulations (Sec. 4.10) we took the X-ray/gamma-ray fluxes of the inner Galactic region from Figures 10 and 11 as published in Ref. Turler2010 in EF_{E} flux density representation. Ref. Turler2010

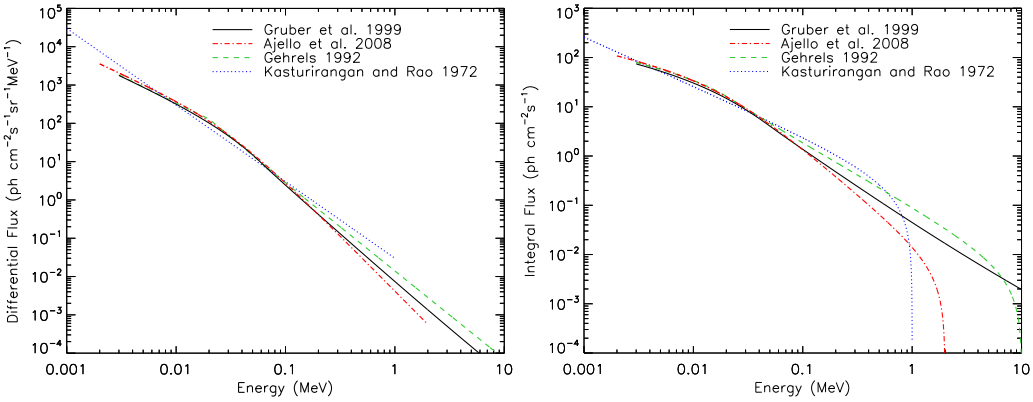

Figure 41: The CXB spectra for different models. *Left:* The differential photon flux. *Right:* The integral photon flux for the same models. The integral flux is multiplied by a solid angle of the radiation illuminating the satellite at 500 km altitude.[38]

summarizes measurements from *RXTE*/PCA[138], *INTEGRAL*/SPI[140], *INTEGRAL*/IBIS[138, 107], *CGRO*/COMPTEL[139] and *CGRO*/EGRET[139] instruments and show the fluxes renormalized to the central radian of the Milky Way defined by $|l| < 30°$ and $|b| < 15°$.

The emission from the inner Galactic region irradiates a satellite from the solid angle of 0.542 sr. The differential and integral photon spectra are shown in Figure 42. The integral flux for energy $E > 10\,\mathrm{keV}$ is $0.2\,\mathrm{ph\,cm^{-2}s^{-1}}$. However, it should be noted that the Galactic emission is not spatially uniform and has a brightness structure peaked at the Galactic center (see e.g. Ref. Mayer-Hasselwander1982). Figure 42 also shows measurements done by *Fermi*/LAT taken from Figure 4 of Ref. Strong2011 for smaller region of $|l| < 30°$ and $|b| < 10°$. We do not include these *Fermi*/LAT measurements in our MC simulations because the region of the inner Galaxy is not exactly the same as the one used for the other aforementioned data sets. This does not effect our results because the photon flux at these very high energies is very small.

4.5.1 Trapped Particles

The fluxes of the geomagnetically trapped electrons and protons inside the inner van Allen radiation belt [152] contribute to the overall detected instrumental background and they are especially important when a satellite at LEO passes the polar regions [153, 154] or the South Atlantic Anomaly (SAA). Details about the Earth's radiation environment can be found in, for example, Ref. Roederer1970, Jursa1985, Kivelson1995, Walt2005,

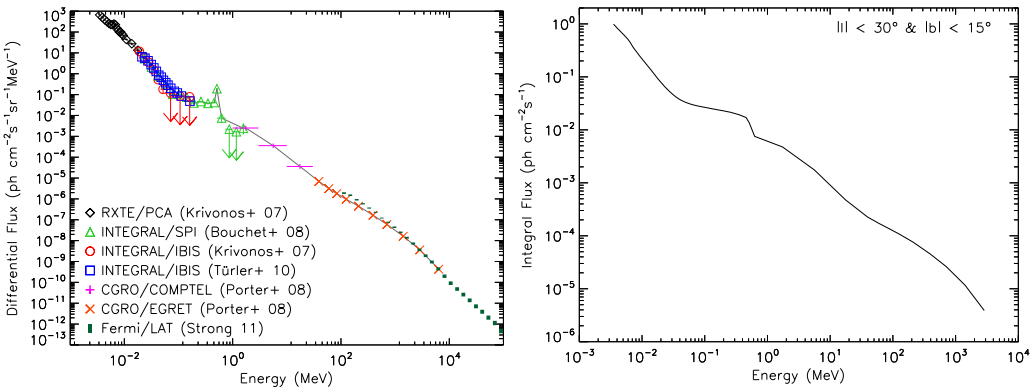

Figure 42: The spectra of the inner Galaxy emission. *Left:* The differential photon flux observed by *RXTE*/PCA[138], *INTEGRAL*/SPI[140], *INTEGRAL*/IBIS[138, 107], *CGRO*/COMPTEL[139] and *CGRO*/EGRET[139] for the region defined by $|l| < 30°$, $|b| < 15°$ and *Fermi*/LAT[147] for the region defined by $|l| < 30°$, $|b| < 10°$. The gray solid line marks the flux taken for our MC simulations. *Right:* The integral photon flux. The integral flux is multiplied by 0.542 sr solid angle of the inner Galaxy region. [38]

Zombeck2007, Qin2014, Adriani2015, Benghin2018, Shprits2018.

Several models describing the fluxes of the trapped particles around the Earth based on measurements from tens of space missions have been developed over last decades, e.g. the National Aeronautics and Space Administration's (NASA) AE8 [155, 156] and AP8 [157, 156] models, European Space Agency's (ESA) AE-8 update ESA-SEE1 [158] model, or model based on the measurements from Proton/Electron Telescope (PET) onboard the Solar, Anomalous, and Magnetospheric Particle Explorer (*SAMPEX*) satellite - the *SAMPEX*/PET PSB97 model [159].

In our on-board background simulations (Sec. 4.10) we employ the fluxes of trapped electrons and protons prescribed by the recent AE9 and AP9 models [160, 161, 162, 163] as they are implemented in ESA's SPace ENVironment Information System (SPENVIS[5]). SPENVIS is an Internet interface to models of the space environment and its effects, developed by a consortium led by the Royal Belgian Institute for Space Aeronomy (BIRA-IASB). The AE9/AP9 models are based on 33 satellite data sets from 1976 to 2011 and they are provided by the U.S. Air Force Research Laboratory (AFRL) in their software package [6].

[5] www.spenvis.oma.be

[6] https://www.vdl.afrl.af.mil/programs/ae9ap9

The AE8/AP8 models available in SPENVIS or in the AFRL package do not compute fluxes lower than 1 particle $\mathrm{cm}^{-2}\mathrm{s}^{-1}$, whereas the AE9/AP9 models provide fluxes below 1 particle $\mathrm{cm}^{-2}\mathrm{s}^{-1}$. That is important for our purpose, because we want to estimate the detected background count rate in the regions outside SAA and polar regions. However, the current version of the AP9/AE9 model provided in SPENVIS is recommended for evaluation purposes only and there have been reported discrepancies between the AE8/AP8 and the AE9/AP9 models, e.g. see Ref. Pich2017 and references therein.

Figure 43 shows orbit-averaged integral spectra of trapped electrons and protons averaged over 60 days of orbiting (including SAA passages) with sampling of 10 s obtained for different models by the AFRL package. It demonstrates that AE9/AP9 models gives much higher electron and proton fluxes compared to the AE8/AP8 models at low inclinations and low energies. Therefore the detected background count rate due to the trapped particles calculated by our simulation may overestimate the real level.

Figure 44 shows maps of integral fluxes (flux of particles with energy higher than E) of trapped electrons and protons for the AE9 and AP9 models with Monte Carlo (MC) mode, 100 runs and 50 % confidence level (CL) at 500 km altitude. The MC mode accounts for the uncertainty due to the random perturbations as well as the flux variations due to the space weather [160].

We calculated spectra of electrons and protons averaged along the trajectory of a satellite at altitude 500 km with inclination of $i = 20°$ and orbiting 30 days with flux sampling every 10 s. Only the regions with the integral flux ≤ 10 particle $\mathrm{cm}^{-2}\mathrm{s}^{-1}$ were used ($E > 40$ keV for electrons and $E > 100$ keV for protons). These conditions give a duty cycle, i.e. the fraction of time a satellite spends in a region with particle flux lower than a given flux threshold, of 80 %. If the orbital inclination is 90° the duty cycle would be 76 %. Details about the duty cycle for different inclinations, altitudes at LEO, flux and energy thresholds for AE8, AP8, AE9 and AP9 models can be found in Ref. Ripa2020.

In this way we were able to obtain averaged spectra outside of SAA. The differential and integral fluxes are shown in Figure 45. The differential flux per solid angle has been calculated for simplicity assuming the radiation is illuminating a satellite isotropically from the solid angle of 4π because, for example, in case of *CAMELOT* satellites the pointing strategy is not established yet. The trapped particles can collide with the detector from various directions and we are interested in a long-term average. Also, the assumption of the isotropy of the trapped particle flux is a simplification because of the well known "East-West" effect [164]. The integral flux for

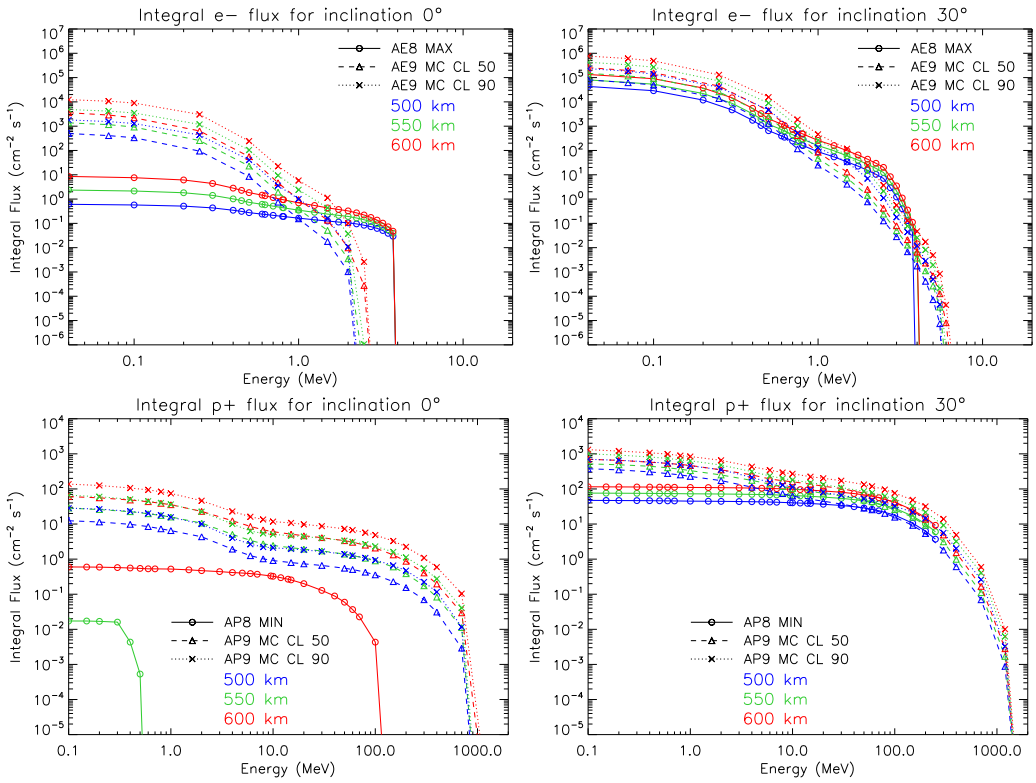

Figure 43: Comparison of orbit-averaged integral fluxes of trapped electron models AE8 MAX (solar maximum), AE9 50 % and 90 % confidence levels (CL); and trapped proton models AP8 MIN (solar minimum), AP9 50 % and 90 % CL for different altitudes and inclinations.[38]

trapped electrons is $0.41\,\mathrm{cm}^{-2}\mathrm{s}^{-1}$ ($E > 40\,\mathrm{keV}$) and for trapped protons is $0.14\,\mathrm{cm}^{-2}\mathrm{s}^{-1}$ ($E > 100\,\mathrm{keV}$) as obtained from the model.

4.5.2 Primary Cosmic-Rays

The spectra of the primary particles of cosmic-rays (CRs) used in our simulations are described below. For the assumed 500 km altitude the fluxes irradiate the satellite from the solid angle of 8.64 sr. The origin of CRs is extraterrestrial consisting mainly of protons. Other components of CRs such as electrons, positrons, alpha particles and nuclei of heavier elements have been detected as well. Several experiments have been performed to study CRs, e.g. AMS [165, 166], BESS [167], CREAM [168], *Fermi*/LAT [169, 170], HESS [171], PAMELA [172].

We considered two models for the spectra of primary particles. The first one was the ISO-15390[173] model, which is the international standard for

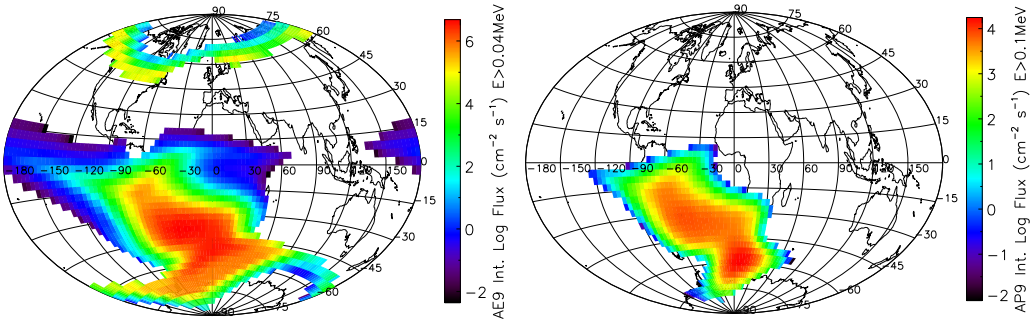

Figure 44: A map of the integral flux of geomagnetically trapped electrons (left) and protons (right) at 500 km altitude according to the AE9 and AP9 models (MC mode, 50 % CL), respectively, obtained by the AFRL package.[38]

estimating the radiation impact of CRs on hardware in space and which describes the fluxes of primary protons, alpha particles, and nuclei of heavier elements.

The second model which we considered was described by Mizuno et al. (2004), see Ref. Mizuno2004, and it was based on measurements done by BESS and AMS experiments (see also Ref. Campana2013). The flux of primary CRs in interstellar space can be modeled by a power law function:

$$F_{\mathrm{U}}(E_{\mathrm{k}}) = A \left[\frac{R(E_{\mathrm{k}})}{\mathrm{GV}} \right]^{-a}, \tag{15}$$

where $R = pc/Ze$ is the rigidity of the particle as a function of its kinetic energy E_{k} or momentum p and its charge Ze. The flux constant A and the exponent a are determined by fitting of the following model to the measurements.

The flux of primary CRs for a given phase of the solar cycle and in a given position in the Earth's magnetosphere according to the model described in Ref. Mizuno2004 is:

$$F(E_{\mathrm{k}}) = F_{\mathrm{U}}(E_{\mathrm{k}} + Ze\phi) \times F_{\mathrm{M}}(E_{\mathrm{k}}, M, Z, \phi) \times F_{\mathrm{C}}(R, h, \theta_{\mathrm{M}}), \tag{16}$$

where M is the mass of the particle, ϕ is a solar modulation potential, h is the altitude of the satellite's orbit and θ_{M} is the geomagnetic latitude.

By applying an effective shift of energy of the primary particles due to the deceleration by the solar wind the first function F_{U} in Eq. (16) gets form:

$$F_{\mathrm{U}}(E_{\mathrm{k}} + Ze\phi) = A \left[\frac{R(E_{\mathrm{k}} + Ze\phi)}{\mathrm{GV}} \right]^{-a}. \tag{17}$$

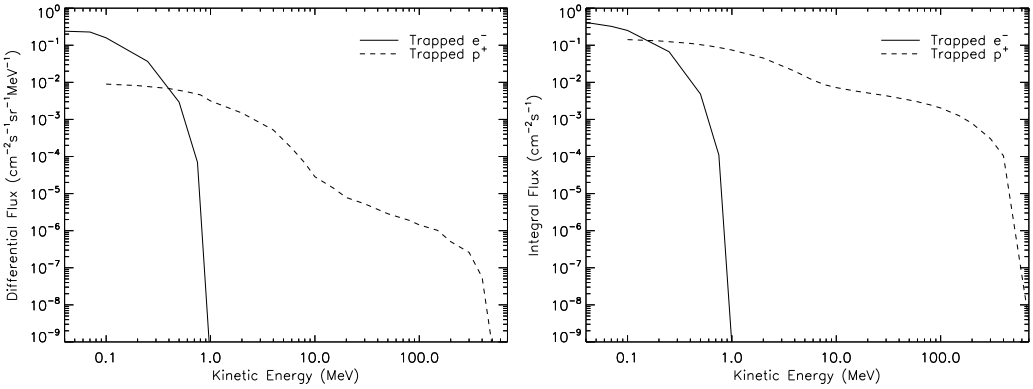

Figure 45: Differential fluxes (left) and integral fluxes (right) of geomagnetically trapped electrons and protons averaged along the trajectory of a satellite at altitude 500 km with inclination $i = 20°$ and orbiting 30 days. The models were AE9 and AP9, MC mode with 100 runs and the spectra were derived from the 50 % CL of the fluxes. Only the regions avoiding SAA were used. The differential flux per solid angle has been calculated for simplicity assuming the radiation is illuminating the satellite isotropically from the solid angle of 4π.[38]

The second function F_{M} accounts for the flux modulation due to the solar cycle and is given by:

$$F_{\mathrm{M}}(E_{\mathrm{k}}, M, Z, \phi) = \frac{(E_{\mathrm{k}} + Mc^2)^2 - (Mc^2)^2}{(E_{\mathrm{k}} + Ze\phi + Mc^2)^2 - (Mc^2)^2}\,, \tag{18}$$

where the solar modulation potential varies between $\phi = 0.55\,\mathrm{GV}$ for solar minimum and $\phi = 1.10\,\mathrm{GV}$ for solar maximum.

The third term is the geomagnetic cutoff function F_{C} given by:

$$F_{\mathrm{C}}(R, h, \theta_{\mathrm{M}}) = \frac{1}{1 + (R/R_{\mathrm{cut}})^{-r}}\,, \tag{19}$$

where $r = 12$ for p^+ or α particles, $r = 6$ for e^- or e^+, and the cutoff rigidity R_{cut} is given by the Störmer equation [174]:

$$R_{\mathrm{cut}} = 14.5 \left(1 + \frac{h}{R_{\mathrm{E}}}\right)^{-2} \cos^4\theta_{\mathrm{M}}\,\mathrm{GV}, \tag{20}$$

where R_{E} is the Earth's radius.

We want to estimate a long term average of the flux, therefore we assume that the flux has uniform angular distribution for the zenith angle $0° \leq \theta \leq$

$\theta_{\rm cut}$ and the flux is zero for $\theta_{\rm cut} \leq \theta \leq 180°$, where the $\theta_{\rm cut}$ is the zenith angle of the Earth's horizon and it is 112° for the altitude of 500 km.

Primary Protons and Alpha Particles

For primary protons and alpha particles we compared the model ISO-15390 and the model Mizuno et al. (2004) described in Ref. Mizuno2004.

For the ISO-15390 model we employed SPENVIS where we generated the orbit-averaged spectra for circular orbit with inclination $i = 20°$, duration 30 days and sampling 60 s. The following parameters setting was applied: solar minimum activity (May 1996), magnetic shielding on, stormy and quite magnetosphere, Størmer with eccentric dipole method and magnetic field moment unchanged.

For the model described in Ref. Mizuno2004 we used the following parameters: solar minimum cycle with the solar modulation potential $\phi = 0.55\,\mathrm{GV}$, altitude 500 km, and two geomagnetic latitudes $\theta_{\rm M} = 0°$ and $\theta_{\rm M} = 20°$ (orbital inclination) + 9.6° (tilt between the geomagnetic dipole axis and the Earth's rotational axis).

For primary protons the values of $A = 23.9\,\mathrm{particle\,m^{-2}s^{-1}sr^{-1}MeV^{-1}}$ and $a = 2.83$ were adopted. For primary alpha particles the values of $A = 1.5\,\mathrm{particle\,m^{-2}s^{-1}sr^{-1}MeV^{-1}}$ and $a = 2.77$ were adopted.

Figure 46 and 47 show fluxes of primary protons and alpha particles, respectively, at 500 km altitude obtained by the ISO-15390 model for quiet and stormy magnetosphere and obtained by the Mizuno et al. (2004) model for fixed geomagnetic latitudes $\theta_{\rm M} = 0°$ and $\theta_{\rm M} = 29.6°$. This model predicts the integral flux of primary protons of kinetic energies $E > 1\,\mathrm{GeV}$ being $0.11\,\mathrm{cm^{-2}s^{-1}}$ (for $\theta_{\rm M} = 0°$) or $0.29\,\mathrm{cm^{-2}s^{-1}}$ (for $\theta_{\rm M} = 29.6°$) and the integral flux of primary alpha particles of kinetic energies per nucleon $E > 1\,\mathrm{GeV/n}$ being $0.016\,\mathrm{cm^{-2}s^{-1}}$ (for $\theta_{\rm M} = 0°$) or $0.041\,\mathrm{cm^{-2}s^{-1}}$ ($\theta_{\rm M} = 29.6°$).

For our Geant4 simulations of the expected on-board background by a *CAMELOT* satellite (Sec. 4.10) we use the ISO-15390 model with stormy magnetosphere, because it is the international standard for CR flux and because it was obtained for a fixed orbital inclination of $i = 20°$ meaning crossing the range of geomagnetic latitudes between $-30°$ and $\sim 32°$[7], [175]. It predicts the integral flux of primary protons of kinetic energies $E > 1\,\mathrm{GeV}$ being $0.095\,\mathrm{cm^{-2}s^{-1}}$ (for quite magnetosphere) or $0.099\,\mathrm{cm^{-2}s^{-1}}$ (for stormy magnetosphere) and the integral flux of primary alpha particles of kinetic energies per nucleon $E > 1\,\mathrm{GeV/n}$ being $0.017\,\mathrm{cm^{-2}s^{-1}}$ (for quite magnetosphere) or $0.018\,\mathrm{cm^{-2}s^{-1}}$ (for stormy magnetosphere).

Primary Electrons and Positrons

For the spectra of the primary e^- and e^+ we used the model described

[7] https://spawx.nwra.com/spawx/maps/maplats.html

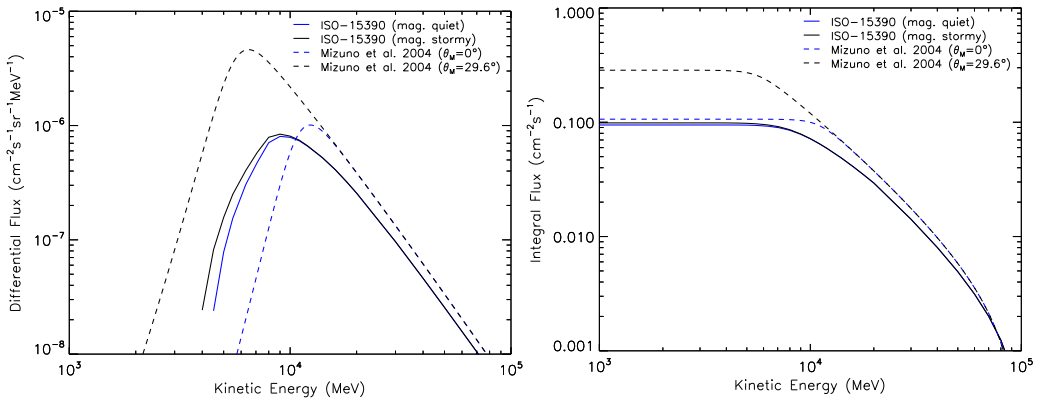

Figure 46: Differential fluxes (left) and integral fluxes (right) of primary CR protons. Solid lines mark model introduced by Mizuno et al. (2004) [100] for geomagnetic latitudes $\theta_{\mathrm{M}} = 0°$ and $\theta_{\mathrm{M}} = 29.6°$. Dashed lines mark galactic CR model ISO-15390 [173] for quiet and stormy magnetosphere obtained in SPENVIS for circular orbit with inclination $i = 20°$. Spectra from both models were obtained for altitude of 500 km. The integral flux is multiplied by a solid angle corresponding to the radiation illuminating the satellite at this altitude. [38]

by Mizuno et al. (2004) [100] with references to the flux measurements by [176, 177]. The measurements of the ratio of positrons and electrons $e^+/(e^-+e^+)$ are given by [178, 166].

We adopt the model of the primary interstellar particles Eq. (15) with following parameters: $A = 0.65\,\mathrm{particle\,m^{-2}s^{-1}sr^{-1}MeV^{-1}}$ and $a = 3.3$ for electrons and $A = 0.051\,\mathrm{particle\,m^{-2}s^{-1}sr^{-1}MeV^{-1}}$ with the same exponent a for positrons.

Same as for the primary protons and alpha particles we used the following conditions of the solar cycle and the orbit: solar minimum with the modulation potential $\phi = 0.55\,\mathrm{GV}$, altitude 500 km, and two geomagnetic latitudes $\theta_{\mathrm{M}} = 0°$ and $\theta_{\mathrm{M}} = 29.6°$. Figure 48 and 49 show the fluxes of the primary electrons and positrons.

For our simulations of the expected detected background (Sec. 4.10) we use the spectrum for $\theta_{\mathrm{M}} = 29.6°$. We also assume that the angular distribution of the flux is incoming uniformly from the solid angle unocculted by the Earth. Then the integral flux ($E > 1\,\mathrm{GeV}$) for e^- is $3 \times 10^{-3}\,\mathrm{cm^{-2}s^{-1}}$ and for e^+ it is $2.3 \times 10^{-4}\,\mathrm{cm^{-2}s^{-1}}$.

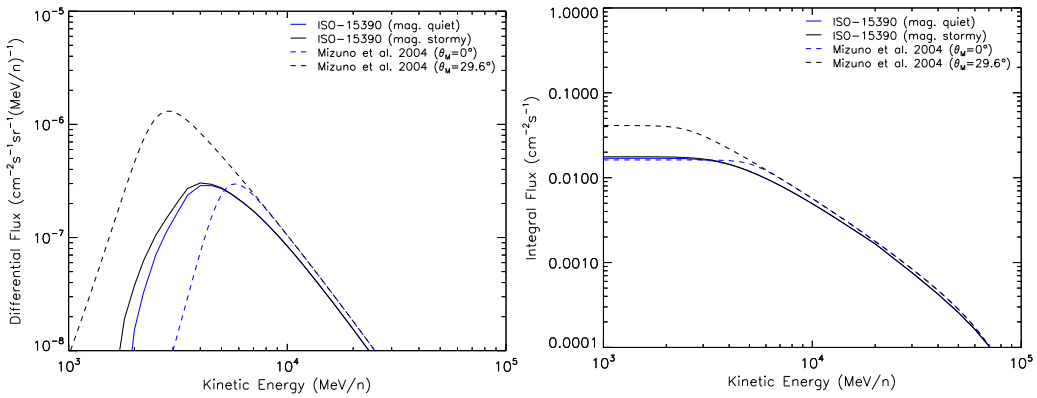

Figure 47: Differential fluxes (left) and integral fluxes (right) of primary CR alpha particles as a function of energy per nucleon. Solid lines mark model introduced by Mizuno et al. (2004) [100] for geomagnetic latitudes $\theta_{\mathrm{M}} = 0°$ and $\theta_{\mathrm{M}} = 29.6°$. Dashed lines mark galactic CR model ISO-15390 [173] for quiet and stormy magnetosphere obtained in SPENVIS for circular orbit with inclination $i = 20°$. Spectra from both models were obtained for altitude of 500 km. The integral flux is multiplied by a solid angle corresponding to the radiation illuminating the satellite at this altitude.[38]

4.6 Secondary Particles and Radiation

Secondary (albedo) particles and radiation are created by interaction of primary CRs with the Earth's atmosphere [179, 103].

Secondary Protons For secondary p^+ and for energy above 100 MeV we use the model [100] based on the measurements done by the Alpha Magnetic Spectrometer (AMS) [165] from 380 km altitude for the geomagnetic latitude 0.3 rad $\leq \theta_{\mathrm{M}} \leq$ 0.4 rad. For energy below 100 MeV we use the fit to *MITA*/NINA-2 data [180] from 450 km altitude and for 1.0 $\leq$ L-shell $\leq$ 1.7, where L-shell is the McIlwain L-parameter [181]. For details see the LAT Technical Note LAT-TD-08316-01 [**?**] of the *Fermi* satellite [182]. There is only small dependence of the flux on altitude [180, 183] therefore it can be used as an approximation to the flux at altitude of 500 km.

The differential flux $F(E)$ in units of particle $\mathrm{m}^{-2}\mathrm{s}^{-1}\mathrm{sr}^{-1}\mathrm{MeV}^{-1}$ is modeled as:

$$F(E) = \begin{cases} 0.1\left(\frac{E}{100\,\mathrm{MeV}}\right)^{0.4} & \text{for } 10\,\mathrm{MeV} \leq E \leq 100\,\mathrm{MeV} \\ 0.1\left(\frac{E}{100\,\mathrm{MeV}}\right)^{-1.09} & \text{for } 100\,\mathrm{MeV} \leq E \leq E_{\mathrm{brk}} \\ 0.1\left(\frac{E_{\mathrm{brk}}}{100\,\mathrm{MeV}}\right)^{-1.09}\left(\frac{E}{E_{\mathrm{brk}}}\right)^{-2.4} & \text{for } E \geq E_{\mathrm{brk}}, \end{cases} \tag{21}$$

where $E_{\mathrm{brk}} = 600\,\mathrm{MeV}$ is break energy. Figure 50 shows the modeled flux

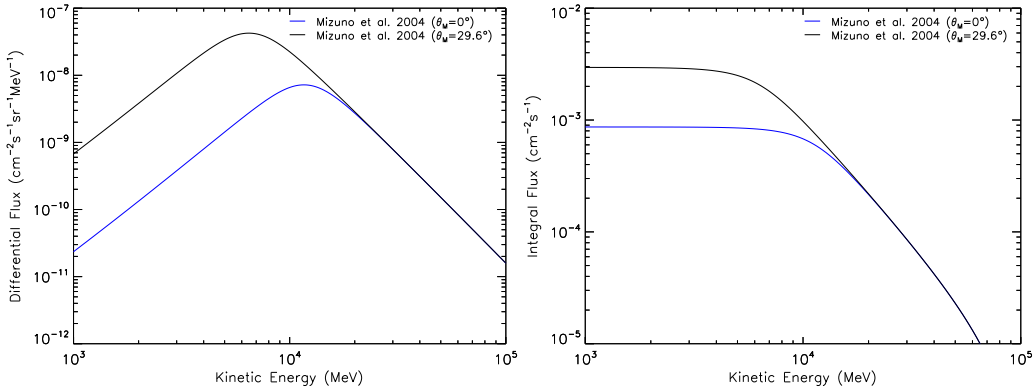

Figure 48: Differential fluxes (left) and integral fluxes (right) of primary CR electrons modeled by Mizuno et al. (2004) [100] for geomagnetic latitudes $\theta_{\mathrm{M}} = 0°$ and $\theta_{\mathrm{M}} = 29.6°$ and altitude of 500 km. The integral flux is multiplied by a solid angle corresponding to the radiation illuminating the satellite at this altitude.[38]

together with the measurements.

The same model is used for the upward and downward component of the flux and it is assumed that secondary protons irradiate the satellite from the solid angle of 4π sr without zenith-angle dependence of the flux. The integral flux ($E \geq 10\,\mathrm{MeV}$) is $0.037\,\mathrm{cm}^{-2}\mathrm{s}^{-1}$.

4.6.1 Secondary Electrons and Positrons

For secondary e^- and e^+ and for energy above 100 MeV we use the model [100] based on the measurements done by AMS [165] from 380 km altitude for the geomagnetic latitude $0 \leq \theta_{\mathrm{M}} \leq 0.3$ rad. For energy below 100 MeV we use the fit to *Mir*/MARIA-2 data [184, 185] from 400 km altitude and for $1.0 \leq$ L-shell ≤ 1.2. For details see the LAT Technical Note LAT-TD-08316-01 [**?**].

For secondary e^- the differential flux $F(E)$ in units of particle $\mathrm{m}^{-2}\mathrm{s}^{-1}\mathrm{sr}^{-1}\mathrm{MeV}^{-1}$ is modeled as:

$$F(E) = \begin{cases} 0.3\left(\frac{E}{100\,\mathrm{MeV}}\right)^{-2.0} & \text{for } 10\,\mathrm{MeV} \leq E \leq 100\,\mathrm{MeV} \\ 0.3\left(\frac{E}{100\,\mathrm{MeV}}\right)^{-2.2} & \text{for } 100\,\mathrm{MeV} \leq E \leq E_{\mathrm{brk}} \\ 0.3\left(\frac{E_{\mathrm{brk}}}{100\,\mathrm{MeV}}\right)^{-2.2}\left(\frac{E}{E_{\mathrm{brk}}}\right)^{-4.0} & \text{for } E \geq E_{\mathrm{brk}}, \end{cases} \tag{22}$$

where the break energy $E_{\mathrm{brk}} = 3000\,\mathrm{MeV}$. Figure 51 shows the modeled flux together with the measurements.

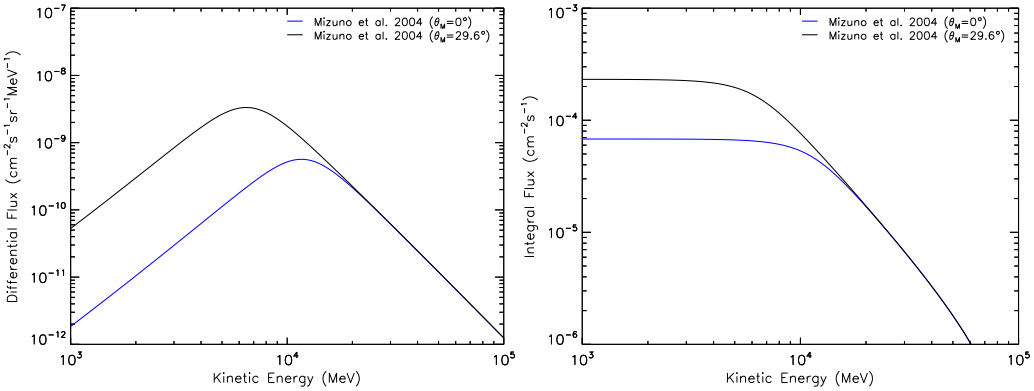

Figure 49: Differential fluxes (left) and integral fluxes (right) of primary CR positrons modeled by Mizuno et al. (2004) [100] for geomagnetic latitudes $\theta_{\mathrm{M}} = 0°$ and $\theta_{\mathrm{M}} = 29.6°$ and altitude of 500 km. The integral flux is multiplied by a solid angle corresponding to the radiation illuminating the satellite at this altitude.[38]

For secondary e^+ the differential flux $F(E)$ in units of particle $\mathrm{m}^{-2}\mathrm{s}^{-1}\mathrm{sr}^{-1}\mathrm{MeV}^{-1}$ is modeled as:

$$F(E) = \begin{cases} 20\left(\frac{E}{10\,\mathrm{MeV}}\right)^{-1.77} & \text{for } 10\,\mathrm{MeV} \leq E \leq 60\,\mathrm{MeV} \\ 0.833\left(\frac{E}{60\,\mathrm{MeV}}\right)^{-1.0} & \text{for } 60\,\mathrm{MeV} \leq E \leq 178\,\mathrm{MeV} \\ 1.0\left(\frac{E}{100\,\mathrm{MeV}}\right)^{-2.2} & \text{for } 178\,\mathrm{MeV} \leq E \leq E_{\mathrm{brk}} \\ 1.0\left(\frac{E_{\mathrm{brk}}}{100\,\mathrm{MeV}}\right)^{-2.2}\left(\frac{E}{E_{\mathrm{brk}}}\right)^{-4.0} & \text{for } E \geq E_{\mathrm{brk}}, \end{cases} \tag{23}$$

where the break energy $E_{\mathrm{brk}} = 3000\,\mathrm{MeV}$. Figure 52 shows the modeled flux together with the measurements.

The same model is used for the upward and downward component of the flux and it is assumed that secondary e^- and e^+ irradiate the satellite from the solid angle of 4π sr without zenith-angle dependence of the flux. The integral flux ($E \geq 20\,\mathrm{MeV}$) is $0.18\,\mathrm{cm}^{-2}\mathrm{s}^{-1}$ for e^- and $0.23\,\mathrm{cm}^{-2}\mathrm{s}^{-1}$ for e^+.

Albedo X-rays/γ-rays The secondary (albedo) X-ray and γ-ray flux is due to interaction of primary CRs with the Earth's atmosphere. It is produced by decay of π^0 pions (mainly above 50 MeV), by bremsstrahlung from primary and secondary electrons (mainly below 50 MeV), and also by the reflection of CXB and it has been measured by several satellites and balloon experiments [91, 186, 92, 94, 187, 188, 96, 189, 99, 100, 190, 103, 101, 191, 107, 127]. The intensity depends on the geomagnetic latitude [192].

We utilize a model reported by Ajello et al. (2008) [104] based on the *Swift*/BAT measurements from $\sim$ 20 keV to $\sim$ 200 keV for altitude of

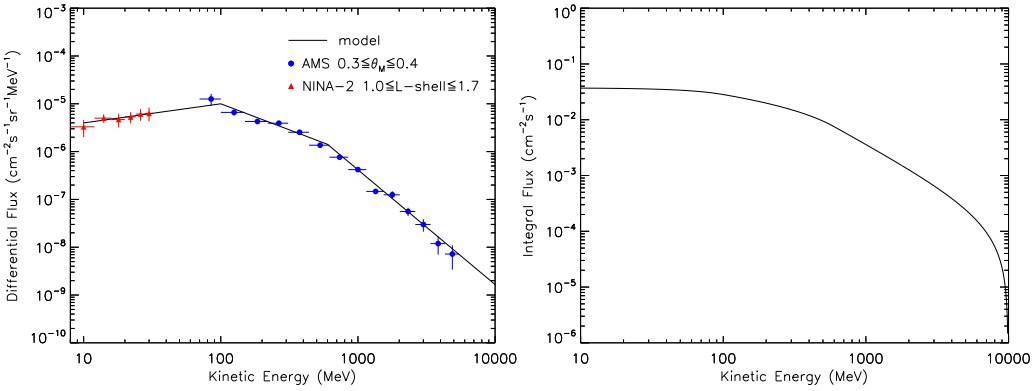

Figure 50: Differential fluxes (left) and integral fluxes (right) of secondary protons modeled by Eq. (21) are marked by the black curve. The measurements from the AMS and *MITA*/NINA-2 experiments for the given geomagnetic position are shown as well. The integral flux is multiplied by the solid angle of 4π sr.[38]

$h \sim 550$ km and inclination of $i = 20.6°$ and which is compatible with measurements from BeppoSAX[102] ($h \sim 580$ km and $i = 4°$) and after some corrections with measurements by the polar-orbiting satellite 1972-076B [192] ($h \sim 750$ km). MC simulations show that this model is a very good approximation of the Earth albedo X-ray emission up to 300 keV [193, 104].

We assume the Ajello et al. (2008) model [104] in the energy range of $E = 10 - 300$ keV and hence the differential photon flux $F(E)$ given by Eq. (14), where the model parameters and their 90 % CL errors are Γ_1=-5 (fixed), Γ_2=1.72±0.08, E_b=33.7±3.5 keV and $C = 1.48^{+0.6}_{-0.3} \times 10^{-2}$.

For higher energies we assume a model reported by Mizuno et al. (2004) [100] based on measurements by *1972-076B* and *Kosmos 461* satellites [192, 187] and by balloon flights [186, 188]. Particularly, we consider only energies $E = 0.3 - 20$ MeV where we assume the differential photon flux $F(E)$ in units of ph cm^{-2}s^{-1}sr^{-1}keV^{-1} to be a simple power law function:

$$F(E) = 719 \left(\frac{E}{\mathrm{keV}}\right)^{-1.34}, \tag{24}$$

where we normalized the Mizuno et al. (2004) model [100], their Eq. (21), in order to obtain the same differential flux at 300 keV as predicted by the Ajello et al. (2008) model [104]. The spectrum is shown in Figure 53. According to MC simulations [193] there is only a small dependence of the albedo X-ray flux ($25 - 300$ keV) on the solar cycle and geomagnetic latitude below $\sim 20°$ for an instrument at LEO with large FOV which covers the whole terrestrial disc.

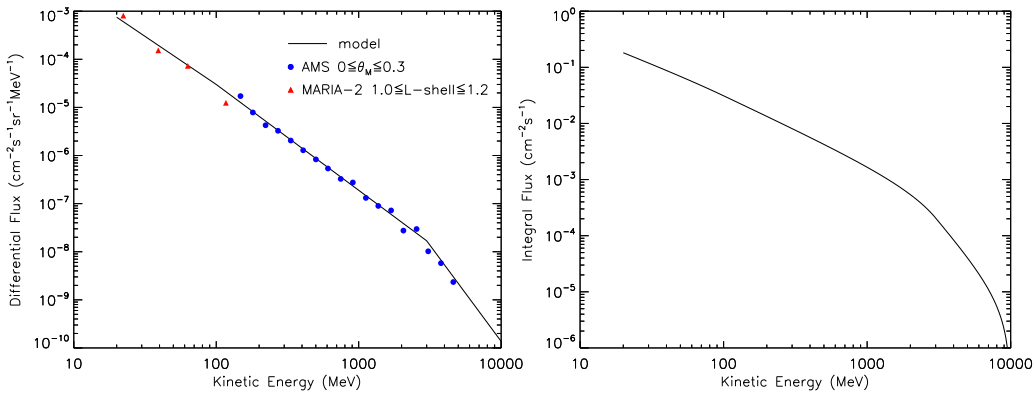

Figure 51: Differential fluxes (left) and integral fluxes (right) of secondary electrons modeled by Eq. (22) are marked by the black curve. The measurements from the AMS and *Mir*/MARIA-2 experiments for the given geomagnetic position are shown as well. The integral flux is multiplied by the solid angle of 4π sr.[38]

A zenith angle dependence of the albedo γ-ray flux has been measured in the $1 - 10\,\mathrm{MeV}$ region [92, 91, 100]. See also Ref. Kraushaar1972, Thompson1974, Imhof1976, Ryan1979, Thompson1981, Akyuz1997, Dean2003, Petry2005, Abdo2009 and references therein for the zenith angle dependence of the albedo γ-ray flux at other energies. In the energy range $25 - 300\,\mathrm{keV}$, covered by the Ajello et al. (2008) model, the MC simulations [193] suggest that there is no zenith angle dependence. However, for the higher-energy part $0.3 - 20\,\mathrm{MeV}$ one can expect a zenith angle dependence of the flux. In case of *CAMELOT* satellites, they will have detectors with all-sky FOV which can be illuminated from various directions and we are interested in a long term average flux, therefore, for simplicity, we do not assume any zenith angle dependence in our Geant4 simulations involving a *CAMELOT* satellite mass model.

At an altitude of 500 km the photons would irradiate the satellite from a solid angle of 3.93 sr. The integral flux ($E > 10\,\mathrm{keV}$) is $3.1\,\mathrm{ph\,cm^{-2}s^{-1}}$.

Albedo Neutrons The albedo neutrons are produced in hadronic showers created by CRs interacting with the Earth's atmosphere and they can reach a satellite at LEO [127]. For the albedo neutrons we use the predictions of the QinetiQ Atmospheric Radiation Model (QARM), based on MC radiation transport code, as reported in the ESA document ECSS-E-ST-10-04C [**?**]. The model has been validated against several measurements [194, 195, 196, 197] and is also consistent with other MC simulations[198, 199]. For other models and measurements

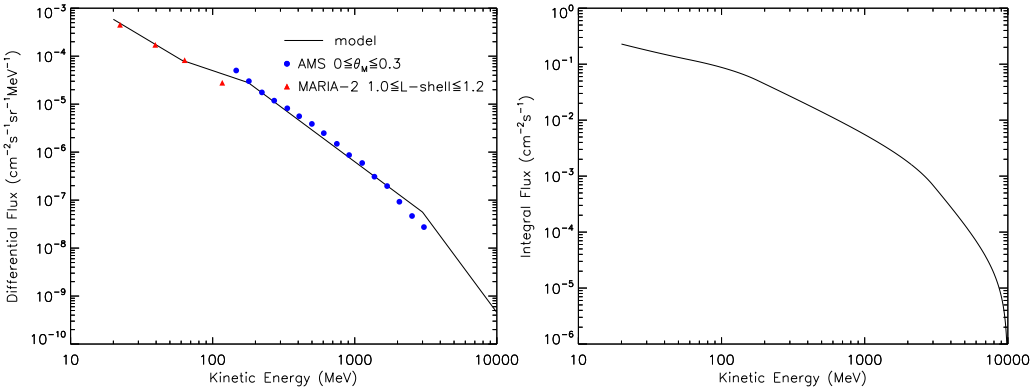

Figure 52: Differential fluxes (left) and integral fluxes (right) of secondary positrons modeled by Eq. (23) are marked by the black curve. The measurements from the AMS and *Mir*/MARIA-2 experiments for the given geomagnetic position are shown as well. The integral flux is multiplied by the solid angle of 4π sr.[38]

see Ref. Lingenfelter1963,Dean2003,Kole2015,Cumani2019 and references therein.

Figure 54 shows the fluxes of secondary neutrons for the cutoff rigidity $R_{\rm cut} = 16.6\,{\rm GV}$ and $R_{\rm cut} = 5\,{\rm GV}$ for solar minimum. The fluxes were scaled from the altitude of 100 km to 500 km as described in the ECSS-E-ST-10-04C document.

In our simulations of the expected detected background (Sec. 4.10) we use the spectrum for the solar minimum and for the cutoff rigidity $R_{\rm cut} = 5\,{\rm GV}$ which corresponds to the geomagnetic latitude $\theta_{\rm M} = 37°$ following from the Störmer equation Eq. (20) or latitude between $\sim 30°$ and $\sim 50°$, see Figure 7 of Ref. smart2005.

The integral flux is $0.61\,{\rm cm}^{-2}{\rm s}^{-1}$ for $E > 1\,{\rm eV}$, for $R_{\rm cut} = 5\,{\rm GV}$, altitude of 500 km and assuming that all neutrons are coming from the solid angle of 3.93 sr which corresponds to the angular size of the Earth observed from that altitude.

4.7 The *CAMELOT* CubeSats

We study in particular the expected on-board background for the proposed *CAMELOT* mission, expected to be launched to LEO with the main objective of all-sky monitoring and timing-based localization of GRBs. The at least nine satellites are considered to be placed on orbits with altitude of $\sim 500 - 600\,{\rm km}$ with inclination of 53° or at Sun-synchronous orbits of inclination 97.6° [40]. One of the options for the *CAMELOT* satellite

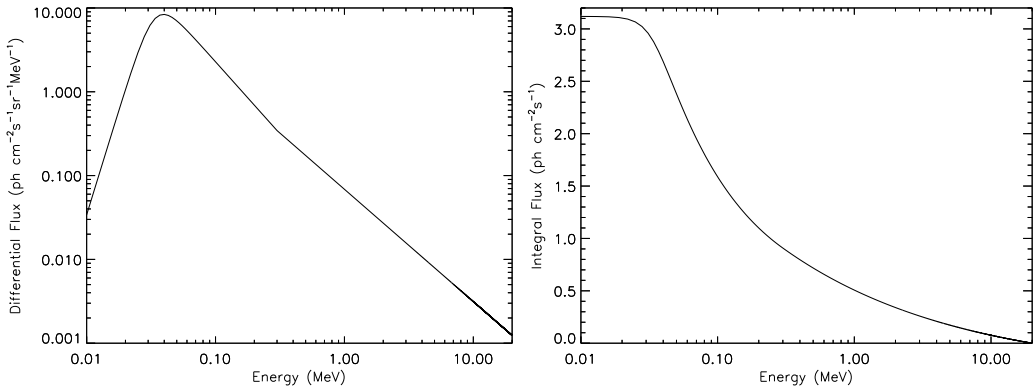

Figure 53: The albedo X-ray/γ-ray spectra. For energies from 10 keV to 300 keV modeled by Ajello et al. (2008) and for energies from 300 keV to 20 MeV modeled by Eq. (24). *Left:* The differential photon flux. *Right:* The integral photon flux integrated up to 20 MeV. The integral flux is multiplied by the Earth-subtended solid angle of 3.93 sr at an altitude of 500 km.[38]

platform is the one being developed by C3S LLC in Budapest, therefore we apply its mass model in our Geant4 simulations.

4.7.1 The Detector System

The constellation of at least nine 3U CubeSats is proposed to be equipped with large and thin CsI(Tl) scintillators, of size $75 \times 150 \times 5$ mm^3 each, read out by Hamamatsu Multi-Pixel Photon Counters (MPPC). There would most likely be four scintillators on each satellite with two scintillators placed on two neighbouring sides of the satellite. The scintillators will be wrapped in the enhanced specular reflector (ESR) foil and enclosed in a support structure made either from aluminium or carbon fiber-reinforced plastic (CFRP). For details about the detector system see Ref. Ohno2018. The effective area of four detectors on board one *CAMELOT* satellite as a function of energy and for different directions, obtained from Geant4 simulations, is shown in Figure 55.

In order to understand and characterize the behaviour of the large-area CsI(Tl) scintillator detector and the MPPC readout, an experimental setup was built in Hiroshima, Japan. The experimental setup provided vital information for the simulation, mostly for the position dependence of the scintillator effective light yield. Different γ sources were used in the tests, mostly an ^{241}Am source [200].

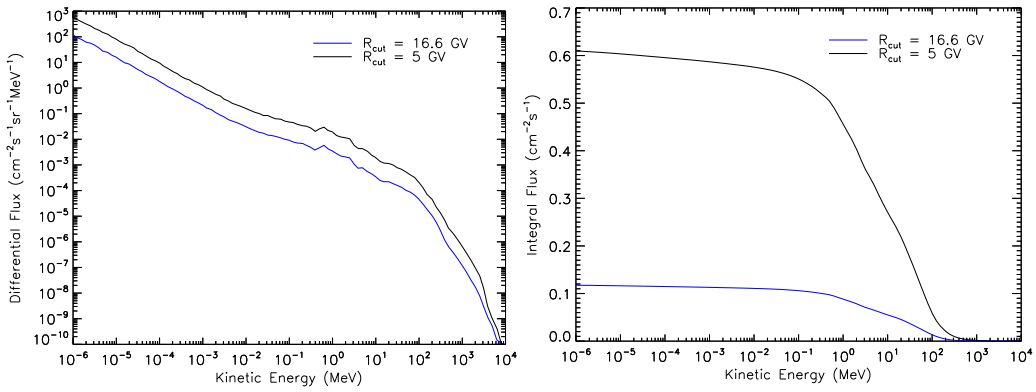

Figure 54: Differential fluxes (left) and integral fluxes (right) of albedo neutrons predicted by the QARM model for two values of cutoff rigidity and scaled to the altitude of 500 km. The integral flux is multiplied by the solid angle of 3.93 sr.[38]

4.8 Validation of Geant4 Simulation and Calibration of Detector's Optical Parameters

A dedicated set of measurements were carried out with ^{241}Am γ source with an activity of 471 kBq which was collimated to irradiate different positions on the scintillator. The experiments were carried out with a single MPPC very similarly to the measurements presented in Ref. Torigoe2019. The collimation was achieved with two lead sheets each containing holes in nine positions. In order to obtain the optical parameters of the scintillators as precisely as possible, the effect of reflectivity and absorption length on photon light yield was maximized by utilizing one MPPC in the middle of the shorter side of the scintillator. Spectra were recorded in nine cases by moving the ^{241}Am source in the nine positions where holes were present. Figure 56 shows the simulation of the experimental set-up.

The measured and simulated spectra for the irradiation point closest to the MPPC and in the farthest corner are compared in Figure 57. The same number of X-rays were simulated, which were emitted in 2 minutes of data acquisition for each spectrum. The difference between these spectra is the largest of all. The main reason for this is the difference in the mean path of optical photons, which is the shortest when the source is in front of the MPPC and the largest when the source is placed in the corner.

Two distinct peaks are visible in the measured and simulated spectra (Figure 57). The peak with the higher energy corresponds to the ^{241}Am γ peak at 59.5 keV. The lower-energy one is the K_α X-ray fluoresence peak of the Cesium in the scintillator [200]. The results of the Geant4 simulation were

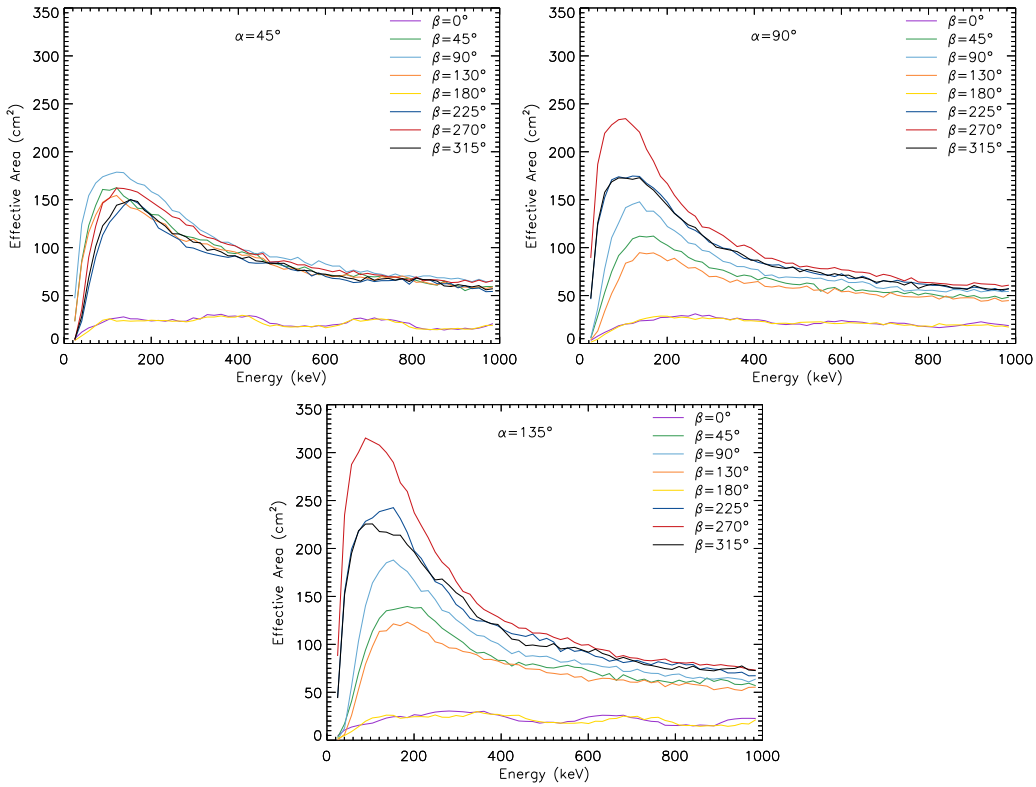

Figure 55: The effective area of four detectors on board one *CAMELOT* satellite as a function of energy and for different angles α and β defining the source direction in respect to the satellite. For the exact definition of these angles see Fig. 59.[38]

smeared by a Gaussian function with a standard deviation σ of 5 channels for the closest point of irradiation and 15 channels for the farthest to match them with the measured ones. The histogram of the number of photons detected in the simulation were scaled up by 1.35 and 1.39 respectively to match them with the measurements. This way assuming a linear detector response, all amplification factors were treated together. The fact that the scaling factor is almost the same for all parts of the scintillator translates to a good light collection efficiency. The main aim of the measurements was to determine the number of detected optical photons for an energy deposition of 1 keV in the scintillator (on average). For the measurements taken at the farthest position from the MPPC the 59.5 keV ^{241}Am peak was at ADC channel 180. The number of detected photons in the simulations had to be scaled up by roughly 1.37 to match the measurements. For the measurements taken at the closest point to the MPPC the same scaling parameter was used. For the

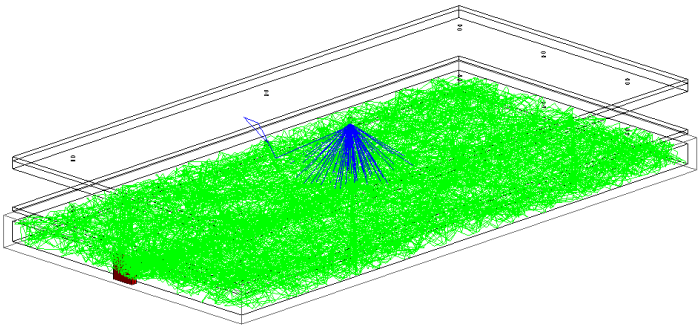

Figure 56: Simulation of 50 X-rays originating from a collimated X-ray source placed above the middle of the scintillator. Blue tracks are X-rays, green tracks are optical photons and the red square marks the MPPC. Only optical photons which are detected were drawn.[38]

farthest position from the MPPC this implicates that an energy deposition of 1 keV yields 4.11 detected optical photons on average.

The light yield in the simulation for the scintillator was fixed at 54 photons/keV, which is the yield for CsI(Tl) scintillators produced by Saint-Gobain[8] which is similar to our scintillator produced by AMCRYS[9]. The absorption length and the reflectivity of the surface of the scintillator was varied until the simulation agreed with the measurements for the two extreme spectra, the one in front of the MPPC and the one in the farthest corner. The best fitting reflectivity was 99.99 % and the absorption length determined from the fit was 60 cm. These values were used in the later simulations.

In this way of calibration the energy resolution and noise of the electronics are taken into account in the simulations. Although pileup is not included but during operation we do not expect such high count rates from regular sources where it could be relevant.

4.9 Description of Geant4 Simulations

A Geant4 MC based simulation was developed in order to understand how the *CAMELOT* CubeSat constellation would detect γ-rays originating from short GRBs, long GRBs and TGFs. This required dedicated simulations

[8] https://www.crystals.saint-gobain.com/products/crystal-scintillation
[9] http://www.amcrys.com

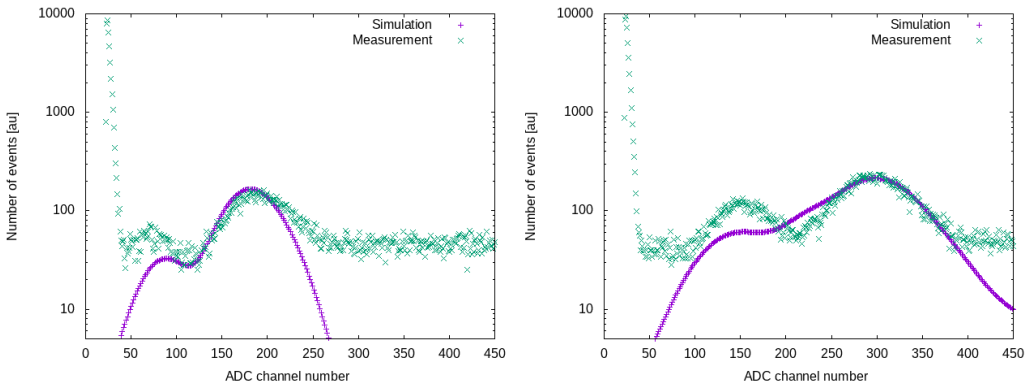

Figure 57: Simulated spectra of number of scintillation photons detected compared to the measurements. At the closest position to the MPPC (right) and at one of the farthest corners (left). The simulated spectra were smeard by 5 and 15 channels respectively.[38]

of each background component as well as response to the γ-ray sources and calculation of the signal-to-noise ratio. The repository containing the simulation source code and analysis code are shared on GitHub (with a GNU General Public License). [10,11].

As the first step, the experimental setup that was used to calibrate the optical parameters of the CsI(Tl) scintillator – the γ-ray detector of the satellite – that with its casing was implemented in Geant4. Details are in Sec. 4.8. Afterwards the complex CAD model (Sec. 4.9.2) of the satellite – consisting of 7 modules, each with a given average material composition – was imported to Geant4 with CADMESH [201]. Four scintillators, each read out by 8 MPPCs were placed on two sides of the satellite.

In order to keep computation time at a reasonable level, the simulation of each primary particle is stopped if the number of detected optical photons reaches 10 000. Heavy ions can create several hundred thousands of scintillation photons. This limitation made it possible to run the codes on personal computers with a few cores. The signal of the 8 MPPCs is planned to be grouped into two groups of 4 MPPCs. In the following simulations the signal of all 32 MPPCs belonging to the four scintillators is summed up. This way we give a conservative signal-to-noise ratio (SNR) estimation since a more sophisticated trigger algorithm will decrease the chance of the background to exceed the threshold in each channel. The energy deposition is calculated from the number of detected optical photons. As described in

[10] https://github.com/ggalgoczi/szimulacio/tree/master/Bck_4.10.6
[11] https://github.com/ggalgoczi/szimulacio/tree/master/GRB

Sec. 4.8, 1 keV energy deposition corresponds to 4.11 optical photons detected in the simulation. This corresponds to an overall photon detection efficiency of 7% which is expected given the large size of the scintillator, the small sensitive area of MPPCs and the quantum efficiency of the MPPCs which depends on the scintillation light wavelength.

4.9.1 Directional and Positional Distribution of Primary Particles

The simulations presented in this section can be split into two main groups based on whether we are simulating the source of the background or an astrophysical source. The latter are the target objects: sGRBs, lGRBs and TGFs, which can be considered as point sources very far away, therefore photons coming from these sources are treated in the simulations as parallel.

The other main group is the background (eg. CXB, albedo particles, trapped electrons). The background particles and γ-rays mainly hit the satellite from large solid angles or isotropically. The pointing strategy of the *CAMELOT* satellites is not established yet and the detector has all-sky FOV. We are interested in the estimation of a long-term average background at the regions of low geomagnetic latitude and outside SAA as mentioned in Sec. 4.3. Therefore, as an approximation, we assume that all components of the background flux of particles and γ-rays irradiate the satellite isotropically.

In order to realize this in the simulations the background particles were placed randomly on a sphere with a radius R around the model of the satellite. To maintain isotropy their direction was also randomly chosen. To boost up the simulation a source biasing was used [202] to limit the number of primary particles simulated to the ones which would hit the satellite. Due to the biasing, the number of detections in the simulation had to be normalized to determine the detection rate we would actually have.

The expected detection rate $N_{\mathrm{det.rate}}$ for *CAMELOT* in space can be calculated as follows [202]:

$$N_{\mathrm{det.rate}} = 4 f_{\Omega} \pi^2 R^2 (\sin^2\theta_{\mathrm{max}} - \sin^2\theta_{\mathrm{min}}) \Phi N_{\mathrm{det.sim}} / N_{\mathrm{prim}}, \tag{25}$$

where $f_{\Omega} = \Omega/4\pi$ is the factor which takes into account the solid angle Ω of the type of the background. For instance albedo particles originate only from the atmosphere beneath the satellite. This corresponds to 3.95 sr for our orbit. R is the radius of the sphere upon which the primary particles are distributed. This radius needs to be much larger than the size of the target object to maintain isotropy. θ stands for the angle that is formed by the initial direction of the simulated primary particle and the vector pointing to the center of the satellite from the origin of the simulated primary particle. By limiting θ we are able to simulate only those particles which

would hit the satellite. In our case $R = 50\,\mathrm{m}$. θ_{min} and θ_{max} are the upper and lower bounds for the chosen interval of the emission angle in the simulation. In our case $\theta_{\mathrm{min}} = 0$ and $\theta_{\mathrm{max}} = 0.5729°$. Φ is the flux in units of $\mathrm{cm}^{-2}\mathrm{s}^{-1}\mathrm{sr}^{-1}$. $N_{\mathrm{det.sim}}$ is the number of detections in the given simulation. N_{prim} is the number of primary particles shot in the simulation. The factor $\pi^2 R^2(\sin^2\theta_{\mathrm{max}} - \sin^2\theta_{\mathrm{min}}) = 24668\,\mathrm{cm}^2$. Table 4 summarizes the values of Ω and the normalization factor $f_{\mathrm{norm}} = 4\Omega\pi^2 R^2(\sin^2\theta_{\mathrm{max}} - \sin^2\theta_{\mathrm{min}})$ for the background models described in Sec. 4.3.

	CXB and primary CR	Galactic γ	Trapped and charged secondary particles	Albedo γ and n^0
Ω (sr)	8.64	0.542	4π	3.93
f_{norm} ($\mathrm{cm}^2\mathrm{sr}$)	8.525×10^5	5.348×10^4	1.240×10^6	3.878×10^5

Table 4: Summary of solid angles Ω of background flux and normalization factor f_{norm}. [38]

4.9.2 Satellite's Mass Model

In order to include all parts of the satellite including even the smallest volumes, the detailed CAD model of the satellite was read into Geant4 directly with CADMESH [201] that utilizes TETGEN [203] and ASSIMP[12] software libraries to directly read in STL files into Geant4. The satellite consists of seven modules including the structure of the satellite, the communications module, the payload etc. The only volume that was not included were the antennas.

Name of module	mass [g]	Type of material	Mass ratio [%]
ADCS	710	Aluminum 6061-T6	50
		Copper Electric	25
		Glass Borosilicate	25
COM	90	Stainless Steel	2
		Brass Generic	25
		Aluminum 7075-T73	40
		FR4 Glass-Epoxy sheet	33
EPS	750	FR4 Glass-Epoxy sheet	25
		Aluminum 6061-T6	75
OBC	50	FR4 Glass-Epoxy sheet	100
STRU	980	Aluminum 6061-T6	100
SP	570	Solar Panel	100
Payload	100	Aluminum 7075-T73	100

Table 5: The mass ratio of materials that are used for the satellite (Courtesy of C3S LLC).[38]

The material of each of the volumes was averaged (as described in Table 5. and Table 6.). Figure 59 shows the mass model of the *CAMELOT* satellite. Figure 58 presents the individual volumes of the satellite.

[12] http://www.assimp.org

Material name												
Aluminum 6061-T6	Al	96.90	Mg	1.20	Si	0.80	Fe	0.70	Cu	0.40		
Aluminum 7075-T73	Al	88.60	Zn	6.10	Mg	2.90	Cu	2.00	Si	0.40		
Stainless Steel	Fe	66.50	Cr	20.00	Ni	10.50	Mn	2.00	Si	1.00		
Copper Electric	Cu	100.00										
Glass Borosilicate	Si	42.10	O	54.80	B	3.10						
FR4 Glass-Epoxy	Si	23.39	O	36.02	C	37.04	H	3.55				
Brass Generic	Cu	85.00	Zn	15.00								
Solar Panel	Ge	38.00	Si	24.00	O	20.00	C	13.00	H	4.00	B	1.00

Table 6: The chemical composition of materials in mass fraction that are used for the satellite (Courtesy of C3S LLC).[38]

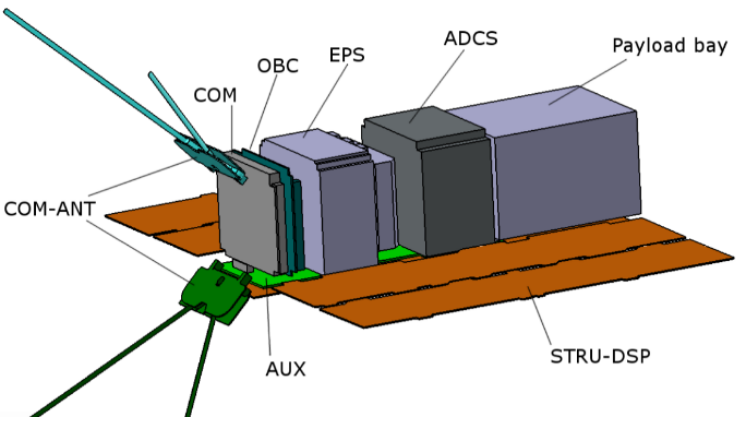

Figure 58: The individual volumes of the simulated satellite. The CAD model of the satellite was read into Geant4 and 4 scintillators (not displayed on this figure) with their respective read out were placed on two sides of the satellite (Courtesy of C3S LLC).[38]

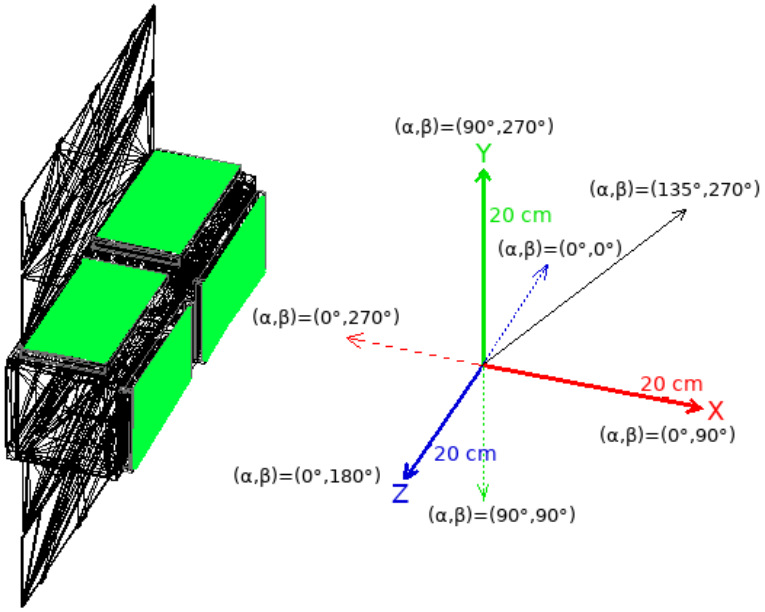

Figure 59: The mass model used for the Geant4 simulations. The CAD model of the satellite was read into Geant4 and 4 scintillators (green rectangles) with their respective read out were placed on two sides of the satellite. The angles α and β refer to the angles shown in the figure of the detector's effective area. β is rotation around the Y axis, counted from the -Z axis and it increases towards +X axis. α is rotation around the Z axis, counted from the +X axis and increasing towards -Y axis. The highest effective area is for a source at direction (α, β) = (135°, 270°).[38]

4.10 Results of Geant4 Simulations

4.10.1 Response to Each External Background Components

In this section the simulation results of the satellite response to each of 14 external background components is presented. The results are for one *CAMELOT* satellite. The count rate is summed for all detectors. By far the most relevant background is CXB. Therefore we chose to simulate two different CXB models introduced by Gruber et al. (1999) [126] and Ajello et al. (2008) [104] described in Sec. 4.4. The input energy spectra of each background component used for the simulations are described in the corresponding subsection of section 4.3. The model of the satellite was irradiated isotropically as shown in Figure 60.

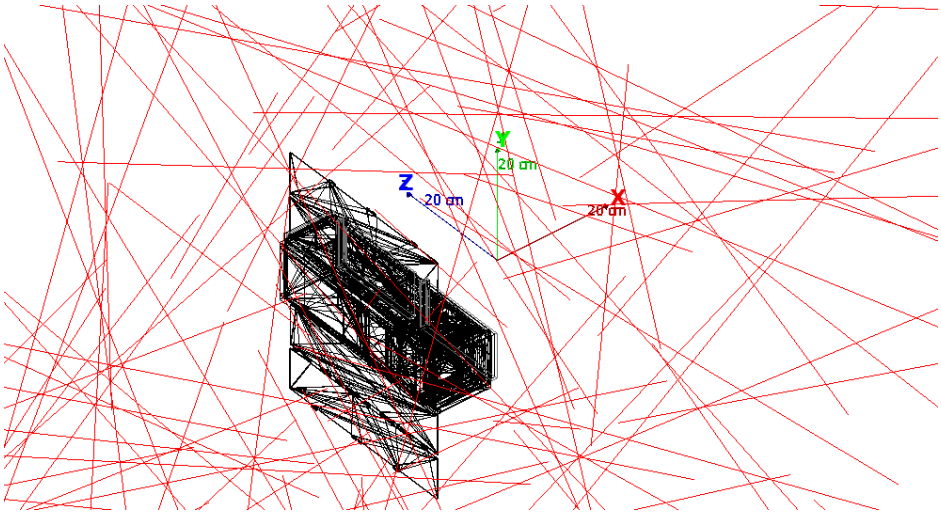

Figure 60: The mass model of the satellite is isotropically irradiated with X-rays (blue tracks). All four scintillators onboard appear green as they are filled with the tracks of optical photons which have green colour. The effect of the directional biasing (described in Sec. 4.9.1) can be seen.[38]

Four possible aluminium detector support structure (shortly detector casing or just casing) thicknesses were investigated. The same material and thickness is on all sides of the detector housing, including the back side. In order to give an idea of the contribution of each component a realistic 20 keV low-energy threshold was chosen. The five components which contribute the most to the background for the casing thickness of 0.5 mm thick Al with this low-energy threshold are: CXB ($\sim 1000 - 1100$ counts per second (cps)), albedo γ (~ 200 cps), primary CR protons (27 cps), albedo protons (45 cps)

and albedo positrons (28 cps). Tables 7 and 8 summarize the background detection rate predicted by the simulation.

Thickness (mm)	CXB A08	CXB G99	CR α	CR p^+	Galactic γ	Trapped p^+	CR e^-	CR e^+	Trapped e^-
0.5	1150	996	51	28	5.12	1.15	0.74	0.057	0.17
1.0	1020	893	49	29	3.98	0.947	0.76	0.057	0.073
1.5	890	770	51	29	4.04	0.820	0.76	0.060	0.072
2.0	858	707	51	29	3.50	0.827	0.75	0.059	0.066

Table 7: Simulated detection rate induced by cosmic and trapped particle background components. The background detection rate is in counts per second, assumes a low-energy threshold of 20 keV, and is simulated for different thicknesses of the aluminium support structure of the detector. Two spectral models described by Gruber et al. (1999) [126] and by Ajello et al. (2008) [104] (denoted as G99 and A08) were simulated for the CXB. For the primary CR p^+ and α particles we used the ISO-15390 model with stormy magnetosphere and inclination of $i = 20°$. For primary CR e^- and e^+ we used the model described by Mizuno et al. (2004) [100] for solar minimum, $\theta_M = 29.6°$. For trapped e^- and p^+ we used the AE9 and AP9 models, respectively, for inclination of $i = 20°$, MC mode and derived from the 50 % CL of the fluxes. Altitude of 500 km was chosen.[38]

By summing up the contribution of each background component we derived a total background rate of 1550 cps for 0.5 mm, 1400 cps for 1 mm, 1270 cps for 1.5 mm and 1100 cps for 2 mm of the casing thickness assuming a low-energy threshold of 20 keV. From the two CXB models simulated, the Ajello et al. (2008) model was chosen since it gives a more conservative estimate. The Ajello et al. (2008) and Gruber et al. (1999) models have integral fluxes of 33.7 ph cm^{-2}s^{-1} and 30.3 ph cm^{-2}s^{-1} for $E > 10$ keV and give background rates of 1020 cps and 893 cps for 1 mm thick Al detector casing, respectively.

The low-energy threshold onboard the *CAMELOT* satellites is planned to be a tunable parameter and changeable upon a ground command. Laboratory experiments show that low-energy threshold for our detectors is around $15 - 20$ keV. In Figure 61 the detection rate is shown for different casing thicknesses and low energy thresholds. The low energy part of the background spectrum is dominated by CXB X-rays which are stopped by thicker detector casing. The higher energy part is dominated mostly by hadrons and albedo gamma rays (hard spectrum) which can easily cross aluminium and deposit high energies in the scintillator.

Thickness (mm)	Albedo γ	Secondary e^+	Secondary e^-	Secondary p^+	Albedo n^0
0.5	208	28.2	6.32	45.5	23.8
1.0	205	27.1	8.00	43.7	22.3
1.5	192	27.4	7.95	42.5	22.3
2.0	191	28.2	7.86	43.4	21.4

Table 8: Simulated detection rate induced by background components originating in the atmosphere. The detection rate is in counts per second, assumes a low-energy threshold of 20 keV and is simulated for different thicknesses of the aluminium support structure of the detector. For secondary neutrons the spectrum for the solar minimum and for the cutoff rigidity $R_{\text{cut}} = 5\,\text{GV}$ was used.[38]

4.10.2 Simulation of a Typical Short GRB from Different Directions

In order to quantify if *CAMELOT* is capable of detecting X-ray sources we need to investigate the X-ray absorption by the satellite structures themselves. The four scintillators are placed on two sides of the satellite. Therefore the X-rays from half of the objects need to cross a certain part of the satellite before arriving to the detectors.

To quantify the X-ray absorption of the satellite and to determine the count rate expected from sGRBs, different source directions were simulated. First, the satellite was rotated around its major axis by 10° 35 times to cover all directions around this axis. Afterwards the same was repeated for the minor axis of the satellite. A 1024 ms peak spectrum of a typical sGRB was used in the simulation. Details of typical sGRB spectra are described in subsection 4.2.1.

Rotating Around Major Axis for Short GRB

The satellite was rotated around its major axis (Z in Figure 62) by 10° between each simulation. The simulated primary X-rays originated from the direction of the X axis. 0° case corresponds to the scenario when X-rays arrive perpendicular to the surface of two of the scintillators. The count rate is the highest for 45° when the angle between the direction of the photons and the surface normal of both detectors is 45°. The combined projected area of the four scintillators is the largest in this scenario. The least favored direction is 270° (see Figure 63).

In Figure 64 the spectra of two directions are shown. As expected for the least optimal direction (270°) the low energy part of the spectrum is suppressed. These are the X-ray photons which are not able to cross the material of the satellite.

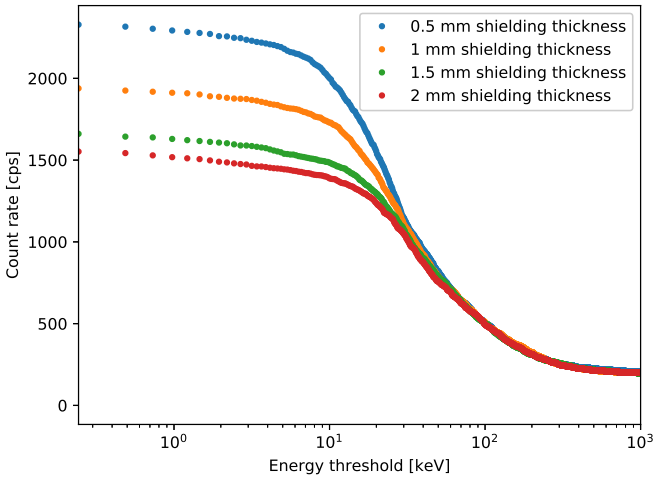

Figure 61: Background count rate for three aluminium detector support structure thicknesses versus low-energy thresholds. Above a threshold of ∼50 keV the thickness of the support structure does not change the background rate.[38]

Different low-energy thresholds are possible to be set. Therefore, it is important to understand how the count rate of X-rays from sGRBs would change by varying the low-energy threshold. In Figure 65 the count rate for the most and least optimal direction is shown depending on the low-energy threshold. Up to about 100 keV the count rate does not decrease significantly. Also it is important to notice that the direction of the source is much more important than the thickness of the detector casing.

Rotating Around Minor Axis for Short GRBs

The same procedure as described in subsection 4.10.2 was followed for investigating sGRB (for 1024 ms peak spectrum) directions around the minor axis (X in Figure 62). X-ray were simulated as a parallel beam coming from the Z direction. In Figure 66 the count rate for each direction is shown. 0° is the least optimal. It corresponds to the case when all scintillators are seen from their edge. In this case the cross-section of the four scintillators combined is 7.5 cm^2, which is about 3 % of the area in the most optimal direction during rotation around the minor axis.

Since the background for the casing thickness of 2 mm is 1100 cps, a count rate of 165 cps is required from a sGRB to be observed with a significance of 5 σ. Therefore from the directions investigated with the rotation of the

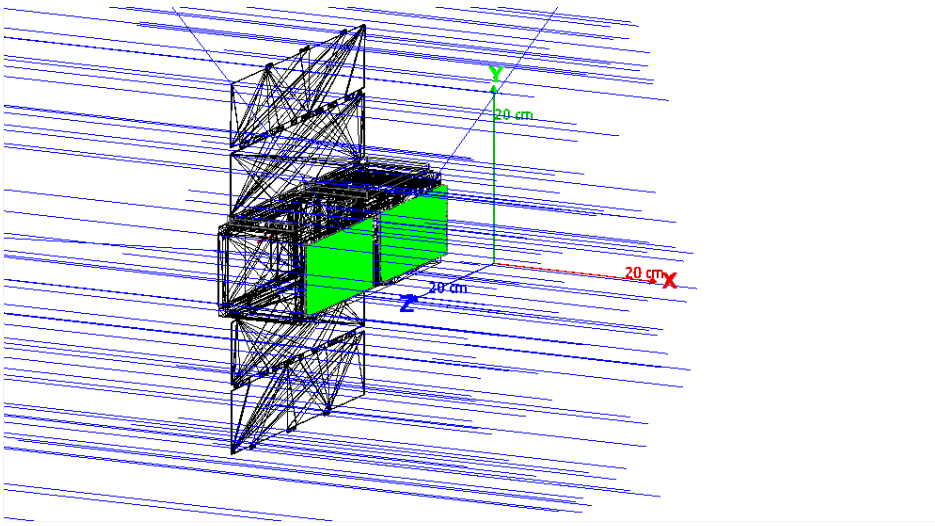

Figure 62: The satellite hit by parallel X-rays, such as the ones originating in short GRBs. Only one of the four scintillators were triggered in this case. Blue tracks are X-rays, green tracks are optical photons which were detected by the MPPCs.[38]

minor axis the interval between 50° and 150° is suitable for the detection of sGRBs.

4.10.3 Signal-to-Noise Ratio of X-ray/γ-ray Transients

For the detection of astrophysical objects, the final figure of merit is the SNR. It is important to mention that for the localization accuracy not only the SNR but also the number of detected photons is important for the cross-correlation of light curves. Electronic noise was neglected in the following calculations as the planned low-energy threshold set for detection is higher than the amplitude of the electronic noise.

Detection low-energy threshold can be set onboard the satellite. Therefore SNR was quantified for each astrophysical object in the function of low-energy threshold. The following equation was used to determine SNR:

$$SNR = \frac{\Delta t \sum_{E_1}^{E_2} f(E)}{\sqrt{\Delta t \sum_{E_1}^{E_2} g(E)}}, \tag{26}$$

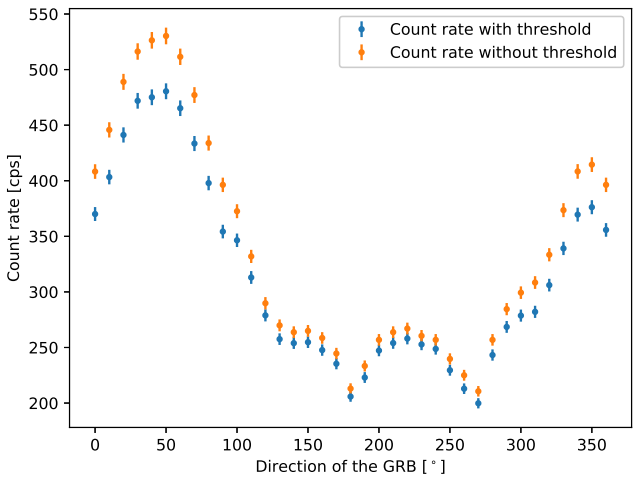

Figure 63: Count rate of a typical sGRB (for 1024 ms peak spectrum) for different source directions. The satellite was rotated around its major axis. An arbitrary but possible low-energy threshold of 20 keV was utilized. The detector support structure thickness of the scintillator was 2 mm.[38]

where $f(E)$ is the detected count rate spectrum of the signal, $g(E)$ stands for the detected count rate background spectrum, E_1 is the low-energy threshold, E_2 is the high-energy threshold and Δt is the exposure time. In our simulations we did not put boundary on the high-energy threshold, but the triggering algorithm onboard *CAMELOT* satellites will have capability to set both the low- and the high-energy thresholds.

The main aim of the *CAMELOT* mission is the detection and localization of sGRBs. Therefore it is important to understand with what significance could *CAMELOT* satellites detect these objects. Among the direction, when the satellite was rotated around its major axis SNR is the highest when the angle between X-rays from a GRB and the surface normal of both detectors is 45°. We have the lowest SNR for the angle of 270° (see Figure 63).

When the simulated typical sGRB (for 1024 ms peak spectrum) is in the most optimal direction an SNR of > 11 can be achieved. SNR stays above 10 within the low-energy detection threshold range from up to 100 keV. The thickness of the aluminium detector casing affects SNR mostly for low values of the low-energy detection thresholds, since the main background component, CXB has a rather soft spectrum. For the least optimal direction among the directions investigated an SNR of 6 can be achieved. This

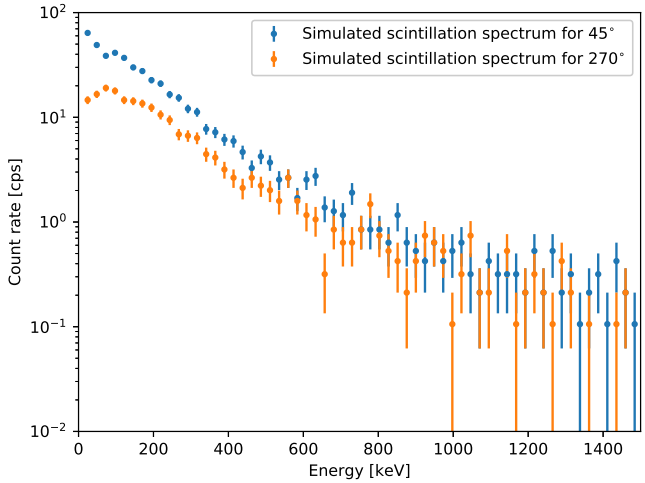

Figure 64: Typical short GRB spectra (for 1024 ms peak) for the most optimal direction and the least optimal direction among the investigated cases. The lower energy band is suppressed for 270°, since GRB X-rays need to cross the material of the satellite for this scenario to be detected. Thickness of the detector support structure was 2 mm in this case.[38]

characteristic is shown in Figure 67. The other directions, when the satellite was rotated around its minor axis (Figure. 66), are less favored. In these cases the cross section of the detectors are significantly lower.

Tables 9 and 10 summarize the simulated detection count rate induced by the X-ray/γ-ray transient sources and the expected SNR. For GRBs four different exposure times Δt were used: 64, 256 and 1024 ms for sGRBs and 4096 ms for lGRBs. It should be noted that long triggering timescales of the order of several seconds or tens of seconds are readily affected by the time variation of background due to geomagnetic latitude (cutoff rigidity) change during the orbit and the activation background varying with time since SAA passages. The SNR calculated for such long integration time is effected by the background systematics. Varying background can cause false triggers and detectors with larger effective area are more vulnerable unless a sophisticated background modeling is part of the trigger algorithm.

Different missions has employed different triggering timescales. *BeppoSAX*/GRBM used adjustable timescale in the range from 7.8125 ms to 4 s in 10 steps [204]. *CGRO*/BATSE used time windows of 64 ms, 256 ms and 1024 ms [205]. *Suzaku*/WAM used triggering timescales of 1/4 s and 1 s

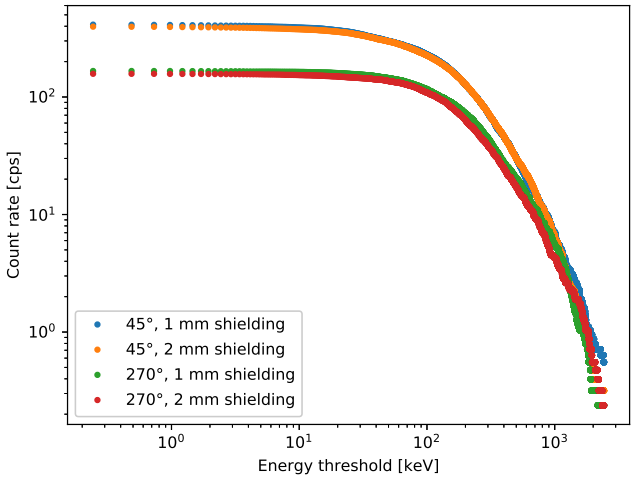

Figure 65: Count rate for a typical sGRB (for 1024 ms peak spectrum) versus detection low-energy threshold. Two source directions and thicknesses of the detector support structure are shown from the 70 investigated scenarios.[38]

[59]. *HETE-2*/WXM and FREGATE used timescales from 80 ms up to 10.5 s or longer, but they modeled background to remove trends which can cause false triggers [206]. *Swift*/BAT uses two types of rate triggers: i) "short" rate triggers with timescales 4, 8, 16, 32 and 64 ms which are traditional triggers employing single background period of fixed duration; ii) "long" rate triggers with timescales from 64 ms to 64 s which fit multiple background intervals to remove trends as pioneered by *HETE-II* [207]. *Fermi*/GBM uses triggering timescales of 16, 32, 64, 128, 256, 512, 1024, 2048, 4096 and 8192 ms [63]. In case of *AGILE*/MCAL, transients are searched using time windows of duration of sub-millisecond, 1, 16, 64 , 256, 1024 and 8192 ms [208, 209].

From Table 10 it is also seen that in contrary to one's expectation, TGF SNR increases with thicker detector casing. The reason for this is the hardness of TGF spectrum. The median energy of X-ray photons originating in TGFs is 2 MeV. These have a few per cent chance to interact with the scintillator material. The thicker detector casing provides more material in which these energetic photons can interact and produce secondary particles. Therefore thicker casing yields in higher SNR. This study is important in order to understand sensitivity of different trigger time window durations necessary for designing efficient GRB trigger algorithm.

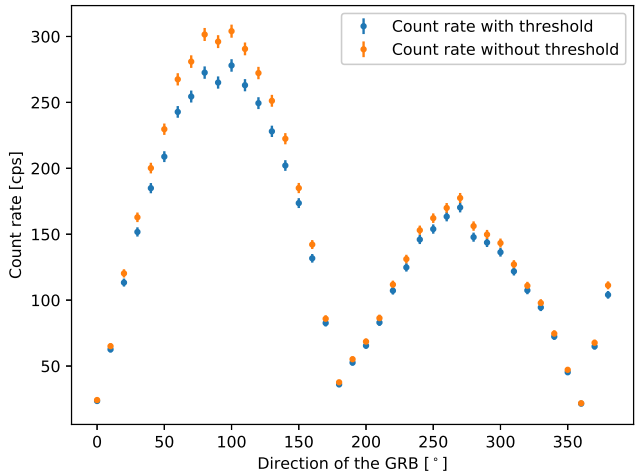

Figure 66: Count rate of a typical sGRB (for 1024 ms peak spectrum) for different source directions. The satellite was rotated around its minor axis. An arbitrary but possible low-energy threshold of 20 keV was utilized. The aluminium detector support structure was 2 mm thick in this case.[38]

Al	sGRB peak spectrum			lGRB peak spectrum			lGRB	TGF	SGR
[mm]	64 ms	256 ms	1024 ms	64 ms	256 ms	1024 ms	fln. sp.		
0.5	1440	910	385	1190	924	758	326	34600	16200
1.0	1390	911	367	1139	908	715	309	38900	14000
1.5	1300	890	367	1110	840	674	292	37600	11900
2.0	1320	839	355	1058	815	662	277	38600	10500

Table 9: Simulated detection rate induced by X-ray/γ-ray transient sources. The detection rate is in counts per second, assumes a low-energy threshold of 20 keV and is simulated for different thicknesses of the aluminium support structure of the detector. For short and long GRBs the 64 ms, 256 ms and 1024 ms peak spectra were used. For long GRB also the fluence spectrum (fln. sp.) was used.[38]

4.11 Discussion

The background count rates obtained in our MC simulations were derived from models of fluxes of gamma-rays and particles averaged over various latitudes, depending on the particular flux component, below 50° and outside SAA. The reason is that we aim to obtain an expected "mean" background

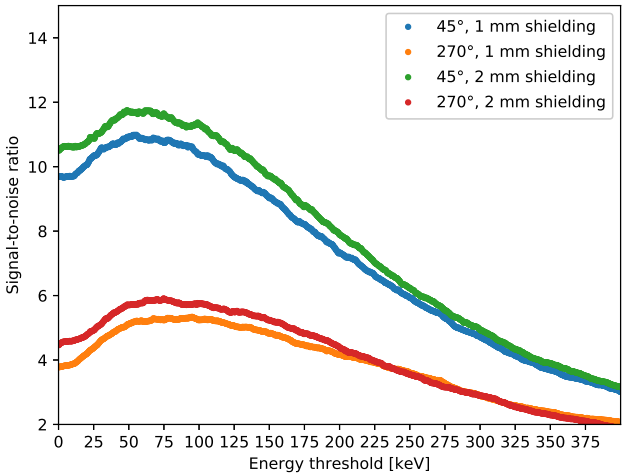

Figure 67: Signal-to-noise ratio of short GRBs versus low-energy detection threshold. Two detector support structure thicknesses and two GRB directions (rotating around Z axis) are shown among the directions investigated in Sec. 4.10.2. Among these investigated directions, highest signal is achieved when the direction of the GRB is 45°. For 270° the signal from a typical sGRB is the smallest (see Figure 63).[38]

rate in parts of orbit which are suitable for gamma-ray transient scientific data collection. However, in reality, the background rate will have time variation due to geomagnetic latitude (cutoff rigidity) change within the orbit and due to the activation background varying with time since SAA passages.

The foreseen orbital inclination of the *CAMELOT* satellites is above $\sim 50°$ and option of polar orbits is also likely. Therefore significant background variation is expected as well. We investigated background count rates measured by *Fermi*/GBM, *RHESSI*[210] and *Lomonosov*/BDRG[153] gamma-ray instruments throughout their orbits to learn what background variations are expected. In case of *Fermi*/GBM (altitude 560 km and inclination 26°) the background rate outside SAA for one NaI detector module in $8-1000$ keV range varied throughout the orbit between ~ 1000 cps and $\sim 1500-2000$ cps, i.e. $\sim 1.5-2\times$ change (about two months after the launch), see also Ref. Fitzpatrick2012. In case of the *RHESSI* spectrometer (altitude 500 km and inclination 38°) the background rate outside SAA for one rear detector segment in $25-20\,000$ keV range varied throughout the orbit between ~ 250 cps and ~ 650 cps, .i.e. $\sim 2.5\times$ change (about three

Al	sGRB peak spectrum			lGRB peak spectrum			lGRB fln. sp.	TGF	SGR
(mm)	64 ms	256 ms	1024 ms	64 ms	256 ms	1024 ms	4096 ms	0.1 ms	0.2 s
0.5	9.27	11.7	9.91	7.66	11.9	19.5	16.8	8.79	185
1.0	9.35	12.3	9.87	7.66	12.2	19.2	16.7	10.3	167
1.5	9.23	12.6	10.4	7.89	11.9	19.2	16.6	10.6	149
2.0	10.1	12.8	10.8	8.08	12.5	20.2	16.0	11.6	142

Table 10: Simulated detection signal-to-noise ratio for X-ray/γ-ray transient sources. The detection SNR has been calculated for different thicknesses of the aluminium support structure of the detector. The assumed background count rate is the sum of all components as described in Ref. 4.10.1. For the GRB peak spectra were used the exposure time $\Delta t = 64\,\mathrm{ms}$, 256 ms and 1024 ms. For the fluence spectrum (fln. sp.) of long GRB we used $\Delta t = 4096\,\mathrm{ms}$. For TGF we assume exposure time $\Delta t = 0.1\,\mathrm{ms}$ and for SGR $\Delta t = 0.2\,\mathrm{s}$. For this TGF spectrum the SNR is only a theoretical value following from the formula. For example, for 1 mm thicknesses of the Al detector casing the expected detected number of counts within 0.1 ms from is 3.9 cnt, whereas the expected number of background counts is below 1 cnt (only 0.14 cnt).[38]

years after the launch) [13]. For a detector on a polar orbit the background rate can increase dramatically more when passing the polar regions of trapped particles in the van Allen radiation belt. The *Lomonosov*/BDRG (altitude 550 km and inclination 98°) measurements show that the rate outside SAA, in $20 - 450\,\mathrm{keV}$ range increases $\sim 50\times$ inside the polar regions compared to the rates near equator (about 5 months after the launch), see also Ref. Svertilov2018. Therefore outside SAA and polar trapped particle regions the background count rate variation of at least $\sim 2\times$ the value near the equator for detectors on board the *CAMELOT* satellites are also foreseen. Inside the polar regions the rate increase can be much higher.

Since CubeSats which are not on equatorial orbit (currently most of them) are subject to high proton flux upon SAA passages, these protons have enough energy to activate the material of the satellite [127]. Short term activation is important as decaying isotopes can cause a strongly time-variable background for a few minutes after the end of SAA passes. Long term activation can increase the background significantly in a matter of months. [211] To quantify the effects of proton induced activation, we plan to conduct simulations in the near future. Emission lines of radioactive isotopes could also be used for energy calibration. As an example for our

[13] http://sprg.ssl.berkeley.edu/~tohban/browser/

scintillators ^{123}I will be created which emit γ-rays with an energy of 159 keV [212].

In order to discuss how our estimated background rates of *CAMELOT* detectors scale to the observations of *Fermi*/GBM, *AGILE*/MCAL and *Suzaku*/WAM we consider the surface area of the scintillators of these instruments and assume that these surface areas can be used as rough scaling factors. For CAMELOT (CsI): 15 cm $\times$ 7.5 cm $\times$ 4 scintillators giving the area of $\sim$ 450 cm^2. For *Fermi*/GBM (NaI): 3.14 $\times$ (12.7/2 cm)^2 giving the area of $\sim$ 127 cm^2 for one detector module (the effective area around 0.4 MeV is $\sim$ 30 cm^2) [213]. For *AGILE*/MCAL (CsI): 1.5 cm $\times$ 37.5 cm $\times$ 30 detectors giving the area of $\sim$ 1700 cm^2 (the effective area at $0.4 - 1$ MeV is $\sim 200 - 300$ cm^2) [85]. For *Suzaku*/WAM (BGO) the area is $\sim$ 800 cm^2 [59].

The estimated background rates of *CAMELOT* detectors for 0.5 mm Al support structure are $\sim$ 2.3, $\sim$ 0.75 and $\sim$ 0.3 kHz respectively for $E >$ 10 keV, $E >$ 50 keV and $E >$ 400 keV (see Fig. 61). The observed background rates of one detector module of *Fermi*/GBM ($\sim$ 2 months after the launch, altitude $h = 560$ km and inclination $i = 26°$) are $\sim$ 1 kHz and $\sim$ 0.13 kHz for $E >$ 10 keV and $E >$ 400 keV, respectively. For *AGILE*/MCAL ($h = 550$ km and $i = 2.5°$) the rate is $\sim$ 1.3 kHz for $E >$ 400 keV. In case of *Suzaku*/WAM ($h = 570$ km and $i = 31°$) the rate is $4 - 6$ kHz for $E >$ 50 keV.

If we use the surface area of scintillators as a scaling factor than the background rate scaling between *Fermi*/GBM and *Suzaku*/WAM or *Fermi*/GBM and *AGILE*/MCAL is in a good approximation. The current simulated *CAMELOT* background is smaller than that of *Fermi*/GBM and *Suzaku*/WAM observations. For example, if we scale the *CAMELOT* background to the *Fermi*/GBM, it would be $\sim$ 0.65 kHz, which is lower than the observed value of $\sim$ 1 kHz for $E >$ 10 keV. This is of course due to the activation background component, which is not included in the *CAMELOT* simulated background and the scaling would be reasonable if we consider the activation background component for *CAMELOT* around $1 - 2$ kHz. The same applies when we scale *CAMELOT* background to *Suzaku*/WAM observations. Scaling *CAMELOT* background to *AGILE*/MCAL is in a good agreement even without accounting for the activation component for *CAMELOT*. The *AGILE*/MCAL satellite is in an equatorial orbit with an inclination of only 2.5° with low particle background which causes material activation.

Having the simulation results of the detection background count rate and GRB count rate we can discuss an approximate number of expected short and long GRB detections per year by a single *CAMELOT* satellite. For 1 mm Al casing and the best gamma-ray incident angle (45° to the surface normals of perpendicular detectors) the simulation detection count

rate is 911 cps and 715 cps for sGRB 256 ms and lGRB 1024 ms median peak spectrum, respectively. GRBs will not always be seen under this most preferred direction therefore we scale this rate by a factor of $1/\sqrt{2}$ which corresponds to the rate expected from GRBs seen perpendicular to the largest scintillator side (644 cps for sGRB and and 506 cps for lGRB). There will be GRBs seen under more preferred direction as well as under less preferred direction therefore this is a compromise direction. Furthermore we can assume a detection SNR threshold to be 5 and a mean background count rate to be 3 000 cps (1 500 cps from external background flux and 1 500 cps from material activation).

Therefore for the above-mentioned integration times we obtain detection count rate thresholds of 541 cps and 271 cps, respectively for sGRBs and lGRBs with median spectral shapes. By scaling the spectral normalizations A_{256} and A_{1024} of typical *Fermi*/GBM sGRB and lGRB from Table 3 by factors of 541/644 for sGRB and by 271/506 for lGRB and by integrating those amplitude-scaled typical spectra one obtains the threshold photon peak fluxes of $4.03\,\mathrm{ph\,cm^{-2}s^{-1}}$ for sGRB (or fluence of $3.92 \times 10^{-7}\,\mathrm{erg\,cm^{-2}}$ for 256 ms) and $2.22\,\mathrm{ph\,cm^{-2}s^{-1}}$ for lGRB (or fluence of $3.48 \times 10^{-7}\,\mathrm{erg\,cm^{-2}}$ for 1024 ms). These thresholds together with the expected duty cycle can be used to estimate an approximate number of GRB detections per year from the distribution of GRB photon peak fluxes from the FERMIGBRST catalog.

Fermi/GBM surveys the entire sky, that is not occulted by the Earth, with the observing duty cycle of $\sim$ 85 % [214]. Following the trapped particle maps the duty cycle would be 76 % for orbital inclination of 89° (polar orbit is an option for *CAMELOT* CubeSats) and integral particle flux $\leq$ $10\,\mathrm{particle\,cm^{-2}s^{-1}}$ (see Sec. 4.5.1 and Ref. Ripa2020). However, we examined background data measured by a GRB instrument *Lomonosov*/BDRG at polar LEO and it suggests that due to high background variation the duty cycle can be expected to be lower, i.e. about 60 %. Therefore we assume this more conservative value of $\sim$ 60 % as a duty cycle for a single *CAMELOT* CubeSat. From these calculations we obtain an approximate number of sGRBs detectable by a single *CAMELOT* CubeSat, i.e. with photon peak flux higher than the aforementioned thresholds, to be 18/year. In case of lGRBs we obtained 115/year.

In the same way we proceeded with SGRs. By using the simulated detection count rate of a typical SGR for the aluminium detector casing thickness of 1 mm from Table 9 and the typical SGR spectral parameters calculated in Sec. 4.2.2 we obtained SGR detection threshold photon flux of $9.19\,\mathrm{ph\,cm^{-2}s^{-1}}$ or threshold fluence of $8.47 \times 10^{-8}\,\mathrm{erg\,cm^{-2}}$ for 0.2 s and energy range of $15 - 500\,\mathrm{keV}$. This means that all bursts listed in the Konus catalog of SGRs between 1978 and 2000 [75] would be detectable also by a

CAMELOT CubeSat.

A difficulty is to estimate the SGR annual detection rate using this catalog because it was composed of measurements from several interplanetary spacecrafts and one LEO satellite which means it is difficult to know the exact duty cycle for the SGR measurements. Therefore we examined the five year *Fermi*/GBM SGR catalog [215] and calculated the detection thresholds also for the time scale of 0.1 ms and energy range of $8 - 200$ keV which are the median SGR duration and energy range used in this catalog. For these conditions we obtained *CAMELOT* SGR photon flux detection threshold of $18.2\,\mathrm{ph\,cm^{-2}s^{-1}}$ or fluence threshold of $5.82 \times 10^{-8}\,\mathrm{erg\,cm^{-2}}$. Using this fluence threshold, the SGR fluence distribution reported in the *Fermi*/GBM SGR catalog and the aforementioned assumed duty cycle of a single *CAMELOT* CubeSat we obtained a prediction of 46 SGRs detectable by one *CAMELOT* satellite annually. Note that the annual number of detected SGRs will be subject to large fluctuations since SGR bursts tend to occur in clusters when particular magnetars become active.

Concerning the used SNR calculation it should be noted that it is rather simplistic for TGF detection. The large number of 0.1 ms intervals (large number of trials) during the mission examined by the trigger algorithm (note that the rate trigger algorithm for *CAMELOT* is yet under development) as well as the fact that a cosmic ray could easily cause a count in two detectors needs to be taken into account. If other background sources by chance produce one or two additional counts in the same 0.1 ms interval, then a false trigger would be issued.

Specific conditions of the trigger algorithm to efficiently detect TGFs by *CAMELOT* CubeSats are yet to be determined. For example one option is to aim to detect brighter but less frequent TGFs. *AGILE*/MCAL observes 2780 TGFs within 3.5 years which is $\sim$ 800 TGFs/year [86]. The fluence distribution follows a power low of -2.2 [88]. This means that TGFs with 5 times greater fluence will be 3 % in number. The spectrum of a typical TGF used in our simulations is based on the TGF fluence at the threshold level of *AGILE*/MCAL. Therefore if a *CAMELOT* satellite had equatorial orbit as *AGILE* then this scaling would give 23 TGFs/year/CubeSat with 19.5 cnts/TGF.

However, *CAMELOT* satellites will likely have polar or other high-inclination orbits. From observations most, if not all, TGFs has been detected at latitude lower than 45° north and south by *CGRO*/BATSE, *RHESSI*, *AGILE*/MCAL, *Fermi*/GBM and ASIM instruments [216]. One of the good distribution maps [216] was obtained from the recent ASIM instrument [217]. As relatively young (operational for $\sim$ 2 years yet), the TGF number is not high, but with 51.6° on *ISS*, it has a relatively uniform

coverage of the TGF positional distribution. There are three major TGF sites: around Central America, around Central Africa and around South East Asia. A good comparison of the expected TGF detections by *CAMELOT* can be done with the *TARANIS*/XGRE instrument which was supposed to operate on Sun-synchronous orbit with 700 km altitude. According to Ref. Sarria2017 *TARANIS* (unfortunately lost due to the VEGA launch failure) was expected to detect $\sim$ 200 TGFs/year. A *CAMELOT* satellite will have about 1/10 of the effective area, but if corrected for the 500 km vs. 700 km altitude difference, this would be converted into $\sim$ 1/5. Then $200 \times 3\,\%$ (for $5\times$ brighter TGFs) give $\sim$ 6 TGFs/year for a single satellite. With 9 satellites in a constellation CAMELOT would provide $\sim$ 50 TGFs/year.

As shown in Fig. 63, the *CAMELOT* detectors can observe gamma-ray sources also for directions when the photons need to pass through the body of the satellite (rear direction). This means that also gamma-ray photons scattered off the Earth's atmosphere and entering the detector from the side not facing the source can produce signals. In this sense the *CAMELOT* satellites will have omnidirectional FOV although the sensitivity for the rear direction is lower. Compton scatter of the burst flux off the Earth's atmosphere into the detector is a known effect and observed already by the *CGRO*/BATSE instrument [218]. Correction for this effect has been included in the BATSE's response matrices [219] and in the trigger efficiency calculation [220]. See also Refs. Wigger2008, Wigger2006 with spectrum of GRB 021206 measured by the RHESSI satellite which shows significant Earth's atmospheric backscatter of photons below 300 keV. Moreover, a method which employs the atmospheric scattering of GRB flux for the polarisation measurements in the prompt gamma-ray emission has been published in Ref. Willis2005 and Ref. McConnell1996. The atmospheric scattering might affect the *CAMELOT* measurements and it might be necessary to do careful modeling of this effect in the future in order to reduce the systematic uncertainties. A detailed simulation of this effect is beyond the scope of this section, however such an analysis might be useful to improve the timing based localization in LEO.

4.12 Conclusions

A Geant4 based simulation was developed to understand the capabilities of the planned *CAMELOT* CubeSat constellation to detect short and long GRBs, TGFs. The CAD model of the satellite was imported directly to Geant4 with CADMesh. Since the scintillators onboard *CAMELOT* have a considerably large size, optical light propagation is important. To take this into account, scintillation light propagation was simulated in Geant4 by tracking each optical photon created by scintillation.

The simulation was validated and its optical parameters were calibrated with an ^{241}Am X-ray source. The calibrated reflectivity of the surface of the scintillator turned out to be 99.99 % and absorption length 60 cm.

Thirteen background components were simulated to determine their contribution to the overall background spectrum. The five components which contribute the most to background are: CXB (1000 cps), albedo X-rays (200 cps), cosmic-ray α particles (49 cps), albedo protons (44 cps) and albedo positrons (27 cps). These count rates were calculated by assuming a 20 keV low-energy threshold and 1 mm of aluminium detector support structure thickness.

The total simulated background rate was 1545 cps for a detector casing thickness of 0.5 mm. By increasing the casing thickness to 1 mm the total background decreased to 1410 cps and by increasing it more to 1.5 mm it turned out to be 1270 cps. Finally for 2 mm it was 1100 cps. These rates were obtained from models of fluxes of gamma-rays and particles averaged over various latitudes, depending on the particular flux component, below 50° and outside SAA, because our goal was to obtain an expected "mean" background rate in parts of orbit which are suitable for gamma-ray transient scientific data collection.

Since the four scintillators of the *CAMELOT* CubeSat are placed on its two sides the direction of the source influences the signal-to-noise ratio. A typical short GRB was simulated in 70 directions. 35 directions were investigated by rotating the satellite around its major axis by 10° between simulations. The SNR of the detection of the typical short GRB (with integral fluxes between 8.15 ph cm^{-2}s^{-1} and 2.21 ph cm^{-2}s^{-1} for $E > 5$ keV and for 64 and 1024 ms integration window respectively) varied between 5 and $\sim$ 10. Other 35 directions were simulated by rotating the satellite around its minor axis. This resulted in less favorable directions, since the cross section with respect to the direction of X-rays from the sGRB is much smaller in this case. An SNR of at least 5 was determined for the range from 50° to 150°.

The simulations show that CubeSats equipped with large area scintillators

are able to detect sGRBs, lGRBs, TGFs and SGRs. In our case for the *CAMELOT* CubeSats an average sGRB (256 ms peak spectrum) could be detected with an SNR of > 12 in the most favoured direction. lGRBs (with an integral flux of $2.54\,\mathrm{ph\,cm^{-2}s^{-1}}$ for $E > 5\,\mathrm{keV}$) yield an SNR of > 16 for 4096 ms exposure. TGFs despite their very short duration of 0.1 ms could also be detected because, for example, for 1 mm thicknesses of the Al detector casing the expected detected number of counts within 0.1 ms from a TGF (with fluence at the threshold level of *AGILE*/MCAL) is 3.9 cnt, whereas the expected number of background counts is only 0.14 cnt. SGRs due to their very large X-ray flux yield in an SNR of >100. The results of the simulation will aid the development of the trigger algorithm and also choosing the detector support structure.

5 Activation of satellites in space

5.1 Introduction

A software toolkit for the simulation of activation background for high energy detectors onboard satellites [221] is presented on behalf of the HERMES-SP [222] collaboration. The framework employs direct Monte Carlo and analytical calculations allowing computations two orders of magnitude faster and more precise than a direct Monte Carlo simulation. The framework was developed in a way that the model of the satellite can be replaced easily. Therefore the framework can be used for different satellite missions. As an example, the proton induced activation background of the HERMES CubeSat is quantified.

The High Energy Rapid Modular Ensemble of Satellites (HERMES) mission [222] consists of a fleet of 3U CubeSats hosting broadband X and gamma-ray detectors. The aim of the mission is to detect transient sources with high sky coverage and good angular resolution. The CubeSats will utilize triangulation to locate the investigated X-ray sources and will be launched over a longer time span. Therefore proton induced activation of these satellites have to be taken into account since it increases background in the long term significantly. An important factor to evaluate for the HERMES mission is the activation background produced by the satellite passages inside the regions with high fluxes of trapped protons, such as the South Atlantic Anomaly (SAA). Different orbits will have different characteristics (depth and duration) and therefore different irradiation doses. Moreover, decay times of all the radio-activated isotopes shall be evaluated. We have developed a framework similar to Odaka et al. [223] which is much more efficient from a computational point of view with respect to a full-scale Monte Carlo simulation. This method consists of three steps.

1. A simulation to determine the production rate of each long lived unstable nuclear isotope.

2. Analytical calculation of the decay rates and chains of each isotope at any given time.

3. A second simulation involving only the decaying isotopes and their products.

5.2 Determining the number of primary nuclear isotopes

The framework which is presented in this paper is based on Geant4 [36]. In the first step a mass model is used to simulate an irradiation of the satellite with monochromatic proton fluxes. One can think of this step as the determination of response to the proton irradiation similarly to the Green function technique. 16 energies between 4 MeV and 700 MeV were simulated. Energies lower than 4 MeV does not create activation in our case and energies above 700 MeV have typically very low fluxes. In Figure 68. the number of different identified isotopes is shown, for a simulation with the HERMES mass model and in Figure 69 the simulation is shown. Higher proton energy results in more possible reactions.

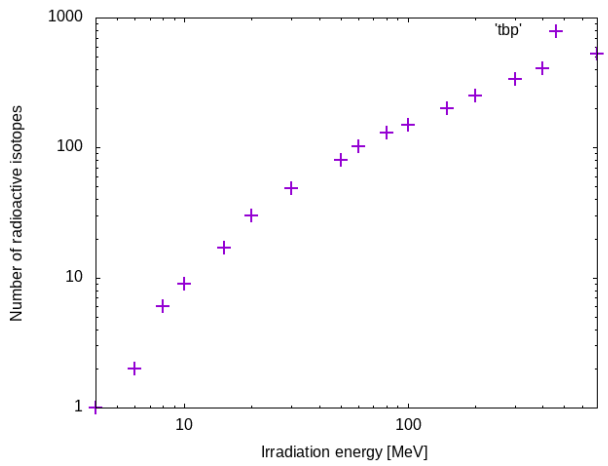

Figure 68: Number of identified species of isotopes created by proton irradiation on the HERMES satellite for each irradiation energy. Different volumes implemented in the mass model are treated independently, but for this plot they are summed together.[221]

In the "SteppingAction" Geant4 class radioactive decays are detected. Then to prevent recording a decay chain several times, the decayed isotope and the simulation of its secondary particles is stopped. For each volume of the geometry the name, energy, and excitation level of these isotopes are stored with their excitation energy.

Each of the "Physical" volumes in the mass model have to be treated independently. The reason for this is due to two factors. Each volume consists of different materials, therefore different radioactive isotopes will be created. The other reason is that the chance that a decaying isotope inside different

volumes will be actually detected can be very different: e.g., an isotope decaying in the detector will certainly be detected, but one in the solar panels is very unlikely to be recorded.

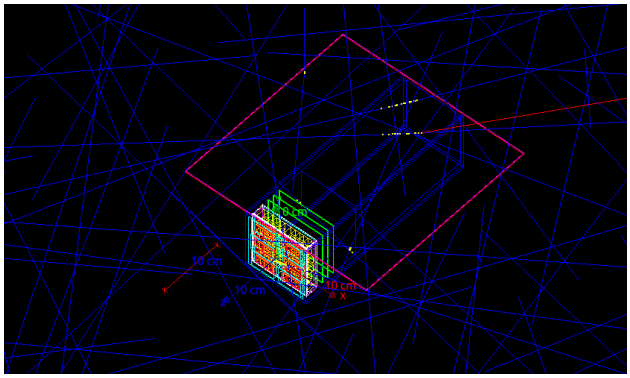

Figure 69: The mass model of the HERMES satellite being irradiated by protons.[221]

Different energy irradiations yield in the creation of very different isotopes as nuclear cross sections vary significantly by energy. Also, the abundance of the created nuclear isotopes is very different. For example, simulating a proton fluence of 100 000 cm^{-2} with energy of 30 MeV yields mostly to the production of Tb155 and Ge68. For this fluence, about 5000 isotopes of each type are created. For an irradiation at 700 MeV, on the other hand, the most abundant produced isotope is O15, with a number of 170 000 generated nuclei. The second most abundant isotope in this case is Ga68 with 82 000 nuclei. Also, at 700 MeV the number of different created isotopes is 20 times higher than at 30 MeV.

5.3 Calculation of activity for time of interest

The input spectrum used was determined by the AP9 model of SPENVIS Monte Carlo mode with 90% confidence level for an orbit with height of 600 km and inclination of 40°. It should be emphasized that this represents, both for the orbit type and for the radiation model used, an *absolute worst* case for the HERMES scenario. In this case, most of the protons reach the satellite when it is passing through the SAA. In order to obtain a mean SAA flux, the proton spectrum was averaged simulating an orbit through 30 days sampled at a step of 10 s. Then the fluence of the protons inside one single pass through SAA was determined by multiplying the average spectrum by the transit duration 60×90 s. (There is one SAA passing each 90 minutes. Therefore the fluence in a single passing corresponds to 60×90 s of the average

spectrum assuming that the proton fluence is zero outside of SAA.) In this case, an integral proton fluence of 2.5×10^6 protons/cm^2 at energies above 4 MeV was reached.

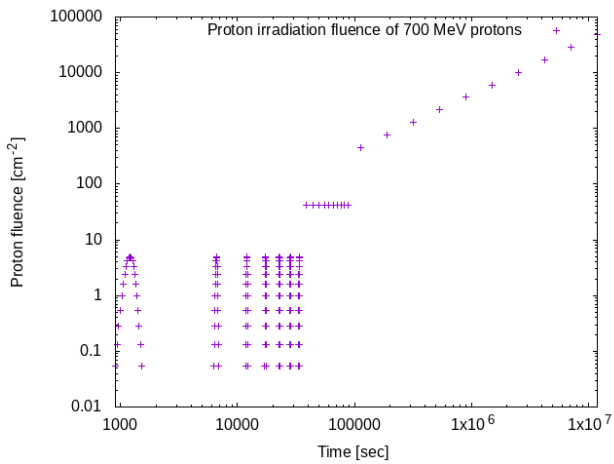

Figure 70: Irradiation profile used to calculate activity for 700 MeV protons.[221]

The contribution of each SAA passage is different since the created radioactive isotopes have different time elapsed to decaying. Also each isotope has a different decay time, therefore the contribution of each SAA will vary by time. We can solve the Bateman eq. [224] for each 1 second timestep inside each SAA transit. Therefore we choose to group the decaying times into "time slices". The seven SAA passages closest to the time of interest were sampled in 21 points. The following 9 SAA transits were treated as a single irradiation. The rest of the passages were grouped into 10 irradiation with a logarithmical integration window. In Figure. 70 the described irradiation profile can be seen.

The first seven SAA transits were simulated with a Gaussian time profile sampled in 21 points. The standard deviation of the Gaussian was chosen to be 100 seconds. In order to keep computation time reasonable but still keep precision the 9 passes were assumed to be single irradiation. The rest of the passes were divided into 9 irradiations in time. As the decays have a logarithmic nature, these 9 irradiations were grouped logarithmically in time as can be seen in figure 69.

The X-axis of Figure 70. shows time between the time of interest and the given irradiation. For each of these points the decays chains are calculated and then summed up to yield the total number of isotopes. The explicit formula to determine the amount of the Nth isotope in a decay chain after

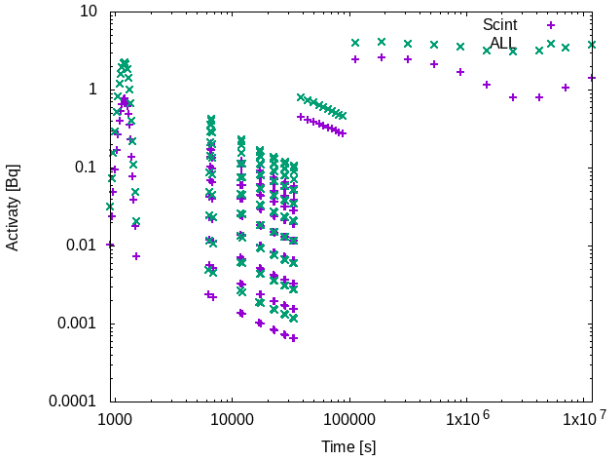

Figure 71: The activation for each irradiation timeslice from 100 MeV protons for all of the volumes and for only the scintillator. Roughly half of the total satellite activation is due the scintillator.[221]

and elapsed time t time is:

$$N_n(t) = \sum_{i=1}^{n} \left[N_i(0) \mathrm{x} \left(\prod_{j=i}^{n-1} \lambda_j \right) \mathrm{x} \left(\sum_{j=i}^{n} \left(\frac{e^{-\lambda_j t}}{\prod_{p=i,p\neq j} n(\lambda_p - \lambda_j}} \right) \right) \right] \tag{27}$$

The algorithm identifies the decaying isotopes created by the proton-induced activation in the first simulation. Most of them are in ground state. Afterwards the algorithm identifies the decay chains and the decay rates of the corresponding daughter nuclei before the deletion of very short lived particles.

The first step in this algorithm is the construction of the decay chains, which describe the decay of the isotopes identified in the first simulation. This is implemented in C++, employing the built-in function of Geant4 to access the decay products of the element in question. The decay tables are taken from the ESNDF dataset included in the Geant4 distribution. Excited states and floating levels (same excitation energy but different angular momentum) of the nuclei are treated individually. (An example for the importance of this: for Ta178, half life can be an order of magnitude different in case of different floating levels of the nuclei.) The decay chains were created by identifying the decay modes of the original isotopes and deducing what the daughter isotope(s) can be. The implemented algorithm looks recursively for the unstable daughters of the isotope in question. This was repeated until the last element had no unstable daughters. In order to keep the number of

decay chains reasonable, daughter isotopes with branching ratios lower than a given threshold are neglected.

An example of such a decay chain is:

Hf156 →Yb152 →Tm152[482.320] →Tm152 →Er152[1715.400] →Er152 →Ho152[179.400] →Ho152
→Dy152[3500.000] →Dy152 →Tb152[256.930] →Tb152 →Gd152[2880.670] →Gd152 →Sm148 →Nd144.

In the brackets is shown the excitation energy in keV. The number of decay chains increases by input proton energy, all together there are more than 1.5 million chains. The Bateman equation [224] has to be solved for each of these chains for every time in the irradiation profile. Moreover, the decay chains are treated independently in each volume. Still on a standard PC (Intel Core i7-8700K CPU @ 3.70GHz × 12, 32 GB of RAM) the algorithm runs in a few hours by setting a lower threshold for the cutoff of branching ratios to 5%.

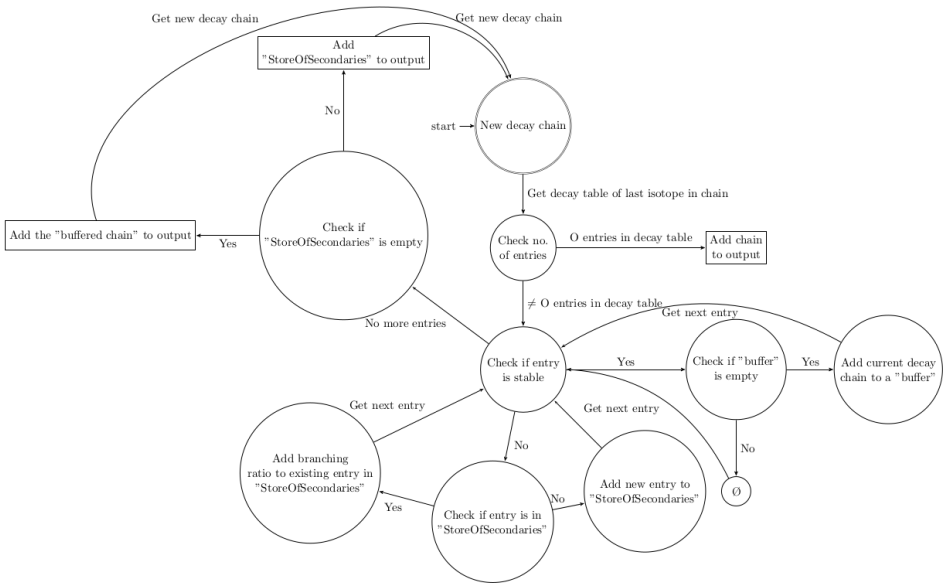

Figure 72: The statediagram chart of the decay chain construction from the decay scheme of the mother nuclei.[221]

The second part of the algorithm is the exclusion of isotopes (mostly isomers) with very short half life from the decay chains. This is needed since to obtain the amount of each isotope after a given time, one needs to solve

the Bateman equation. In this equation, for very large decay rates (λ) even the double-precision floating-point format is not sufficient. Therefore the isotopes with a decay rate larger than 10^9 are erased from the decay chains: this corresponds to a half life of 21 ms. This includes only very short lived isomers (like Ta181[6.237] or W181[365.550]) which would not be abundant after the time in question passes. Therefore it does not affect the results of the simulation.

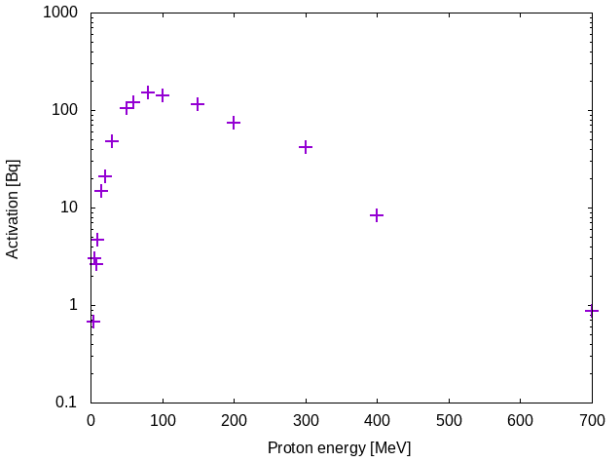

Figure 73: The contribution of different energy bands of primary protons to the activation of the satellite.[221]

The third part of this step is to solve the Bateman equation for these decay chains. The solution of the Bateman equation does not have a closed form, although it was possible to implement the solution recursively in C++. In order to be able to solve the equation, the decay chains were created in linear fashion. In order to obtain the activity of each radioactive isotope, their amount needs to be determined. The software determines this normalization factor from the provided integral photon flux.

As can be seen in Figure 73 about half of the activation due to 100 MeV protons is created in the Gadolinium Aluminium Gallium Garnet (GAGG) scintillator. For other energies this is different as different isotopes have different energy dependence on proton activation cross section. Also what can be seen is that the activity of the volumes changes by time as the isotopes in the scintillator decay "faster" than those on the other satellite structures. The proton energy that contributes most to the overall activity in the HERMES case is about 100 MeV, since protons around this energy have intermediate flux and also quite high activation cross-section compared to lower energies.

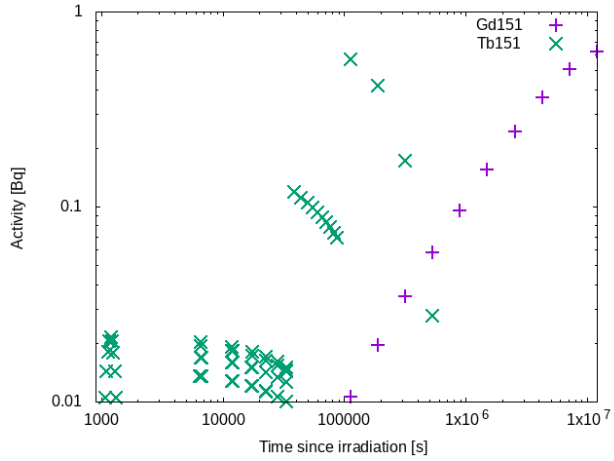

Figure 74: The activity of Tb151 and Gd151 in different time slices with respect to the time of interest. The former decays into the latter. For long timescales the latter is more important for shorter ones, the previous.[221]

For different timescales different isotopes dominate the activity. For example let's take the decay chain:

Tb151 →Gd151[839.320] →Gd151 →Eu151 →Pm147 →Sm147

Tb151 decays with a half-life of 18 hours. After about a day Gd151 becomes more important than Tb151 as can be seen in Figure 74. For the simulated orbit, the activity of the whole satellite is 851 Bq after half a year in space assuming the discussed worst-case irradiation profile (AP9 90% c.l. model, 600 km altitude, inclination of 40°).

5.4 Simulation of detector response

The final result of the last algorithm is a list of isotopes sorted by activity in each volume of the mass model. In this simulation the most active isotopes are put in the respective volume where they were created and their decay is simulated. The energy deposited inside the Silicon Drift Detector (SDD) and the scintillator is registered. The histogram of the energy depositions are normalised to the isotope in question. In the end these histograms are merged into one single histogram which represents what we would actually measure in space due to activation (assuming a perfect energy resolution). Figure 75 shows the merged histogram obtained when assuming half a year spent in space.

The deposited energy inside the scintillator can be seen in figure 75. One can notice the $\beta+$ decay peak at 511 keV and also the characteristic electron

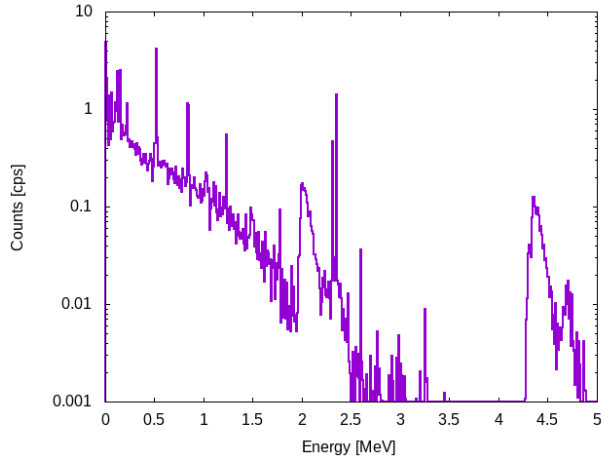

Figure 75: Energy spectrum deposited inside the GAGG scintillator by the proton induced nuclear decays after half a year in space.[221]

capture and γ peaks. Assuming a lower detector threshold of 20 keV the measured background would be 60 counts per second after spending half a year in space. It is interesting to compare this to the 800 Bq activity of the satellite. The deposited energy inside the SDD can be seen in figure 76. The number of detections originating in the SDD is negligible compared to the ones in the scintillator as the SDD is much thinner and consists of material with lower atomic number.

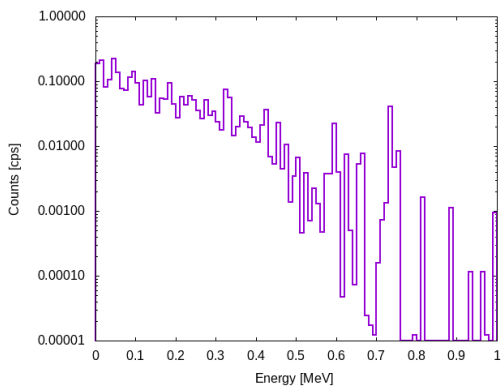

Figure 76: Deposited energy spectrum of the SDD by nuclear decays from activation.[221]

5.5 Validation of the framework

In order to ensure the validity of the results of the implemented simulation framework both direct Geant4 simulations and activation measurements from literature were used. In the direct simulations, Geant4 did all the calculations regarding the decaying nuclei. Energy depositions between 10692 minutes and 10908 minutes after the irradiation were recorded in this case to be compared to the results of our framework and in the experimental results of Sakano et al. [225]. A GAGG crystal with dimensions of $5.0 \times 5.0 \times 40\,\mathrm{mm}^3$ was irradiated by a proton beam with an energy of 150 MeV. A photomultiplier tube was used to read out the activation signal.

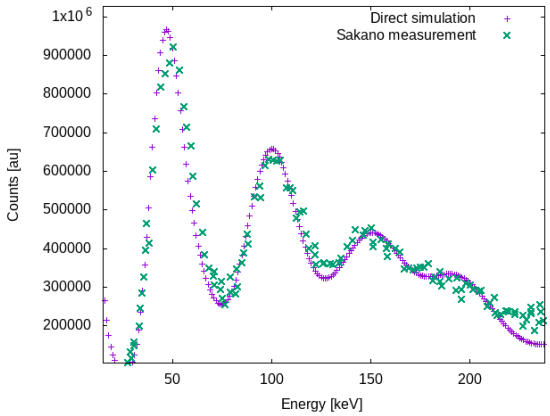

Figure 77: Deposited energy in a single GAGG crystal after 10800 minutes of irradiation by protons with an energy of 150 MeV. The direct simulation performed by us matches the experimental results of Sakano et al. [225].

To be able to run the direct simulations in a reasonable timeframe, only a single GAGG crystal was irradiated by 10^9 protons with an energy of 150 MeV. In Figure 77 the energy spectrum obtained in direct Geant4 simulations due to proton induced activation is compared to measurements obtained by Sakano et al. The results of the simulation were convolved by a Gaussian function with changing width to include the statistical process of photon detection in the measurements. Since the used measurements only span the low energy regime (up to 200 keV) we decided to validate our framework with direct Geant4 simulations. In figure 77 the energy spectrum obtained by the custom simulation is compared to the direct simulation.

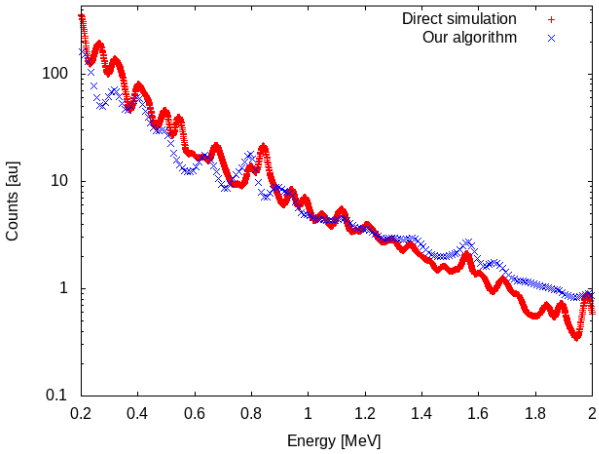

Figure 78: Deposited energy in a single GAGG crystal after 10800 minutes of irradiation by protons with an energy of 150 MeV. The direct simulation performed by us matches the results of our custom framework that we developed.[221]

5.6 Conclusions

Within the HERMES collaboration a Geant4 based framework was developed to understand and quantify the effect of proton induced activation. The framework utilizes direct Monte Carlo and analytical calculations to be able to run two orders of magnitude faster and more accurate simulation, with respect to a direct Monte Carlo approach. The framework was developed in a way that the geometry of the satellite can be replaced easily. We have applied the framework to our satellite and determined the energy deposition spectrum in the HERMES scintillators and in the SDD detectors as well after half a year in space. Assuming a low energy threshold of 20 keV the background due to proton activation would be 60 cps which is within the required specifications [226].

6 Proton scattering induced residual background of the ATHENA X-ray telescope

X-ray telescopes opened up a new window into the high-energy universe. However, the last generation of these telescopes encountered an unexpected problem: their optics focused not only X-rays but low-energy (so called soft) protons as well. These protons are very hard to model and can not be distinguished from X-rays. For example, 40% of XMM-Newton observations is significantly contaminated by soft proton induced background flares. In order to minimize the background from such low-energy protons the Advanced Telescope for High ENergy Astrophysics (ATHENA) satellite introduced a novel concept, the so called Charged Particle Diverter (CPD). It is an array of magnets in a Hallbach design, which deflects protons below 76 keV before they would hit the Wide Field Imager (WFI) detector. In this work, we investigate the effect of scattering of the deflected protons with the CPD walls and the inner surfaces of the WFI detector assembly. Such scattered protons can lose energy, change direction and still hit the WFI. In order to adopt the most realistic instrument model, we imported the CAD model of both the CPD and the WFI focal plane assembly. Soft protons corresponding to ≈2.5 hours of exposure to the L1 solar wind are simulated in this work. The inhomogeneous magnetic field of the CPD is included in the simulation. We present a preliminary estimate of the WFI residual background induced by soft proton secondary scattering, in the case of the optical blocking filter present in the field of view. A first investigation of the volumes responsible for scattering the protons back into the field of view is reported.

6.1 Introduction

Observations in the X-ray spectral band are vital for our understanding of the high-energy Universe, such as supernova remnants, galaxies and clusters of galaxies. The Einstein Observatory (also named HEAO-2, flown in 1978–1981) was the first X-ray telescope that utilized the Wolter Type I grazing-incidence X-ray optics that most observatories use to focus X-rays. Two of the most famous and renowned telescopes are NASA's Chandra X-ray Observatory (1999-) and the European Space Agency's (ESA) X-ray Multi-Mirror Mission Newton (1999-). The previous one focused on having superior spatial resolution on a limited field of view by optimizing the angular resolution at the cost of mass and effective area. The optics of the

XMM-Newton on the other hand is based on electro-formed Nickel, replicated from precision mandrels. This maximized the effective area to be able to offer spectral information on far fainter objects. It was an unexpected development that low-energy protons (≤300 keV) can scatter on the optics and end up being detected.

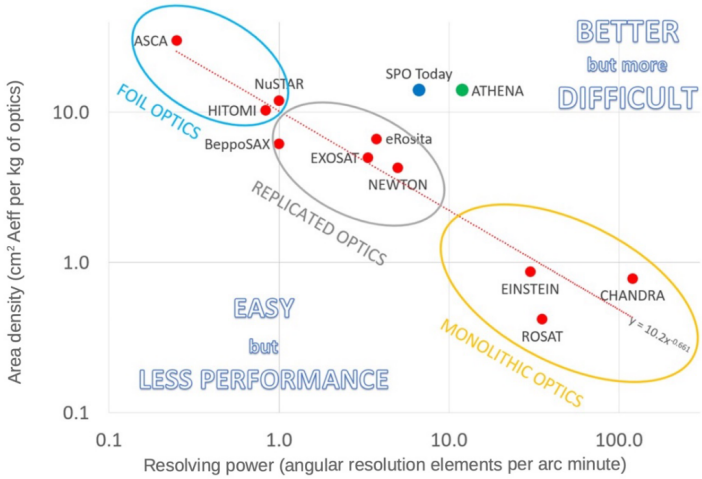

Figure 79: Classifying past and existing X-ray telescopes and the ATHENA telescope by area density of the optics and resolving power. ATHENA is an outlier, since it excels in both parameters. [232]

The next generation high-energy astrophysics observatories will look deeper into the high-energy Universe. Two metrics that are often used to classify X-ray telescopes are the area density and resolving power. The next large-class telescope of ESA will be the Advanced Telescope for High-ENergy Astrophysics (ATHENA). In Fig. 79 several of the past X-ray telescopes are compared to ATHENA with the mentioned two metrics. ATHENA will have an effective area of 1.4 m^2 at 1 keV with a focal length of 12 m. In order to obtain superior area density with fair resolving power ATHENA will utilize the so called Silicon Pore Optics (SPO) using a Wolter-I system. Interestingly, its design and production is based on the processes of the semiconductor industry. Since there have been tremendous efforts in producing electronics in the industry, this knowledge enables the production of an optical system that has excellent X-ray focusing capabilities [233].

The planned position of the ATHENA satellite is at the first Lagrange point as it is more favourable for the background [235, 236]. The two instruments of ATHENA are the Wide Field Imager (WFI) and X-ray

Integral Field Unit (X-IFU). This work focuses on the soft proton induced background of the WFI, sensitive in the 0.2 - 15 keV energy band. The origin of such low-energy ($\leq$300 keV) protons is an actively studied field. Their possible sources include interplanetary coronal mass ejections, acceleration events in Earth's magnetosphere and flaring near open coronal field lines [237]. These protons can scatter through the optical system of ATHENA and generate counts similar to the investigated X-rays in the detectors, resulting in contaminated measurements. Previous simulations predict the WFI soft proton induced background without magnetic shielding would be an order of magnitudes higher than the requirement [235].

The ESA and ATHENA team developed a novel concept to minimize the background induced by soft protons[238]. A Hallbach array of magnets is placed between the optical system and each of the detectors. The one in front of WFI is pear-shaped, has a diameter of 35 cm and its magnets weigh 21 kg. The requirement for the maximum residual background for the 2-7 keV band from soft protons is 5×10^{-4} cts/cm^2/keV/s, 10 % of the non-focused non X-ray background requirement[239].

The scientific assessment of this Charged Particle Diverter (CPD) is ongoing under the Background Topical Panel of the ATHENA Science Study Team [240], that includes the end-to-end simulation of the proton transmission efficiency from the SPO to the focal plane, using independent SRIM [241] and Geant4 simulations. Within this activity, we simulated in Geant4 the deflection of the WFI CPD and the potential secondary scattering of the deflected protons with the CPD walls, the WFI baffle and the other volumes composing the assembly. The final aim is estimating the residual background on the WFI, comparing it to the requirement and minimize, if needed, the secondary scattering in the WFI system.

Section 2.1 details the geometry applied in Geant4. Section 2.2 describes how the magnetic field of the CPD was treated in Geant4 and how the effect of the optics in front of WFI was taken into account. Section 3. describes the deposited energy spectrum on the WFI.

6.2 Simulating the proton scattering in GEANT4

A dedicated simulation was developed to understand if protons after being deflected by the CPD can scatter on the inner surfaces of the focal plane assembly and contribute to the background of the ATHENA WFI detector. The simulation was based on the Geant4 toolkit library [242, 244]. All simulations in this work were based on Geant4 version 10.5 with the patch 01 and use the single Coulomb scattering model as defined in the "G4EmStandardPhysicsSS" electromagnetic physics list [245]. The CAD

models utilized in the simulation were imported to Geant4 directly with CADMesh [201].

6.2.1 The geometry of the simulation

The inner part of the ATHENA telescope, which contains the WFI detector, has eight separate volumes. The incoming protons cross the CPD and its magnetic field first as can be seen in Fig. 80. Some of the protons hit the walls of the CPD. Protons then pass through (or scatter) on the baffle. Inside the cover volume there are five volumes. Three of them being CAD volumes, which can be seen in Fig. 81: the filter wheel, the holder of the detector and the base of the system. The remaining two volumes are the detector itself and the optical blocking filter which sits inside the filter wheel. By importing CAD models [241], we both saved time and made it possible to include small structures, such as the ridges on the surface of the baffle and the saw shape walls of the pear-shaped CPD. It is important to mention that these volumes are assumed flat on the micrometer scale, which is not the case in reality.

The WFI baffle has a coating of "Magic Black" material that consists of 44% Oxygen and 56% Aluminium by weight. The composition was measured by EDS X-Max 20 by Oxford Instruments installed in Scanning Electron Microscope TESCAN Mira on BUT CEITEC Nano (https://nano.ceitec.cz /scanning-electron-microscope-e-beam-writer-tescan-mira3raith-lis-mira/). CPD is coated with "Surtec 650" material (details in the Finitec document reference number: 1558830-914_00). The rest of the CAD volumes have the so called "AL7075" alloy, which contains Aluminium, 5.8% Zinc, 2.3%, Magnesium, and 1.3% Copper by weight. The Geant4 mass models of the WFI large area detector and the optical blocking filter are based on the work of Fioretti et al. (2018)[235].

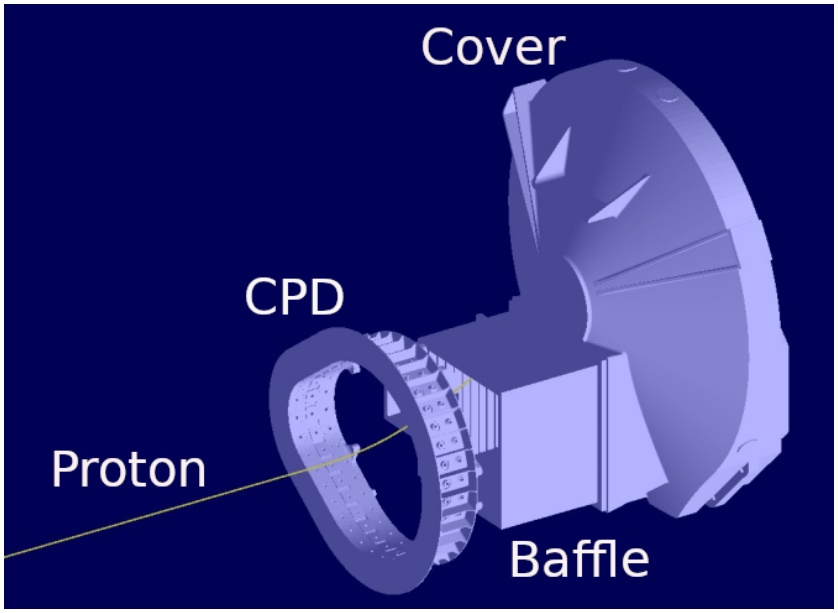

Figure 80: The model of the ATHENA WFI detector system and the Charged Particle Diverter imported in Geant4, kindly provided by the WFI team and ESA. A proton that is deflected by the magnetic field of the CPD is visible hitting the baffle volume. Three of the six included CAD volumes are visible.[246]

6.2.2 Input protons and magnetic field of the simulation

A dedicated raytracing simulation of the proton transmission through the ATHENA Silicon Pore Optics was performed under the CPD scientific assessment [240], using the Remizovich solution as scattering model [247] and assuming the L1 proton solar wind model as input population. The protons reaching the CPD were used as input for the present simulation. The list included 62.5 million protons, which corresponded to 2.4 hours of time in orbit. All of these were simulated one by one.

The magnetic field of the CPD was calculated with the Finite Element Method and was read into our particle simulation. In Geant4 one can customize the parameters of the trajectory equation solver. In our case, we chose the fourth order Runge–Kutta solver with six numbers of variables. The minimal step in the field was chosen to be 0.1 mm. The miss distance, which describes how curved the paths of charged particles are approximated – by a set of linear chord segments – was chosen to be 1 μm. The "delta intersection" parameter defines the minimum accuracy for the distance of track with a

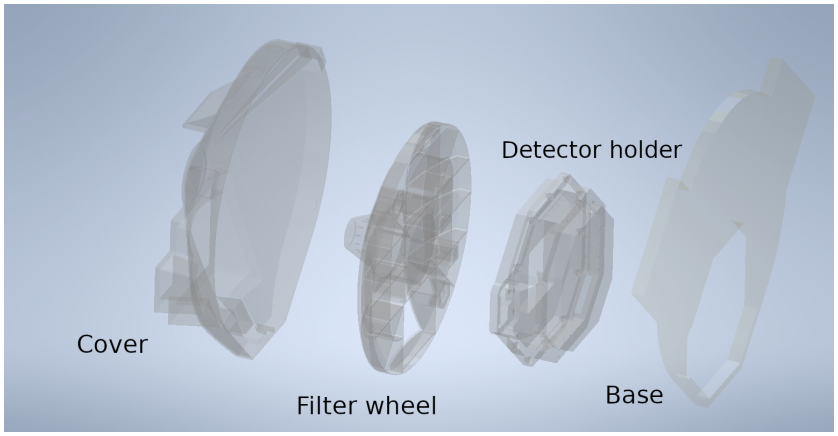

Figure 81: Exploded view of the CAD volumes under the "cover" volume. Protons arrive from the left side, through the hole in the cover. Then they traverse the filter wheel and its optical blocking filter. Finally, they arrive at the detector, which is situated inside the detector holder. [246]

volume boundary. It was set to 0.1 mm. "Delta onestep" is coupled to "delta intersection", it was set to be 1 μm. The relative error for the integration of the steps was also set. Its minimum value was chosen to be 10^{-5} and the maximum to 10^{-4}. Several other configurations were investigated but these settings proved to be the fastest and most accurate. Fig. 82 shows the magnetic field used in the present study. For every thousandth point in the grid the magnetic field vector is plotted. Since the CPD consists of a set of magnets in a pear-shape, the field is very inhomogeneous. The strongest field on the grid is 1.56 T (inside the magnet), while the weakest one is 136 μT (far from the CPD). Z direction is the longitudinal axis of the satellite.

The requirement for the magnetic field of the diverter was to deflect "direct" protons with energies below 76 keV before they reach the WFI detector. In our case, the magnetic field was sampled on a Cartesian grid with a step size of 7.5 mm and a volume of 0.125 m^3 surrounding the CPD in the simulation. The list of the magnetic field vectors included about 2.5 million points. This was read into the randomly accessible memory. A dedicated C++ package was developed to transform these points onto an other Cartesian grid with one unit cubes. This way the magnetic field for any given coordinate could be retrieved by its index speeding up the Geant4 simulation a thousand-fold. The paths of individual proton tracks were validated in our simulation with an independent COMSOL Multiphysics simulation.

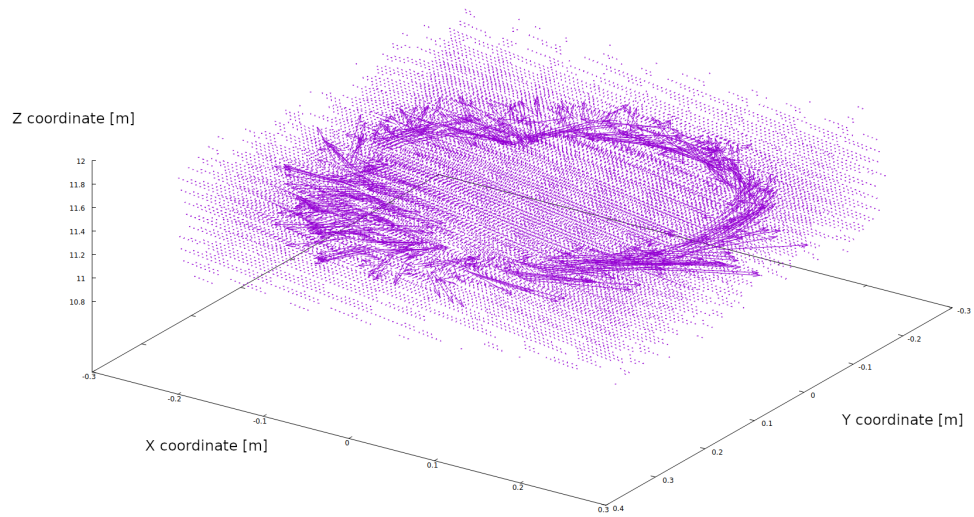

Figure 82: The magnetic vector field of the CPD used in the Geant4 simulation. The CPD consists of many smaller magnets in a pear-shaped configuration, producing the inhomogeneous field. [246]

6.3 The effect of roughness on the micrometers scale on scattering

In order to understand how the roughness on the micrometer scale would affect the scattering and hence the background a set of Geant4 simulations were performed. The surface of the most relevant part for proton scattering, the WFI was scanned with Scanning Probe Microscope and then imported into Geant4. This novel way of understanding the low energy proton scattering was validated with proton scattering measurements at specific incidence angles.

6.3.1 The surface model

The material that is planned to be used for the WFI baffle surface was scanned by an Scanning Probe Microscope at Brno CEITEC Nano[14]. This microscope produced a map of the surface with a 0.18 μm step size and an area of 92x92 μm^2. Since this material is an alloy we needed the exact composition for the Geant4 simulations. EDS X-Max 20 was used to measure the atomic composition. It was installed in a Scanning Electron Microscope (SNR) TESCAN Mira in BUT CEITEC Nano[15]. The material composition turned out to be 44% Oxygen and 56% Aluminum by weight, and had a density of 2.15 gcm^{-3}.

The surface maps were converted from ASCII to Standard Tessellation Language (STL) using Matlab. This file format describes the surface using triangles that are used to build a mesh. This STL file was loaded into Blender for STL file transformation. There a 300 μm thickness was assigned to the 2D map in order to represent a 3D object. The resulting STL file was read into Geant4 using the CADMesh package. In figure 83. the used model can be seen.

[14] https://www.ceitec.eu/scanning-probe-microscope-bruker-dimension-icon/e1359

[15] https://nano.ceitec.cz/scanning-electron-microscope-e-beam-writer-tescan-mira3raith-lis-mi

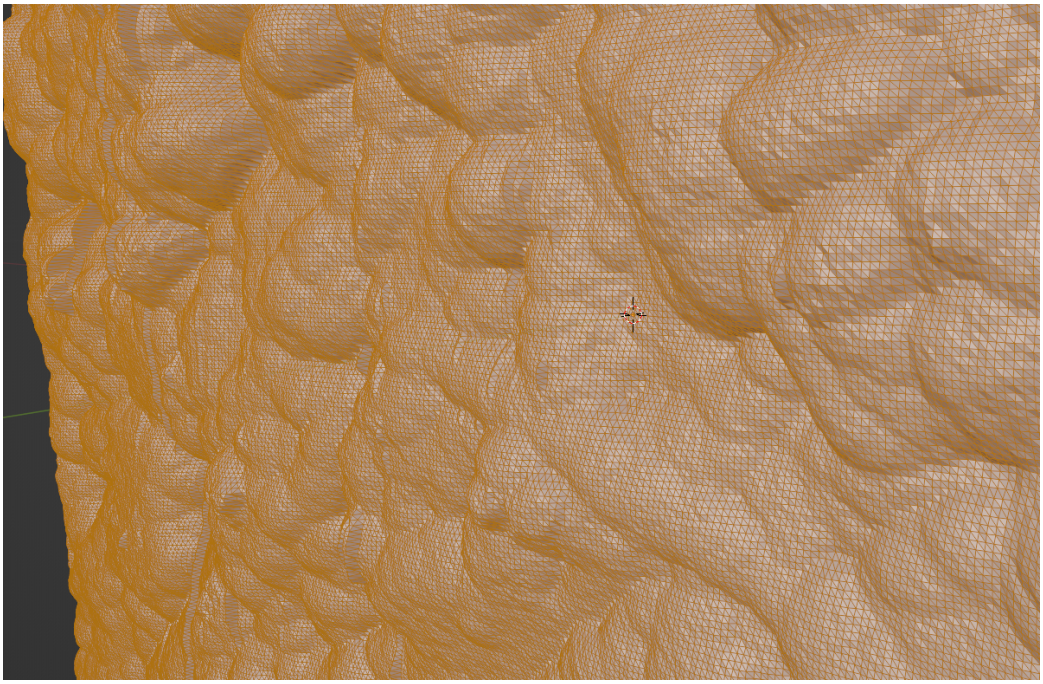

Figure 83: Highly detailed CAD model of the WFI baffle surface sample, where over a half million triangles represent the 92^2 μm^2 area. The samples were imported into Geant4 using the CADMesh library and measured atomic composition, and were created from measurements using Matlab and Blender. [248]

6.3.2 The validation of the simulation

In figure 84. the experimental setup that was used to measure the proton scattering at the Tandem laboratory of Uppsala University[16]. A proton beam with an initial energy of 100 keV was used. The scattered protons were recorded at three different positions. In the figure one of the detectors are shown. The size of these detectors are 10°x10°.

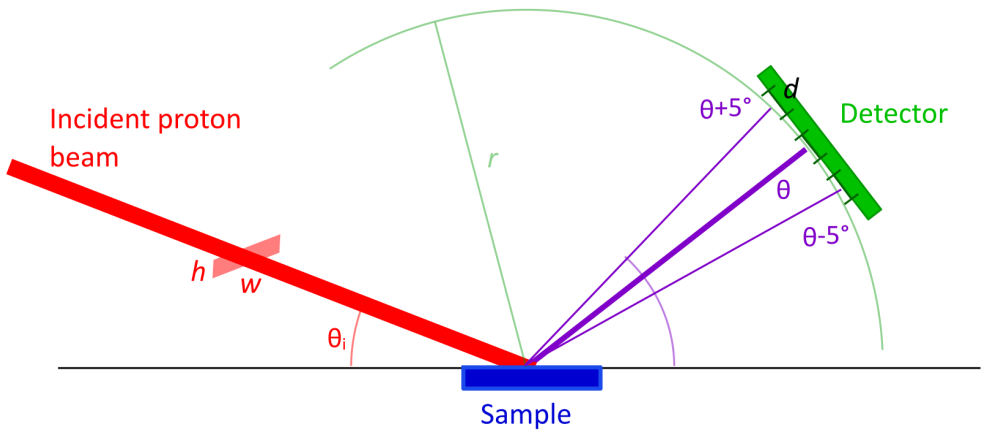

Figure 84: Schematic view of the experimental setup: a particle beam shoots 100 keV protons at incidence angles of 20°, with the energy and scattering angles (θ) of the deflected protons being measured by a detector at various positions, θ and $\theta \pm 5$. [248]

In Geant4 a hemisphere was defined around the target in order to register protons scattering back in all directions. The computational cost of the simulations were significant, almost 24 cores (two threads each) were running for three to simulate the sample. This was due to the fact that the CAD volume of the sample had $\approx$ 1 million triangles in it and a proton could scatter among the small irregularities on the surface. CUTVALUE... The same simulations were repeated with a flat surface in order to understand the contribution of the roughness on scattering.

Figure 85. compares measurements with the flat surface Geant4 simulation and the one where the roughness was included can be seen for the proton energy of 100 keV and incident angle of 20°. A SRIM simulation was also performed where some simplifications were made and only one scattering

[16] https://www.tandemlab.uu.se/?languageId=1

of the proton was allowed. It can be seen that only the simulation with the included roughness from SNR measurements reproduces the scattering efficiency. For this specific case the roughness doubles the efficiency of the scattering.

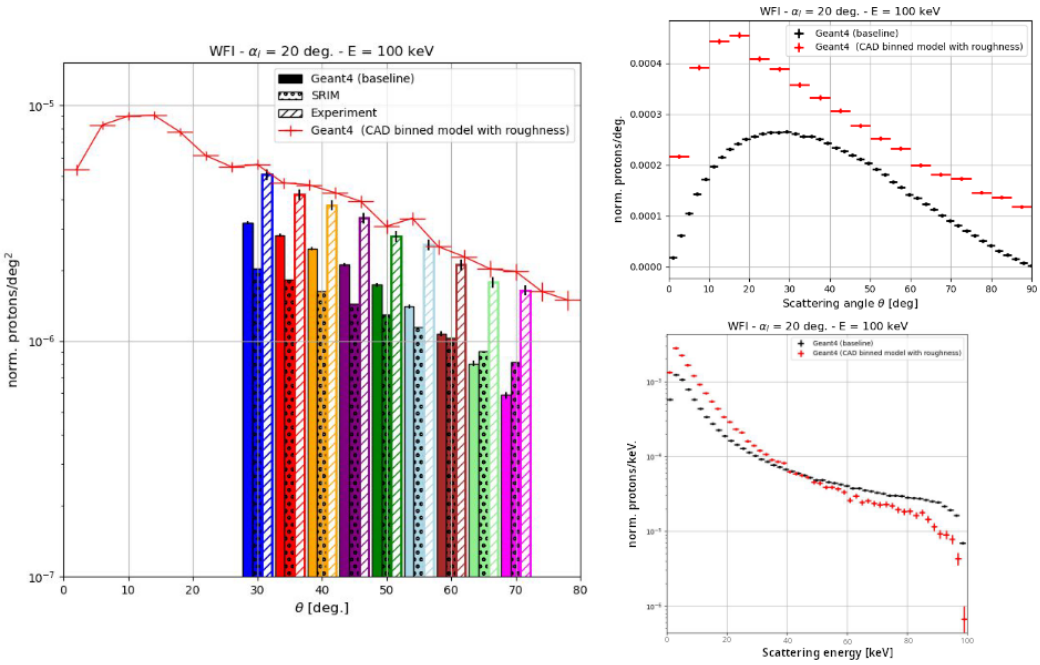

Figure 85: From the CPD Scientific Assessment: Results for the WFI baffle sample with incidence angle of 20 deg, and 100 keV protons fired from the beam. (*left*) Comparison between a baseline Geant4 simulation of an ideal surface, the SRIM simulation, the experimental results, and our Geant4 simulations with roughness and atomic composition. (*top*) A distribution of the proton scattering angles after interactions with the WFI baffle surface sample, compared with the ideal surface. (*bottom*) A distribution of the proton scattering energies after interactions with the WFI baffle surface sample, compared with the ideal surface. [248]

6.4 Results

The ≈one million pixels of the WFI detector registered how much energy was deposited in them. The energy of the primary proton corresponding to each hit was also registered. We have disregarded events where more than one pixel was hit to simplify the pattern reconstruction of the events, since multi-pixel events have less than 1% occurrence.

In Fig. 86 the energy deposition by soft protons in the ATHENA WFI detector is plotted. The background in the most relevant energy band (2-7 keV) was found to be $3.5 \pm 0.2 \times 10^{-5}$ $cm^{-2}s^{-1}keV^{-1}$. This value includes the scattered protons. It is more than an order of magnitude lower than the actual requirement for the WFI detector (5×10^{-4} $cm^{-2}s^{-1}keV^{-1}$) [2].

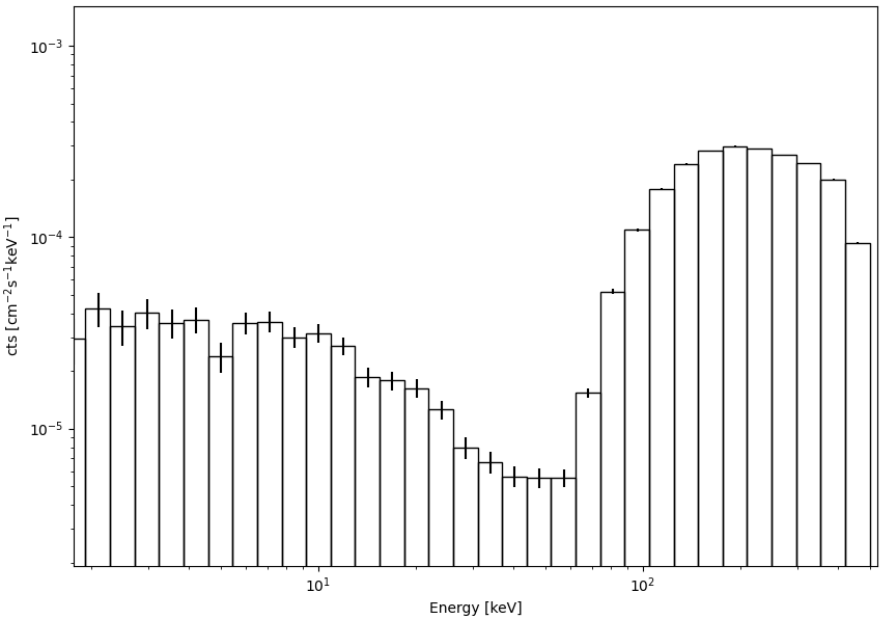

Figure 86: Residual background for the ATHENA WFI. Even though the initial proton energy follows a power law, the protons with lower energy are suppressed as they are deflected by the magnetic field of the CPD. [246]

In order to understand which volumes contribute to the background the most, we have registered each of them as the primary proton passed through. All together there were 279 protons that induced an event in the 2-7 keV energy band. 41 % of them were scattered on the volume which holds the

detector and 44 % of them on the holder of the filter wheel. The rest of the volumes had negligible contribution as the third one by value was the baffle with 8 %.

6.5 Conclusions

A dedicated Geant4 simulation of soft protons entering the WFI detector system of the ATHENA telescope was performed. We proved that the magnetic field designed to deflect protons below 76 keV has the expected effect. We included all the volumes composing the telescope assembly around the WFI detector and we showed that even though the expected residual background increased due to protons scattering on the inner surfaces, its level is still more than an order of magnitude lower than the requirement if the optical blocking filter is present. We also presented the first results on the investigation of volumes responsible for scattering back soft protons into the field of view of the WFI detector.

The simulation of the residual background without the use of the optical blocking filter is planned, together with the use of a more detailed model of the WFI inner structure.

On the micrometer scale flat surfaces were assumed for all of the CAD models. It is important to mention that an undergoing investigation shows that surface roughness can increase the scattering efficiency for such low energy protons. For a specific incident angle and energy: 20° and 100 keV we have shown that the scattering efficiency doubles for the investigated sample.

7 Neutron scattering induced background for the Multi-Blade Detector

7.1 Introduction

The ESS ERIC, currently under construction in Lund, Sweden, aspires to become the most powerful pulsed neutron source in the world. With its long pulse of 2.86 ms and a brilliance higher than 10^{14} n/cm^2/s/sr/Å, it can deliver unprecedented flux on the sample and revolutionise the way neutron experiments are conducted [249, 250]. The produced neutrons are destined to serve a variety of instruments for reflectometry, diffraction, spectrometry and imaging purposes. According to the current schedule the first neutrons will hit the target in 2019, with the user programme starting in 2023.

Reflectometry is an experimental technique present at every neutron source. Hence, two of the first instruments approved for construction at ESS are reflectometers. The one, with a vertical scattering plane, is called the Fast Reflectometer for Extended Interfacial Analysis (FREIA) [251] and the horizontal one is ESTIA [252, 253]. The former one will be optimised for magnetic samples and in-situ or in-operando studies. The latter reflectometer is designed to achieve the best performance for liquid/liquid or liquid/gas interfaces. With a sample flux of 10^9-10^{10} n/s/cm^2 and a high sample reflectivity (∼90%) it is expected that the peak instantaneous rate of the neutron detectors could reach 100 kHz/mm^2 [252, 253]. This value exceeds the rate capability of current neutron detector technologies (including ^{3}He-based detectors) by approximately two orders of magnitude. Additionally, the limit set for neutron scattering inside the detector is lower than what the current state-of-the-art detectors are capable of. These are the two biggest challenges for the detector design aimed at reflectometry for ESS.

In the past ^{3}He-based neutron detectors played a key role for thermal and cold neutron detection. Due to the limitations of these detectors in scientific performance and the shortage of ^{3}He [254], the focus of the neutron detector community has shifted to alternative, higher-performing solutions, such as $^{10}B_4C$-based detectors [255, 256, 257, 258, 259, 260], scintillators [261, 262, 263, 264, 265, 266] or^{6}LiF-based solid state silicon detectors [267]. Additionally, it is already proven that $^{10}B_4C$-based detectors are capable of outperforming ^{3}He detectors in terms of spurious scattering of neutrons [268]. Several studies demonstrate the performance of this detector type and its suitability for neutron scattering experiments [268, 269].

The detector design developed and adopted for the ESS reflectometers is

the Multi-Blade detector [268, 269, 270]. It has been extensively characterised and validated at various neutron facilities and with various types of samples. To get a deeper understanding of the scattering patterns the detector geometry causes and to support the choice of materials and component dimensions, a detailed Geant4 [36, 242] detector model is implemented. The main aim of this simulation effort is to prove that the Multi-Blade detector meets the requirements set by ESS, particularly the scattering of 10^{-4} (see p.9, figure 9.1 in [252]).

In the following sections the Multi-Blade detector is introduced. The details of the Geant4 implementation are presented, as well as the figure of merit used in the subsequent analysis. Fractional scattering is defined and sources of background caused by misplaced detection events are identified and studied as a function of neutron wavelength. The results are discussed with respect to the instrument requirements.

7.2 The Multi-Blade model in Geant4

7.2.1 The Multi-Blade detector

The Multi-Blade detector is a novel neutron detector currently being designed at ESS (see figure 87a). Its development was initiated at Institute Laue-Langevin (ILL) [270, 271]. It consists of a set of successive Multi-Wire Proportional Chambers [272], with $^{10}B_4C$-coated cathodes and Ar/CO_2 (80/20 by volume) as a gas counter mixture. In addition to the anode wires, each chamber is equipped with a strip readout. The strips are perpendicular to the wire direction, in order to achieve two-dimensional spatial resolution.

The detector consists of cassettes as building units. Each one has a boron carbide ($^{10}B_4C$) converter layer that is on a titanium substrate called a "blade". On the other side of the blade a kapton layer and 32 copper strips are located for charge readout. Between the blades 32 wires are stretched at a 4 mm pitch. The blades are tilted in a way that the incoming neutron beam hits the converter layer with an incident angle of 5°, as shown in figure 87b. Therefore the thickness of the converter is viewed by the neutrons as being effectively about 11 times larger [274, 268]. Several cassettes are assembled together forming a fan-like arrangement to achieve the area coverage required for reflectometry.

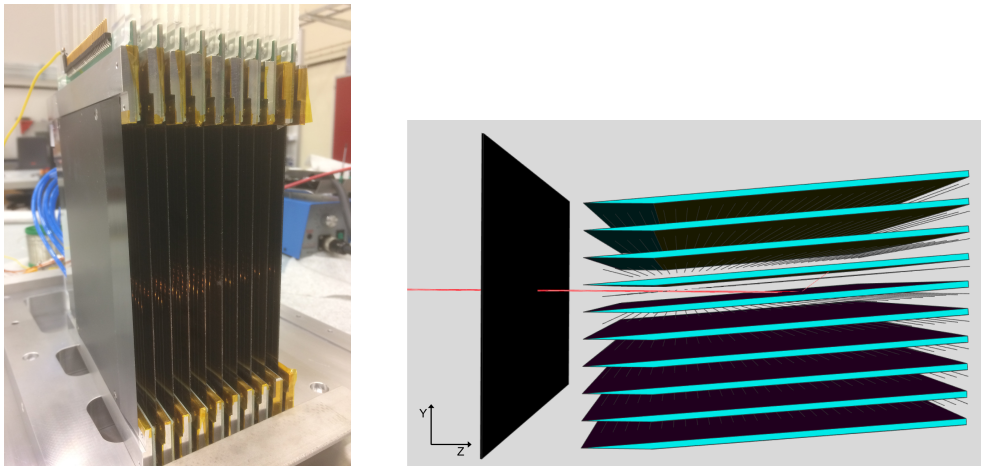

(a) (b)

Figure 87: (a) A prototype of the Multi-Blade detector [269]. (b) Geant4 geometry model being hit by a red neutron beam through the detector entrance window. The vessel is absent from both figures to allow a clear view of the geometry.[273]

7.2.2 Implementation of the detector model in Geant4

It is exactly this fan-like geometry that is the core of the current simulation study. The detector geometry and data analysis are implemented in a framework based on Geant4 developed by the ESS Detector Group [275, 276]. The detector geometry consists of ten 130 mm × 140 mm × 2 mm titanium blades coated with enriched $^{10}B_4C$ by 98% on one side and a kapton and copper layer on the other, with thicknesses of 30 μm and 40 μm respectively. The copper layer is not segmented in strips, unlike the real prototype, as the distance between the strips is 0.1-0.2 mm and the effect of spurious scattering in this part of the detector is negligible compared to other materials. The tungsten wires are also included in the model. The Ar/CO_2 mixture has a ratio of 80/20 by volume and a pressure of 1.1 bar. The gas vessel surrounds the entire detector structure. It consists of enriched $^{10}B_4C$ acting as a total absorber, in order to prevent scattered neutrons from entering the active volume again. On the beam entrance side an aluminium window allows the neutrons to reach the converter (see figure 87b).

All materials are selected from the Geant4 database of NIST materials, except for Ti, Al, Cu and W. The latter are described with the use of the NCrystal library [275, 276], as their crystalline structure is important for the correct treatment of their interaction with thermal neutrons. The physics list used is QGSP_BIC_HP and the Geant4 version is 10.00.p03.

Last, but not least, the neutron generator is a mono-energetic pencil

beam, impinging the converter layer at a 5° angle in the centre of the middle blade, as in figure 87b. The generator parameters, albeit simple, condense the characteristics of typical neutron distributions from reflectometry samples that are important for this study. All results are produced with 1 million events.

7.2.3 Implementation of the detection process in the simulation

In boron-based neutron detectors the secondary charged particles (α and ^{7}Li ions) are created after the ^{10}B nucleus captures a neutron. The cross section of this process is 3835 b for neutrons with a wavelength of 1.8 Å. The position where the neutron is absorbed is called the conversion point. Therefore the neutrons are detected indirectly. The ion products cross the converter and enter the gas volume with a remaining energy. The maximum distance the ^{7}Li and α ions can travel in the specific counting gas is 3 mm and 6 mm respectively at atmospheric pressure and room temperature conditions.

In order to describe the physical phenomena behind the detection of neutrons in the Multi-Blade detector, an approximation is used. The geometrical center of the tracks of the charged particles created by ionisation in the gas of the detector is defined as the hit position (see figure 88). Furthermore, the fact that the readout of the hits is done by wires and strips has to be taken into account. For example, in the direction perpendicular to the blades surface, the coordinate of the hit is measured by the wires. Therefore the position of the triggered wire is read out, not the actual position of the centre of the charge cloud. In order to emulate this effect, the hits are projected to the plane of the boron surface, a transformation that brings the simulation treatment closer to the experimental process.

7.2.4 Comparison of detection efficiency obtained by measurements and Geant4

The simulation results produced with the ESS simulation framework have been previously validated in [277]. An additional validation of the current model is performed in terms of detection efficiency. The results are compared to analytical calculations [270] and experimental measurements performed at the ATHOS instrument of the BNC facility [268] in Hungary and CRISP [269] at ISIS, UK. The observed agreement is within the error bars for most of the neutron wavelengths. The uncertainties of the experimental points depend on the statistics of each measurement and systematic effects on the experimental data are not accounted for in the simulation. In addition, the efficiency estimate of the simulation is affected to a small extent by the fact that

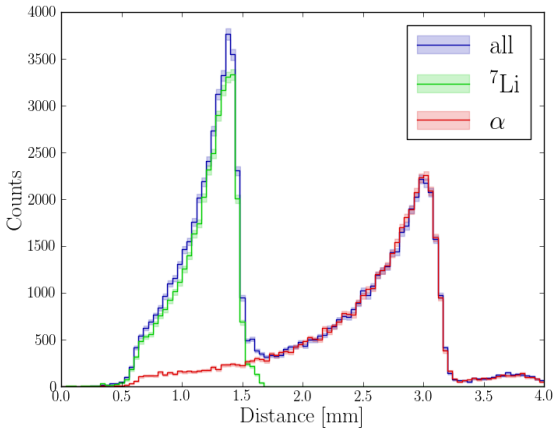

Figure 88: Distance between conversion and hit position as approximated in a simulation for 12 Å neutrons. The two peaks reflect the maximum path of ^{7}Li and α ions respectively, but are halved in this representation (1.5 mm and 3 mm) as a result of the hit definition. The bands around the lines represent the statistical uncertainties.[273]

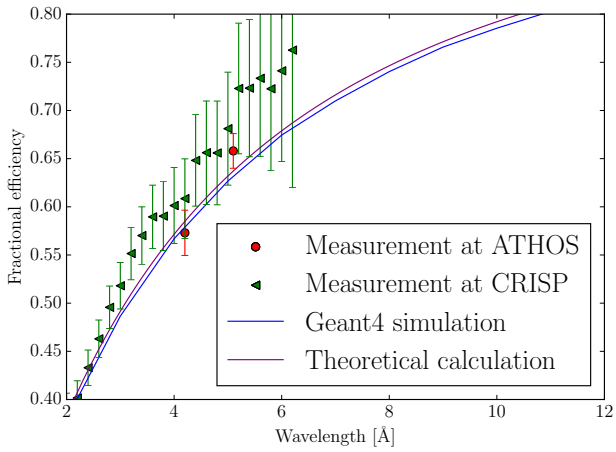

Figure 89: Fractional detection efficiency of the Multi-Blade detector as a function of neutron wavelength, obtained from theoretical calculations [270], measurements [268, 269] and Geant4 simulation (this work).[273]

the detector gas volume is not segmented in the simulation. The detection threshold of 120 keV on the energy deposition is applied per event for the entire gas volume and not per wire, as in the experimental data. However, due to the localised nature of the energy deposition the approximation does not compromise the simulation for the purposes of this work.

7.3 Scattering effects

7.3.1 Definition of spurious detection events

The Multi-Blade is a position sensitive detector, intended to operate in Time-of-Flight (TOF) mode. This means that the energy of the incident neutron is indirectly derived from a time and a 3D position measurement. Two factors can impact the precision of the neutron position reconstruction; the detector spatial resolution (short-scale effect) and scattering (long-scale effect), with different impact to the distribution of the detection coordinates. Figure 90 demonstrates these scenarios. In figure 90a a neutron, which is absorbed in the first converter layer it meets, leads to a secondary particle releasing its energy in the counting gas (the other particle gets stopped inside the cathode substrate and is therefore lost). The spatial resolution of the detector determined by the anode wire pitch and the strip width locally smears the experimental detection point in the data reconstruction process. Figures 90b and 90c depict long-range effects stemming from neutron scattering either within the detector itself or in the entrance window respectively. Such events lead to the miscalculation of the distance between sample and detection point, and eventually to a wrongly derived value for the incident neutron energy and scattering vector.

In order to quantify the impact of the misplaced detected neutrons, an nonphysical technical Geant4 particle, called "geantino", is utilised. This particle is generated along with each primary neutron with the same initial parameters (see figure 90c). Geantinoes do not interact with matter, therefore their tracks are straight lines. The point where a primary neutron would be detected in an ideal measurement is defined by the intersection of the respective geantino track with the first converter layer it traverses. This position is then compared against the respective neutron detection coordinates. The definition of this condition is motivated by the detector design; the actual thickness of the converter is at least 7.5 μm [268, 269] to ensure that, aside from a high detection efficiency, almost all neutrons convert in the first boron layer they encounter, thus reducing the scattering caused by the cathode material.

The utilisation of geantinoes allows for this study to be realised for arbitrary generators and geometries. However, in the current one, due to the fact that primary neutrons start from (0,0,0) and form a pencil beam on the Z axis, the geantino "detection" coordinates are also 0 in X and Y. This means that the actual neutron hit coordinates are sufficient for the visualisation of scattering effects in this particular case ($X_{hit} - X_{geantino} = X_{hit}$, $Y_{hit} - Y_{geantino} = Y_{hit}$). These hit coordinates are the ones projected on the

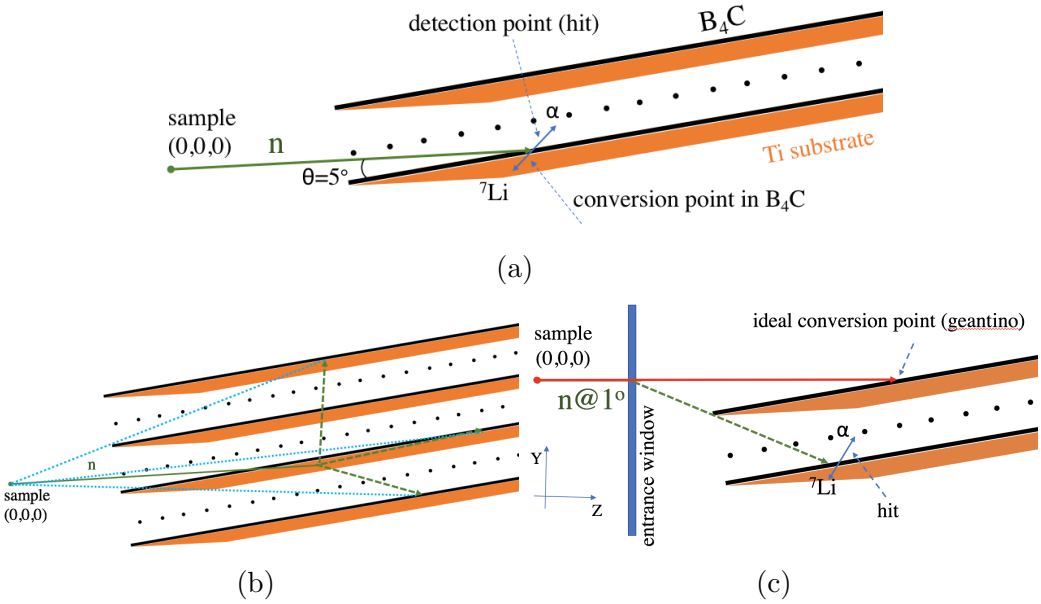

Figure 90: (a) Difference between conversion and detection point. (b) A neutron traversing the first converter layer (solid green) can scatter in the blade material and finally get converted away from the first crossing point (dashed green). This leads to the miscalculation of the distance between sample and detection point (dashed blue). (c) Similarly for a scattered neutron on the detector window. The latter is 1° inclined with respect to the vertical axis. The projection of the detection point on the converter layer is not displayed here for view simplification.[273]

converter layer as explained at the end of subsection 7.2.3.

The contributors to the scattering effects studied in this work are the converter layer and the entrance window of the detector, both looked at as a function of neutron wavelength. The material (Ti) and thickness of the blade (2 mm) have been dictated by engineering needs and the coating process and are fixed for all simulations of this work.

A visualisation of the scattered hits projected on the detector window appear in figure 91. The projection is necessary as the window is not vertical but has a 1° angle with respect to the Y-axis. It is also the standard way of experimentally visualising the data

The primary neutrons hit the centre of the distribution in figure 91a. The simulation is run for the extreme case of 1 Å for the neutron wavelength and 1 cm for the window thickness, in order to maximise the scattering effects. The entries away from the centre make up the scattering events. The asymmetry of the distribution reflects the asymmetry in the registration of the detection events due to the orientation of the blades with respect to the

incident beam. The latter effect is better demonstrable in the projection of figure 91c. Both figures 91b and 91c depict the short-scale effect attributed to the detector resolution, manifesting itself as the Gaussian smearing around 0. The extended tails on either side of the distribution represent the long-scale scattering events. In the case of figure 91c the tails are "modulated" by the succession of the blades in the Y-direction, in addition to the window effects. Such structures are absent in the X-direction because of the detector symmetry along the wire length.

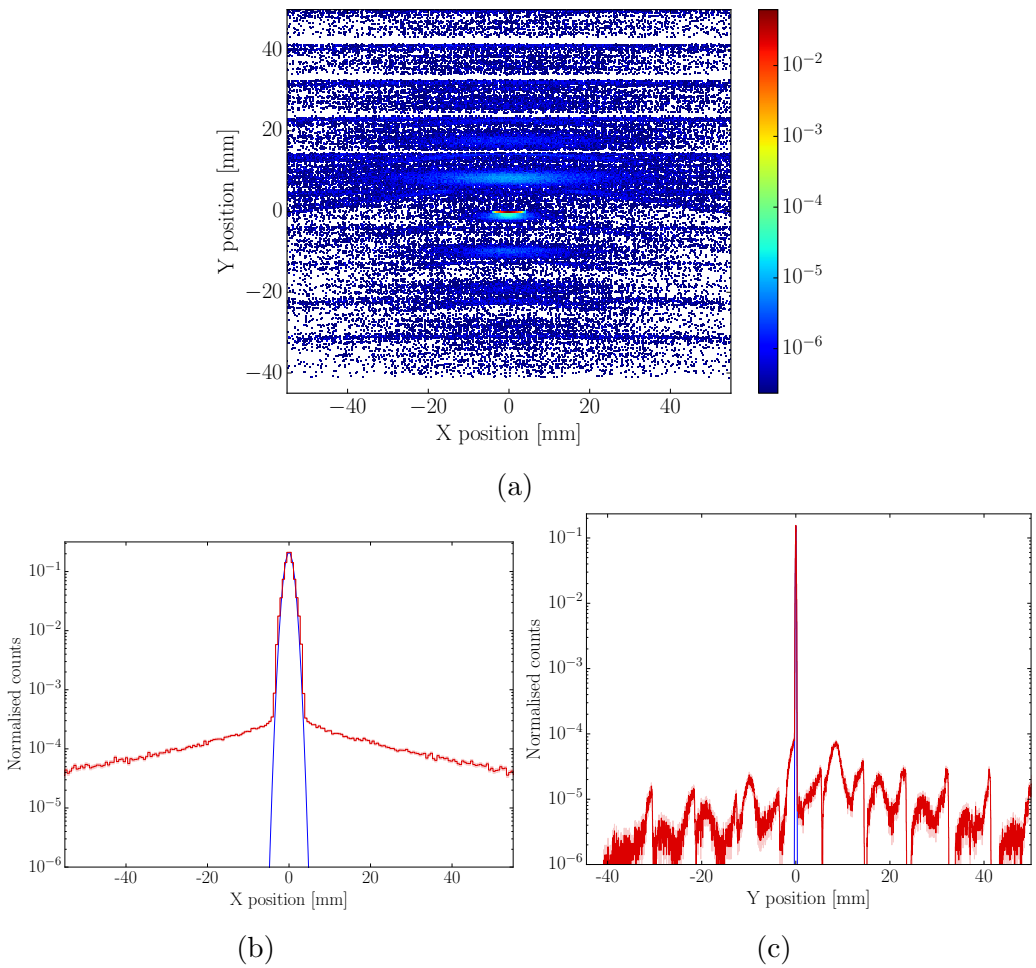

Figure 91: (a) Two-dimensional distribution of hit coordinates, projected on the detector window surface. X (b) and Y (c) projections of distribution (a) in red. The figures are produced with 1 Å neutron wavelength and a window thickness of 1 cm. All distributions are normalised to 1. A Gauss fit of the central bins (in blue) gives σ_X=0.968 mm (FWHM$_X^{fit}$=2.27 mm) and σ_Y=0.0667 mm (FWHM$_Y^{fit}$=0.157 mm).[273]

A detected neutron is considered misplaced, if the detection occurs outside

the 4σ ($\sim$2×FWHM) of the Gaussian fit of the spatial hit distributions (see figures 91b and 91c), i.e. 3.87 mm in the direction parallel to the wires (X-direction) and 0.267 mm in the Y-direction. The σ_X and σ_Y of the two fits indicate minimal impact of scattering on resolution (e.g. $\mathrm{FWHM}_Y^{detector}$=0.55 mm and $\mathrm{FWHM}_Y^{fit} \approx 0.3\times\mathrm{FWHM}_Y^{detector}$). The fraction of scattered neutrons is estimated by summing up all hits that fulfil the above condition and dividing this sum with the total number of detected neutrons, as in the equation below

$$Fraction = \left.\frac{N_{scattered\ neutrons}(|x| \geq 3.87\ mm\ and\ |y| \geq 0.267\ mm)}{N_{all\ neutrons}}\right|_{detected}. \tag{28}$$

This is the figure of merit used in the following subsections, in contrast to the instrument approach, which evaluates the peak-to-tail ratio. The current approach yields higher values of fractional scattering but is important for the detector evaluation.

7.3.2 Comparison of simulation with experimental results

Recently acquired experimental data allow for a comparison with the simulation results. The measurements [269] were performed at the CRISP neutron reflectometer at the ISIS neutron and muon source. The Geant4 model matches the geometrical choices of the respective demonstrator, i.e. the window thickness is 2 mm and the converter layer is 4.4 μm thick in this particular demonstrator. The neutron wavelength in the simulation is set to 1 Å and the beam is pencil-like, while the experimental beam profile was approximately 3 mm × 60 mm. The simulation simplification serves the purpose of providing a clearer picture of the scattering topology and is justified by the detector symmetry along the X-axis.

The basis of the comparison is the Y position of the detection events, as in figure 91c and is shown in figure 92. The experimental data correspond to a wavelength range of 0.5-2.5 Å, achieved via the application of a TOF slice (red distribution of figure 10 in [269]). The simulated coordinates are smeared with a Gaussian of σ=0.42 mm (ca. 2×FWHM) [269]. Only six cassettes were experimentally read-out, therefore only six "peaks" appear in the blue distribution of figure 92. In addition, three wires from the end of each cassette do not contribute to the measurement and have also been accounted for in the simulation by excluding the respective Y histogram bins. The distributions are normalised to their integral.

The Geant4 simulation is able of reproducing the shapes, widths and features of the experimental data. The systematic effects are out of scope

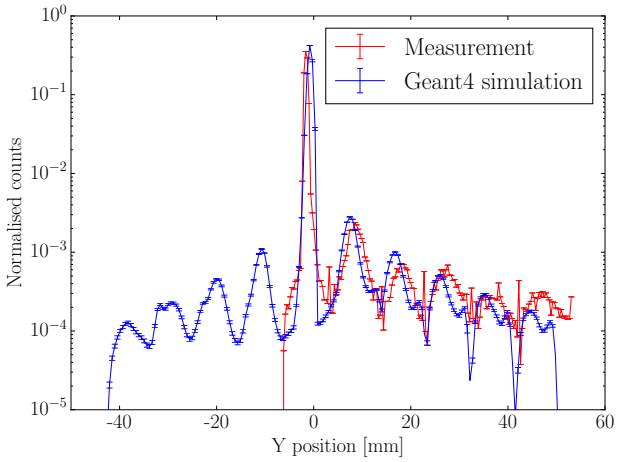

Figure 92: Comparison of Y-position of detected neutrons in measurements taken at CRISP [269] and the results of the simulation (this work).[273]

of the current work. The shape agreement indicates that the simulation reproduces the location of the scattered events and gives confidence that the topology of scattering is understood in a manner sufficient for the purposes of this study. The fraction of scattered neutrons in the simulation is 3.5%. The same fraction estimated from the experimental data amounts to 3.1%.

7.3.3 Impact of the converter thickness

In [268, 269] it is argued that an increase of the converter thickness can respectively increase the fraction of absorbed neutrons, if set to a value higher than 4.4 μm (figure 11 of [269]). The motivation is to prevent as many neutrons from reaching the titanium blade behind the coating, which is the primary contributor to scattering. The detection efficiency anyway saturates at thicknesses above 3 μm [268]. At the same time, an upper value limit needs to be determined, as it is not cost-effective, nor good thin-film deposition practice, to arbitrarily increase the boron carbide thickness.

For the study of the converter thickness the material of the detector window is set to vacuum. Various thicknesses are selected, ranging from typical to extreme. The results are summarised in table 11 and figure 93a, listing the figure of merit defined with equation 28.

The table and figure values represent the scattering which is intrinsic to the detector and is primarily attributed to the blade material. Minor contributions come from the counting gas, the converter and the wires. Figure 93b depicts the distribution of the hit Y position for various converter thicknesses. Clearly, the thicker the coating, the higher the probability is that

λ [Å] c. thickness [μm]	0.1	1	5	7.5	10	20
1	22.250	17.310	4.310	1.840	0.831	0.074
2.5	8.570	5.080	0.265	0.067	0.034	0.022
12	0.460	0.098	0.045	0.040	0.038	0.037

Table 11: Fraction of scattered neutrons in %, as defined in equation 28, for various converter thicknesses and neutron wavelengths.[273]

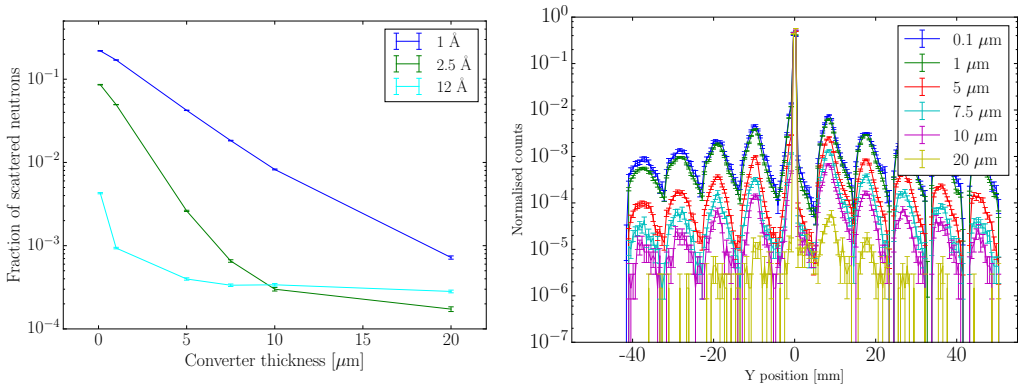

(a) (b)

Figure 93: (a) Fraction of scattered neutrons as defined in equation 28 as a function of converter thickness for various neutron wavelengths. (b) Y position of hits for various converter thicknesses for a neutron wavelength of 1 Å. The entrance window material is set to vacuum. [273]

all neutrons convert and stop in the first layer - regardless of being detected, thus minimising scattering effects inside the detector. Adopting a thickness between 5 μm and 10 μm can reduce the fractional scattering by 1-2 orders of magnitude. The trend in figure 93a demonstrates that for wavelengths above 2.5 Å and 4 Å which are the lowest limit for FREIA and ESTIA respectively, a cost-effective choice of converter thickness would be of the order of 7-8 μm, for the fraction of scattered neutrons to stay below 10^{-3}.

7.3.4 Impact of the detector window thickness

Following the same methodology, the next parameter to be studied is the thickness of the Al detector window. This item is an integral component of the detector, separates the counting gas from the detector environment and assures its operation in vacuum or atmospheric conditions. Similar studies have been performed with other detector types [277]. The values selected represent typical thicknesses used in neutron instruments, in addition to

extreme values. The converter thickness for this series of simulations is now fixed at 7.5 μm. The results are summarised in table 12 and figures 94 and 95. Looking at figure 94, the scattering effects become more significant for lower neutron wavelengths. The result is consistent with the trend of the scattering ,in combination with the absorption cross sections of the materials involved for the specific geometry.

It is interesting to note that a different, e.g. larger detector geometry, would not only scatter differently but also register these events differently. Especially for wavelengths below the Bragg cut-off value of Al and Ti , it is possible to imagine a scenario where the Al window scatters in such a way that although the fraction of scattered neutrons is higher, the scattering angles are such that the neutrons are diverted away from the detector active volume. That is why it is essential to study the impact of the window in combination with the detector response. Scattering is only an issue if it is detected.

The Multi-Blade detector is intended to operate both in vacuum and a normal pressure atmosphere. Given the engineering considerations based on these atmospheric conditions and the fact that the final detector installed at the ESS reflectometers will have a window with a size of 500 mm $\times$ 250 mm, engineering studies show that the window thickness can safely remain below 5 mm for vacuum operation. Recent developments in the ESTIA design promote a neutron flight vessel of a 1 bar Ar/^{4}He mixture, in which case the Multi-Blade detector can be operated with a thin foil (ca. 25-100 μm) instead of a window. In summary, for the wavelengths of interest, the fraction of scattered neutrons at the presence of the window is within acceptable limits.

λ [Å] window thickness [mm]	0	0.1	1	5	10
1	1.840	1.870	1.970	2.480	3.060
2.5	0.063	0.069	0.098	0.238	0.398
4	0.030	0.030	0.039	0.088	0.187
6	0.030	0.031	0.036	0.054	0.075
12	0.041	0.041	0.046	0.073	0.103

Table 12: Fraction of scattered neutrons in %, as defined in equation 28, as a function of window thickness and neutron wavelength for a converter thickness of 7.5 μm.[273]

The impact of the detector window is also demonstrable in figure 95. In figure 95a the lower peaks on either side of the centre are at least 4 orders of magnitude below the peak containing the non-scattered events, especially for the values of interest above 2.5 Å. This value satisfies the instrument

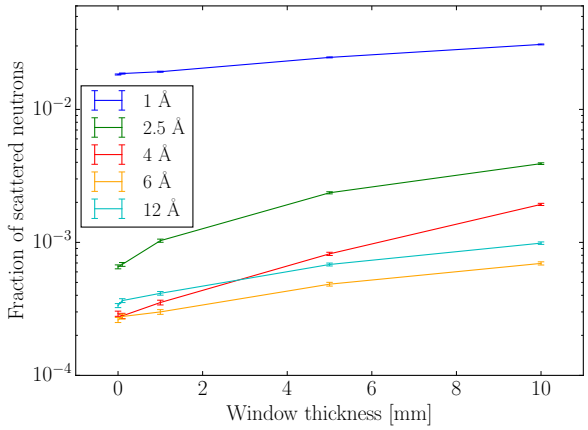

Figure 94: Fraction of scattered neutrons as defined in equation 28 as a function of window thickness for various wavelengths and a converter thickness of 7.5 μm. [273]

requirement, the way it is defined as a peak-to-tail ratio. As expected, the fractional scattering decreases as neutrons get colder.

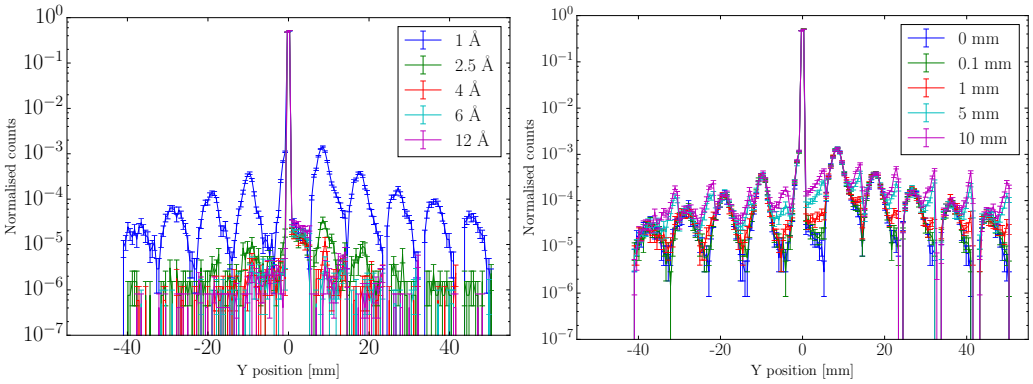

(a) (b)

Figure 95: (a) Y position of hits for various neutron wavelengths and no detector window for converter thickness of 7.5 μm. (b) Same distribution for 1 Å with varying window thicknesses. [273]

7.4 Conclusions

A detailed Geant4 model of the Multi-Blade detector is implemented, in order to identify and quantify scattering effects. To this end, a parameter scan is performed focusing mainly on the effects related to the converter thickness and the detector window. The substrate material and thickness have been experimentally optimised and therefore the engineering values are used in the simulation. Various neutron wavelengths of relevance for ESS reflectometry are used.

A comparison of the simulation with experimental results obtained at the CRISP reflectometer confirms our understanding of the detection and scattering topology within the detector. It is shown that the degradation in spatial resolution due to scattering is smaller than the detector resolution. The result of the converter thickness study supports the design choice to increase this value to 7.5 μm, with a 2 orders of magnitude gain in terms of scattering suppression. As for the detector window, its impact is within the instrument requirements for the values that result from the engineering studies, in particular for detector operation in vacuum.

Last but not least, this study selects the amount of fractional scattering as a figure of merit. It follows a cumulative approach in contrast to the instrument one, in the sense that the background is integrated over the entire tail length of the coordinate distributions, while the instrument requirements are expressed more as a peak-to-tail ratio. This implies that the cumulative approach presented here leads to an overestimate of the scattering effects by at least half an order of magnitude. For neutron wavelengths above 2.5 Å, the peak-to-tail ratio is higher than 4 orders of magnitude, which means that the current implementation of the MultiBlade detector more than satisfies the ESS reflectometry needs.

8 Summary

I have calculated the residual background for several satellites (ATHENA, HERMES, CAMELOT) and in some cases made recommendations on how the background can be decreased. I have also quantified the background for the novel Multi-Blade neutron detector. Furthermore I have written a machine learning software that suppresses the background in volcano muography.

I have developed a novel machine learning tool to distinguish between background and signal in volcano muography with the MOS system. Since in the measurement we do not have the energy of the muons that is needed for teaching the machine learning model I developed a detailed Geant4 simulation. The simulation was validated with measurements. Additionally the tracking software of our group was tested with the developed simulation. The developed neural network suppresses background four times better than the traditional χ^2 method (for 1 GeV muons with a χ^2 cut of 4). [24]

I have proved that the first gamma-ray CubeSat observatory will be capable of detecting short gamma-ray bursts, long gamma-ray bursts and terrestrial gamma-ray flashes. I developed a framework based on a Geant4 simulation that calculates the signal-to-noise ratio of satellites utilizing scintillator detectors. I have determined the signal-to-noise ratio of the Camelot satellite including all background sources. Furthermore I have simulated the transient astrophysical sources including short and long gamma-ray-bursts and proven that the satellite will be more than capable of detecting the investigated transient sources.[39, 38]

I quantified the proton induced in-orbit activation for the HERMES CubeSat. In order to do this I developed a hybrid framework based on a Geant4 simulation and analytical solution of the Bateman equation to calculate the proton induced activation of satellites, and to determine the proton induced activation of the HERMES satellite for several orbits. I have proven that the background level is below the requirements. The framework was tested with measurements. [221]

I have derived the residual background from scattering of soft protons on the inner surfaces of the Athena satellite and developed a simulation to estimate the effect of surface roughness on the scattering of soft protons on the μm scale in Geant4 with models produced by Scanning Probe Microscope (validated by measurements) [246, 248]

I have proved that the novel material analysis that we have developed is capable of distinguishing materials. I have shown that cosmic muons produce secondary particles depending on the density and atomic number of material. Understood how this novel method can be optimized by Geant4 simulations.

I have also proven that by placing scintillators under the target we can cut the acquisition time in half. This result was used for building the COMIS system in Budapest. [37]

I have quantified the cumulative contribution of various detector components to the scattering of neutrons and to prove that the respective effect is within the requirements set for the Multi-Blade detector by the ESS reflectometers. I have shown that increasing the converter thickness to 7.5 μm would yield a scattering suppression of 2 orders of magnitude for the neutron wavelength of 2.5 [Å]. [273]

9 Acknowledgement

I would like to express my gratitude to my supervisor Dezső Varga and my internal supervisor at ELTE, Norbert Werner. Without their guidance I would not have been able to finish this work.

I am grateful for all the colleagues who I had the chance to work with during my studies. Gergő Hamar has taught me the basics of muography and detector physics. László Oláh with whom we worked together on the MOS detectors at Sakurajima. Balázs Újvári introduced me to Geant4. Kalliopi Kanaki has taught me the most on neutron related physics. Riccardo Campana has guided me through my first particle simulations on satellites. Jakub Ripa has provided the background components in Low Earth Orbit. Jakub Zlámal provided the CAD models for the ATHENA satellites. Valentina Fioretti has kindly shared the mass model of the WFI detector of the ATHENA satellite and helped me understand low energy proton scattering. With Gábor Albrecht we have designed the first prototype of the neural network for background suppression in muography.

Last but not least I am grateful to my family and girlfriend who supported me through the ups and downs of my PhD studies.

References

[1] Luis W. Alvarez et al.
Search for hidden chambers in the pyramids
Science, 167:832 (1970)
DOI: 10.1126/science.167.3919.832

[2] Particle Data Group
Astrophysics and cosmology
Physics Letters B, vol. 592, 186-234 (2004)
DOI: 10.1016/j.physletb.2004.06.011

[3] A. Tang et al.
Muon Simulations for Super-Kamiokande, KamLAND and CHOOZ
Phys. Rev. D 74, 053007 (2006)
DOI: 10.1103/PhysRevD.74.053007

[4] D.E. Groom et al.
Muon stopping-power and range tables: 10 MeV–100 TeV
Atomic Data and Nuclear Data Tables 78 183 (2001)
DOI: 10.1006/adnd.2001.0861

[5] H. K. M. Tanaka et al.
Three dimensional CAT scan of a volcano with cosmic-ray muon radiography, Journal of Geophysical Research 115 B12332 (2010)
DOI: 10.1029/2010JB007677

[6] H. K. M. Tanaka et al.
Cosmic-ray muon imaging of magma in a conduit: degassing process of Satsuma-Iwojima Volcano, Japan
Geophys.Res. Lett., 36 L01304 (2009)
DOI: 10.1029/2008GL036451

[7] H. K. M. Tanaka et al.
Imaging the conduit size of the dome with cosmic ray muons: The structure beneath Showa Shinzan Lava Dome, Japan
Geophys. Res. Lett., vol. 34, L22311 (2007)

DOI: 10.1029/2007GL031389

[8] T. Kusagaya et al., Muographic imaging with a multi-layered telescope and its application to the study of the subsurface structure of a volcano
Proc. Jpn. Acad. Ser. B 91 501 (2015)
DOI: 10.2183/pjab.91.501

[9] H. K. M. Tanaka
Instant snapshot of the internal structure of Unzen lava dome, Japan with airborne muography.
Sci. Rep. 6 39741 (2016)
DOI: 10.1038/srep39741

[10] N. Lesparre et al.
Density Muon Radiography of La Soufrière of Guadeloupe Volcano: Comparison with Geological, Electrical Resistivity and Gravity data
Geophysical Journal International, vol. 190, 1008 (2012)
DOI: 10.1111/j.1365-246X.2012.05546.x

[11] C. Carloganu
TOMUVOL muography project
MUOGRAPHERS 2016, Tokyo, November 7, (2016)
http://www.eri.u-tokyo.ac.jp/ht/MUOGRAPHERS16/General-Assembly/program.html

[12] V. Tioukov et al.
Muography with nuclear emulsions - Stromboli and other projects
Annals of Geophysics 60, S0111 (2017)
DOI: 10.4401/ag-7386

[13] D. Carbon et al.
An experiment of muon radiography at Mt Etna (Italy)
Geophysical Journal International
196 633 (2014)
DOI: 10.1093/gji/ggt403

[14] D. Varga et al.
High Efficiency Gaseous Tracking Detector for Cosmic Muon Radiography
Advances in high energy physics 1962317 (2016)
DOI: 10.1155/2016/1962317

[15] D. Varga et al.,
Detector developments for high performance Muography applications
NIM A 162236 (2020)
DOI: 10.1016/j.nima.2019.05.077

[16] L. Oláh et al.,
Plug Formation Imaged Beneath the Active Craters of Sakurajima Volcano With Muography
Geophysical research letters 10.1029 (2019)
DOI: 10.1029/2019GL084784

[17] L. Oláh et al.
Investigation of the limits of high-definition muography for observation of Mt Sakurajima.
Philosophical transactions of the Royal Society A 2018.0135 (2018)
DOI: 10.1098/rsta.2018.0135

[18] R. Nishiyama et al.,
Monte Carlo simulation for background study of geophysical inspection with cosmic-ray muons.
Geophysical Journal International 2606015 (2016)
DOI: 10.1093/gji/ggw191

[19] L. Oláh et al.
High-definition and low-noise muography of the Sakurajima volcano with gaseous tracking detectors
Scientific Reports 3207 (2018)
DOI: 10.1038/s41598-018-21423-9

[20] J. Peña-Rodríguez et al.,
Muography background sources: simulation, characterization, and

machine-learning rejection.
37th International Cosmic Ray Conference proceedings (2021)
DOI: 10.22323/1.395.0400

[21] H. Gómez et al.,
Forward scattering effects on muon imaging
JINST, vol. 12, 12018 (2018)
DOI: 10.1088/1748-0221/12/12/P12018

[22] Bethe, H. A. et al.
Moliere's Theory of Multiple Scattering
Phys. Rev., vol. 89, 1256 (1953)
DOI: 10.1103/PhysRev.89.1256

[23] https://pypi.org/project/pylandau/
Last visited 1/3/2023

[24] Olah, L. et al.
Development of Machine Learning-Assisted Spectra Analyzer for the NEWCUT Muon Spectrometer
Journal for Advanced Instrumentation in Science (2022)
DOI: 10.31526/jais.2022.264

[25] A. P. Bradley
The use of the area under the ROC curve in the evaluation of machine learning algorithms
Pattern Recognition, vol. 30, Issue 7, (1997)
DOI: 10.1016/S0031-3203(96)00142-2

[26] L. W. Alvarez et al.
Search for hidden chambers in the pyramids
Science, vol. 167, 832-839 (1970)
DOI: 10.1126/science.167.3919.8

[27] L. Malmqvist et al.
Theoretical studies of in-situ rock density determination using cosmic-ray muon intensity measurements with application in mining

geophysics
Geophysics, vol. 44, 1485-1622, (1979)
DOI: 10.1190/1.1441026

[28] H. Tanaka et al.
Detecting a mass change inside a volcano by cosmic-ray muon radiography (muography): First results from measurements at Asama volcano, Japan
Geophys. Res.Lett, vol. 36, 17302 (2009)
DOI: 10.1029/2009GL039448

[29] K. Terada et al.
A new X-ray fluorescence spectroscopy for extraterrestrial materials using a muon beam
Scientific Reports, vol. 4, 5072 (2014)
DOI: 10.1038/srep05072

[30] James J. Reidy et al.
Use of Muonic X Rays for Nondestructive Analysis of Bulk Samples for Low Z Constituents
Analytical Chemistry, vol. 50, 40-44 (1978)
DOI: 10.1021/ac50023a015

[31] Bogdanov, A.G.
Geant4 simulation of production and interaction of Muons
IEEE Transactions on Nuclear Science, vol. 53(2), 513-519 (2006)
DOI: 10.1109/TNS.2006.872633

[32] D. Mrdja, I. Bikit et al.
First cosmic-ray images of bone and soft tissue
EPL (Europhysics Letters), vol. 116, 58001 (2016)

[33] I. Bikit et al.
Novel approach to imaging by cosmic-ray muons
Europhysics Letters, vol. 113, 48003 (2016) DOI: 10.1209/0295-5075/113/58001

[34] D. Varga et al.
Asymmetric Multi-Wire Proportional Chamber with reduced requirements to mechanical precision
NIM A, vol. 648, 163-167 (2011)
DOI: 10.1016/j.nima.2011.05.049

[35] J.Allison et al.
Recent developments in Geant4
NIM A: Accelerators, Spectrometers, Detectors and Associated Equipment, vol. 835, 186-225 (2016)
DOI: 10.1016/j.nima.2016.06.125

[36] Allison, John et al.
Recent developments in Geant4
Nuclear Instruments and Methods in Physics Research Section A: Accelerators, Spectrometers, Detectors and Associated Equipment, vol. 835, 186-225 (2016)
DOI: 10.1016/j.nima.2016.06.12

[37] Galgoczi, G. et al.
Imaging by muons and their induced secondary particles — a novel technique
Innovative Particle and Radiation Detectors 2019 proceedings
JINST, vol. 15 (2020)
DOI: 10.1088/1748-0221/15/06/C06014

[38] Galgoczi, G. et al.
Simulations of expected signal and background of gamma-ray sources by large field-of-view detectors aboard CubeSats
J. Astron. Telesc. Instrum. Syst., vol. 7
DOI: 10.1117/1.JATIS.7.2.028004

[39] Ripa J. et al.
Estimation of the detected background by the future gamma ray transient mission CAMELOT
Astronomische Nachrichten, vol. 340, 7666673 (2019)
DOI: 10.1002/asna.201913673

[40] Werner, Norbert et al.
CAMELOT: Cubesats Applied for MEasuring and LOcalising Transients mission overview
Proceedings of the SPIE, Society of Photo-Optical Instrumentation Engineers (SPIE) Conference Series (2018)
DOI: 10.1117/12.2313764

[41] Pál, András et al.
CAMELOT - Concept study and early results for onboard data processing and GPS-based timestamping
arXiv e-prints (2018)

[42] Ripa, Jakub et al.
Monitoring of gamma-ray bursts with a fleet of nanosatellites
69th International Astronautical Congress (2018)

[43] Smith, J. et al.
BurstCube: Mission Concept, Performance, and Status
36th International Cosmic Ray Conference (ICRC2019), International Cosmic Ray Conference (2019)
DOI: 10.22323/1.358.0604

[44] Perkins, J. S. et al.
BurstCube: A CubeSat for Gravitational Wave Counterparts
35th International Cosmic Ray Conference (ICRC2017), volume 301 (2017)
DOI: 10.22323/1.301.0760

[45] Chattopadhyay, Tanmoy et al.
BlackCAT CubeSat: a soft x-ray sky monitor, transient finder, and burst detector for high-energy and multimessenger astophysics
Space Telescopes and Instrumentation 2018: Ultraviolet to Gamma Ray, Society of Photo-Optical Instrumentation Engineers (SPIE) Conference Series (2018)
DOI: 10.1117/12.2314274

[46] Zheng, Shijie
The status of GECAM mission
The Extragalactic Explosive Universe: the New Era of Transient Surveys and Data-Driven Discovery (2019)
DOI: 10.5281/zenodo.3478126

[47] Wen, Jiaxing et al.
GRID: a student project to monitor the transient gamma-ray sky in the multi-messenger astronomy era
Experimental Astronomy, vol. 48, 77-95 (2019)
DOI: 10.1007/s10686-019-09636-w

[48] Grove, J. E. et al.
Glowbug, a Low-Cost, High-Sensitivity Gamma-Ray Burst Telescope
arXiv e-prints (2020)

[49] Fuschino, F. et al.
HERMES: An ultra-wide band X and gamma-ray transient monitor on board a nano-satellite constellation
Nuclear Instruments and Methods in Physics Research A, vol. 936, 199-203 (2019)
DOI: 10.1016/j.nima.2018.11.072

[50] Pearce, M. et al.
Science prospects for SPHiNX - A small satellite GRB polarimetry mission
Astroparticle Physics, vol. 104, 54-63 (2019)
DOI: 10.1016/j.astropartphys.2018.08.007

[51] Ripa, Jakub et al.
Estimation of the detected background by the future gamma ray transient mission CAMELOT
Astronomische Nachrichten, vol. 340, 666-673 (2019)
DOI: 10.1002/asna.201913673

[52] Bagoly, Zsolt et al.
Transient detection capabilities of small satellite gamma-ray detectors

Astronomische Nachrichten, vol. 340, 681-689 (2019)
DOI: 10.1002/asna.201913675

[53] Vedrenne, Gilbert et al.
Gamma-Ray Bursts: The brightest explosions in the Universe (2009)
ISBN-10: 3540390855

[54] Kouveliotou, Chryssa et al.
Gamma-ray Bursts (2012)
DOI: 10.1017/CBO9780511980336

[55] Levan, Andrew
Gamma-Ray Bursts (2018)
DOI: 10.1088/2514-3433/aae164

[56] Zhang, Bing
The Physics of Gamma-Ray Bursts (2019)
DOI: 10.1017/9781139226530

[57] Kouveliotou, C. et al.
Identification of two classes of gamma-ray bursts
The Astrophysical Journal, vol. 413, L101-L104 (1993)

[58] Mereghetti, S et al.
The strongest cosmic magnets: soft gamma-ray repeaters and anomalous X-ray pulsars
The Astronomy and Astrophysics Review, vol. 15, 225-287 (2008)
DOI: 10.1007/s00159-008-0011-z

[59] Yamaoka, Kazutaka et al.
Suzaku Wide-band All-sky Monitor (WAM) observations of GRBs and SGRs
Publications of the Astronomical Society of Japan, vol. 69, R2 (2017)
DOI: 10.1093/pasj/psx026

[60] Lindanger, Anders et al.
Journal of Geophysical Research: Atmospheres (2020)
DOI: 10.1029/2019JD03198

[61] Dwyer, Joseph R. et al.
High-Energy Atmospheric Physics: Terrestrial Gamma-Ray Flashes and Related Phenomena
Space Science Reviews, vol. 173, 133-196 (2012)
DOI: 10.1007/s11214-012-9894-0

[62] von Kienlin, A. et al.
The Fourth Fermi-GBM Gamma-Ray Burst Catalog: A Decade of Data
The Astrophysical Journal, vol. 893, 46 (2020)
DOI: 10.3847/1538-4357/ab7a18

[63] Narayana Bhat, P. et al.
The Third Fermi GBM Gamma-Ray Burst Catalog: The First Six Years
The Astrophysical Journal Supplement, vol. 223, 28 (2016)

[64] Goldstein, A. et al.
Updates to the Fermi-GBM Short GRB Targeted Offline Search in Preparation for LIGO's Second Observing Run
arXiv e-prints (2016)

[65] Duncan, Robert C. et al.
Formation of Very Strongly Magnetized Neutron Stars: Implications for Gamma-Ray Bursts
The Astrophysical Journal Letters, vol. 392, L9 (1992)
DOI: 10.1086/186413

[66] Thompson, Christopher et al.
The soft gamma repeaters as very strongly magnetized neutron stars - I. Radiative mechanism for outbursts
Monthly Notices of the Royal Astronomical Society, vol. 275, 255-300 (1995)

DOI: 10.1093/mnras/275.2.255

[67] Thompson, Christopher et al.
The Soft Gamma Repeaters as Very Strongly Magnetized Neutron Stars. II. Quiescent Neutrino, X-Ray, and Alfven Wave Emission
The Astrophysical Journal, vol. 473, 322 (1996)
DOI: 10.1086/178147

[68] Mazets, E. P. et al.
Observations of a flaring X-ray pulsar in Dorado
Nature, vol. 282, 587-589 (1979)
DOI: 10.1038/282587a0

[69] Hurley, K. et al.
γ-ray bursts
Nature, vol. 434, 1098-1103 (2005)
DOI: 10.1038/nature03519

[70] Mazets, E. P. et al.
The Konus-Wind and Helicon-Coronas-F detection of the giant γ-ray flare from the soft γ-ray repeater SGR 1806-20
arXiv e-prints (2005)

[71] Mereghetti, S. et al.
The First Giant Flare from SGR 1806-20: Observations Using the Anticoincidence Shield of the Spectrometer on INTEGRAL
The Astrophysical Journal Letters, vol. 624, L105-L108 (2005)
DOI: 10.1086/430669

[72] Palmer, D. M. et al.
γ-ray flare from the magnetar SGR 1806 - 20
Nature, vol. 434, 1107-1109 (2005)
DOI: 10.1038/nature03525

[73] Terasawa, Toshio et al.
Repeated injections of energy in the first 600ms of the giant flare of

SGR1806-20
Nature, vol. 434, 1110-1111 (2005)
DOI: 10.1038/nature03573

[74] Lewin, Walter H. G. et al.
Compact Stellar X-ray Sources (2009)
DOI: 10.1017/CBO9780511536281

[75] Aptekar, R. L. et al.
Konus Catalog of Soft Gamma Repeater Activity: 1978 to 2000
The Astrophysical Journal Supplement, vol. 137, 227-277 (2001)
DOI: 10.1086/322530

[76] Fishman, G. J. et al.
Discovery of Intense Gamma-Ray Flashes of Atmospheric Origin
Science, vol. 264, 1313-1316 (1994)
DOI: 10.1126/science.264.5163.1313

[77] Smith, David M. et al.
Terrestrial Gamma-Ray Flashes Observed up to 20 MeV
Science, vol. 307, 1085-1088 (2005)
DOI: 10.1126/science.1107466

[78] Grefenstette, B. W. et al.
First RHESSI terrestrial gamma ray flash catalog
Journal of Geophysical Research (Space Physics), vol. 114, A02314 (2009)
DOI: 10.1029/2008JA013721

[79] Briggs, M. S. et al.
First results on terrestrial gamma ray flashes from the Fermi Gamma-ray Burst Monitor
Journal of Geophysical Research (Space Physics), vol. 115, A07323 (2010)
DOI: 10.1029/2009JA015242

[80] Fishman, G. J. et al.
Temporal properties of the terrestrial gamma-ray flashes from the Gamma-Ray Burst Monitor on the Fermi Observatory
Journal of Geophysical Research (Space Physics), vol. 116, A07304 (2011)
DOI: 10.1029/2010JA016084

[81] Roberts, O. J. et al.
The First Fermi-GBM Terrestrial Gamma Ray Flash Catalog
Journal of Geophysical Research (Space Physics), vol. 123, 4381-4401 (2018)
DOI: 10.1029/2017JA024837

[82] Marisaldi, M. et al.
AGILE Observations of Terrestrial Gamma-Ray Flashes
2011 Fermi Symposium proceedings - eConf C110509 (2011)

[83] Marisaldi, M. et al.
Properties of terrestrial gamma ray flashes detected by AGILE MCAL below 30 MeV
Journal of Geophysical Research (Space Physics), vol. 119, 1337-1355 (2014)
DOI: 10.1002/2013JA019301

[84] Marisaldi, M. et al.
Enhanced detection of terrestrial gamma-ray flashes by AGILE
Geophysical Research Letters, vol. 42, 9481-9487 (2015)
DOI: 10.1002/2015GL066100

[85] Labanti, C. et al.
Design and construction of the Mini-Calorimeter of the AGILE satellite
Nuclear Instruments and Methods in Physics Research A, vol. 598, 470-479 (2009)
DOI: 10.1016/j.nima.2008.09.021

[86] Maiorana, Carolina et al.
Journal of Geophysical Research: Atmospheres (2020)
DOI: 10.1029/2019JD03198

[87] Marisaldi, Martino et al.
Journal of Geophysical Research: Atmospheres, vol. 124, 7484-7497 (2019)
DOI: 10.1029/2019JD03055

[88] Tierney, D. et al.
Fluence distribution of terrestrial gamma ray flashes observed by the Fermi Gamma-ray Burst Monitor
Journal of Geophysical Research (Space Physics), vol. 118, 6644-6650 (2013)
DOI: 10.1002/jgra.50580

[89] Giacconi, Riccardo et al.
Evidence for x Rays From Sources Outside the Solar System
Physical Review Letters, vol. 9, 439-443 (1962)
DOI: 10.1103/PhysRevLett.9.439

[90] Kasturirangan, K. et al.
Spectrum of the Cosmic X- and Gamma Ray Background in the Energy Range 1 keV-1 MeV
Astrophysics and Space Science, vol. 15, 161-166 (1972)
DOI: 10.1007/BF00649950

[91] Schwartz, Daniel A. et al.
The Spectrum of Diffuse Cosmic X-Rays Observed by OSO-3 Between 7 and 100 KEV
The Astrophysical Journal, vol. 190, 297-304 (1974)
DOI: 10.1086/152876

[92] Schoenfelder, V. et al.
Diffuse cosmic and atmospheric MeV gamma radiation from balloon observations.
The Astrophysical Journal, vol. 217, 306-319 (1977)

DOI: 10.1086/155580

[93] Fichtel, C. E. et al.
Diffuse gamma radiation.
The Astrophysical Journal, vol. 222, 833-849 (1978)
DOI: 10.1086/156202

[94] Schoenfelder, V. et al.
The vertical component of 1-20 MeV gamma rays at balloon altitudes
The Astrophysical Journal, vol. 240, 350-362 (1980)
DOI: 10.1086/158239

[95] Boldt, E.
The Cosmic X-Ray Background
Comments on Astrophysics, vol. 9, 97 (1981)

[96] Gehrels, Neil
Instrumental background in gamma-ray spectrometers flown in low earth orbit
Nuclear Instruments and Methods in Physics Research, Section A, vol. 313, 513-528 (1992)
DOI: 10.1016/0168-9002(92)90832-O

[97] Horstman, H. M. et al.
The X and gamma diffuse background.
Nuovo Cimento Rivista Serie, vol. 5, 255-311 (1975)
DOI: 10.1007/BF02747042

[98] Sreekumar, P. et al.
EGRET Observations of the Extragalactic Gamma-Ray Emission
The Astrophysical Journal, vol. 494, 523-534 (1998)
DOI: 10.1086/305222

[99] Dean, A. J. et al.
The Modelling of Background Noise in Astronomical Gamma Ray Telescopes

Space Science Reviews, vol. 105, 285-376 (2003)
DOI: 10.1023/A:1023995803108

[100] Mizuno, T. et al.
Cosmic-Ray Background Flux Model Based on a Gamma-Ray Large Area Space Telescope Balloon Flight Engineering Model
The Astrophysical Journal, vol. 614, 1113-1123 (2004)
DOI: 10.1086/423801

[101] Churazov, E. et al.
INTEGRAL observations of the cosmic X-ray background in the 5-100 keV range via occultation by the Earth
Astronomy and Astrophysics, vol. 467, 529-540 (2007)
DOI: 10.1051/0004-6361:20066230

[102] Frontera, Filippo et al.
The Cosmic X-Ray Background and the Population of the Most Heavily Obscured AGNs
The Astrophysical Journal, vol. 666, 86-95 (2007)
DOI: 10.1086/519985

[103] Zombeck, Martin
Handbook of Space Astronomy and Astrophysics: Third Edition
2007

[104] Ajello, M. et al.
Cosmic X-Ray Background and Earth Albedo Spectra with Swift BAT
The Astrophysical Journal, vol. 689, 666-677 (2008)
DOI: 10.1086/592595

[105] Ajello, M. et al.
The Evolution of Swift/BAT Blazars and the Origin of the MeV Background
The Astrophysical Journal, vol. 699, 603-625 (2009)
DOI: 10.1088/0004-637X/699/1/603

[106] Moretti, A. et al.
A new measurement of the cosmic X-ray background
Astronomy and Astrophysics, vol. 493, 501-509 (2009)
DOI: 10.1051/0004-6361:200811197

[107] Türler, M. et al.
INTEGRAL hard X-ray spectra of the cosmic X-ray background and Galactic ridge emission
Astronomy and Astrophysics, vol. 512, A49 (2010)
DOI: 10.1051/0004-6361/200913072

[108] Campana, Riccardo et al.
Background simulations for the Large Area Detector onboard LOFT
Experimental Astronomy, vol. 36, 451-477 (2013)
DOI: 10.1007/s10686-013-9341-6

[109] Ackermann, M. et al.
The Spectrum of Isotropic Diffuse Gamma-Ray Emission between 100 MeV and 820 GeV
The Astrophysical Journal, vol. 799, 86 (2015)
DOI: 10.1088/0004-637X/799/1/86

[110] Bagoly, Z. et al.
Cosmological Constraints on the Clustering of X-Ray Background Sources
The Astrophysical Journal, vol. 333, 54 (1988)
DOI: 10.1086/166723

[111] Meszaros, A. et al.
Large-Scale Structure of the Universe: Constraints from the X-Ray Background
The Astrophysical Journal, vol. 327, 25 (1988)
DOI: 10.1086/166164

[112] Bi, H. G. et al.
On the large scale structure of X-ray background sources

Astronomy and Astrophysics, vol. 243, 16-22 (1991)

[113] Jahoda, Keith et al.
Cross-Correlation of the X-Ray Background with Nearby Galaxies
The Astrophysical Journal, vol. 378, L37 (1991)
DOI: 10.1086/186136

[114] Shanks, T. et al.
The origin of the cosmic X-ray background
Nature, vol. 353, 315-320 (1991)
DOI: 10.1038/353315a0

[115] Fabian, A. C. et al.
The origin of the X-ray background.
Annual Review of Astron and Astrophys, vol. 30, 429-456 (1992)
DOI: 10.1146/annurev.aa.30.090192.002241

[116] Comastri, A. et al.
The contribution of AGNs to the X-ray background.
Astronomy and Astrophysics, vol. 296, 1 (1995)

[117] Zdziarski, Andrzej A.
Contributions of AGNs and SNe IA to the cosmic X-ray and gamma-ray backgrounds
Monthly Notices of the Royal Astronomical Society, vol. 281, L9 (1996)
DOI: 10.1093/mnras/281.1.L9

[118] Br et al.
Deep Extragalactic X-Ray Surveys
Annual Review of Astron and Astrophys, vol. 43, 827-859 (2005)
DOI: 10.1146/annurev.astro.43.051804.102213

[119] Cappelluti, N. et al.
The nature of the unresolved extragalactic cosmic soft X-ray background

Monthly Notices of the Royal Astronomical Society, vol. 427, 651-663 (2012)
DOI: 10.1111/j.1365-2966.2012.21867.x

[120] Helgason, K. et al.
Sources to the Spatial Coherence in the Unresolved Cosmic Near-infrared and X-Ray Backgrounds
The Astrophysical Journal, vol. 785, 38 (2014)
DOI: 10.1088/0004-637X/785/1/38

[121] Cappelluti, Nico et al.
The Chandra COSMOS Legacy Survey: Energy Spectrum of the Cosmic X-Ray Background and Constraints on Undetected Populations
The Astrophysical Journal, vol. 837, 19 (2017)
DOI: 10.3847/1538-4357/aa5ea4

[122] Ma, Q. et al.
X-ray background and its correlation with the 21 cm signal
Monthly Notices of the Royal Astronomical Society, vol. 480, 26-34 (2018)
DOI: 10.1093/mnras/sty1806

[123] Penzias, A. A. et al.
A Measurement of Excess Antenna Temperature at 4080 Mc/s.
The Astrophysical Journal, vol. 142, 419-421 (1965)
DOI: 10.1086/148307

[124] Moskalenko, Igor V. et al.
Anisotropic Inverse Compton Scattering in the Galaxy
The Astrophysical Journal, vol. 528, 357-367 (2000)
DOI: 10.1086/308138

[125] Dar, Arnon et al.
Is the diffuse gamma background radiation generated by Galactic cosmic rays?
Monthly Notices of the Royal Astronomical Society, vol. 323, 391-401

(2001)
DOI: 10.1046/j.1365-8711.2001.04246.x

[126] Gruber, D. E. et al.
The Spectrum of Diffuse Cosmic Hard X-Rays Measured with HEAO 1
The Astrophysical Journal, vol. 520, 124-129 (1999)
DOI: 10.1086/307450

[127] Cumani, P. et al.
Background for a gamma-ray satellite on a low-Earth orbit
Experimental Astronomy, vol. 47, 273-302 (2019)
DOI: 10.1007/s10686-019-09624-0

[128] Rothschild, R. et al.
The cosmic X-ray experiment aboard HEAO-1.
Space Science Instrumentation, vol. 4, 269-301 (1979)

[129] Gehrels, N. et al.
The Compton Gamma Ray Observatory.
Astronomy and Astrophysicss, vol. 97, 5-12 (1993)

[130] Melia, Fulvio
High-Energy Astrophysics (2009)
ISBN-10: 0691140294

[131] Schönfelder, Volker
The Universe in Gamma Rays (2001)
ISBN-10: 3540678743

[132] Strong, Andrew W. et al.
Diffuse Continuum Gamma Rays from the Galaxy
The Astrophysical Journal, vol. 537, 763-784 (2000)
DOI: 10.1086/309038

[133] Fichtel, C. E. et al.
High-energy gamma-ray results from the second Small Astronomy Satellite.
The Astrophysical Journal, vol. 198, 163-182 (1975)
DOI: 10.1086/153590

[134] Fichtel, C. E. et al.
Tabulated data from the SAS-2 high energy gamma ray telescope
197

[135] Bertsch, D. L. et al.
Diffuse Gamma-Ray Emission in the Galactic Plane from Cosmic-Ray, Matter, and Photon Interactions
The Astrophysical Journal, vol. 416, 587 (1993)
DOI: 10.1086/173261

[136] Kraushaar, W. L. et al.
High-Energy Cosmic Gamma-Ray Observations from the OSO-3 Satellite
The Astrophysical Journal, vol. 177, 341 (1972)
DOI: 10.1086/151713

[137] Mayer-Hasselw et al.
Large-scale distribution of galactic gamma radiation observed by COS-B
Astronomy and Astrophysics, vol. 105, 164-175 (1982)

[138] Krivonos, R. et al.
Hard X-ray emission from the Galactic ridge
Astronomy and Astrophysics, vol. 463, 957-967 (2007)
DOI: 10.1051/0004-6361:20065626

[139] Porter, Troy A. et al.
Inverse Compton Origin of the Hard X-Ray and Soft Gamma-Ray Emission from the Galactic Ridge
The Astrophysical Journal, vol. 682, 400-407 (2008)

DOI: 10.1086/589615

[140] Bouchet, L. et al.
INTEGRAL SPI All-Sky View in Soft Gamma Rays: A Study of Point-Source and Galactic Diffuse Emission
The Astrophysical Journal, vol. 679, 1315-1326 (2008)
DOI: 10.1086/529489

[141] Krivonos, R. et al.
INTEGRAL/IBIS 7-year All-Sky Hard X-ray Survey. I. Image reconstruction
Astronomy and Astrophysics, vol. 519, A107 (2010)
DOI: 10.1051/0004-6361/200913814

[142] Krivonos, R. et al.
INTEGRAL 11-year hard X-ray survey above 100 keV
Monthly Notices of the Royal Astronomical Society, vol. 448, 3766-3774 (2015)
DOI: 10.1093/mnras/stv150

[143] Hunter, S. D. et al.
EGRET Observations of the Diffuse Gamma-Ray Emission from the Galactic Plane
The Astrophysical Journal, vol. 481, 205-240 (1997)
DOI: 10.1086/304012

[144] Strong, A. W. et al.
COMPTEL Skymapping: a New Approach Using Parallel Computing
Astrophysical Letters and Communications, vol. 39, 209 (1999)

[145] Strong, Andrew W. et al.
Diffuse Galactic Continuum Gamma Rays: A Model Compatible with EGRET Data and Cosmic-Ray Measurements
The Astrophysical Journal, vol. 613, 962-976 (2004)
DOI: 10.1086/423193

[146] Prantzos, N. et al.
The 511 keV emission from positron annihilation in the Galaxy
Reviews of Modern Physics, vol. 83, 1001-1056 (2011)
DOI: 10.1103/RevModPhys.83.1001

[147] Strong, A. W.
Interstellar Gamma Rays and Cosmic Rays:. New Insights from Fermi-Lat and Integral
Cosmic Rays for Particle and Astroparticle Physics (2011)
DOI: 10.1142/9789814329033_0059

[148] Abdo, A. A. et al.
Spectrum of the Isotropic Diffuse Gamma-Ray Emission Derived from First-Year Fermi Large Area Telescope Data
Physical Review Letters, vol. 104, 101101 (2010)
DOI: 10.1103/PhysRevLett.104.101101

[149] Ajello, M. et al.
Fermi-LAT Observations of High-Energy Gamma-Ray Emission toward the Galactic Center
The Astrophysical Journal, vol. 819, 44 (2016)
DOI: 10.3847/0004-637X/819/1/44

[150] Revnivtsev, M. et al.
Origin of the Galactic ridge X-ray emission
Astronomy and Astrophysics, vol. 452, 169-178 (2006)
DOI: 10.1051/0004-6361:20054268

[151] Oh, Kyuseok et al.
The 105-Month Swift-BAT All-sky Hard X-Ray Survey
The Astrophysical Journals Supplement, vol. 235, 4 (2018)
DOI: 10.3847/1538-4365/aaa7fd

[152] van Allen, J. A.
Observation of high intensity radiation by satellites 1958 alpha and gamma
Journal of Jet Propulsion, vol. 28, 588-592 (1958)

DOI: 10.2514/8.739

[153] Svertilov, S. I. et al.
Wide-Field Gamma-Spectrometer BDRG: GRB Monitor On-Board the Lomonosov Mission
Space Science Reviews, vol. 214, 8 (2018)
DOI: 10.1007/s11214-017-0442-9

[154] Panasyuk, M. I. et al.
Complete set of detectors for studying cosmic gamma-ray bursts onboard the Lomonosov satellite
Physics of Particles and Nuclei, vol. 49, 109-112 (2018)
DOI: 10.1134/S1063779618010306

[155] Vette, James I.
The AE-8 trapped electron model environment
1991

[156] Vette, James I.
Trapped Radiation Environment Model Program (1964-1991)
1991

[157] Sawyer, D. M. et al.
Trapped Proton Environment for Solar Maximum and Solar Minimum
1976

[158] Vampola, A. L.
The ESA Outer Zone Electron Model Update
Environment Modeling for Space-Based Applications, ESA Special Publication (1996)

[159] Heynderickx, D. et al.
A low altitude trapped proton model for solar minimum conditions based on SAMPEX/PET data
IEEE Transactions on Nuclear Science, vol. 46, 1475-1480 (1999)

DOI: 10.1109/23.819110

[160] Ginet, G. P. et al.
AE9, AP9 and SPM: New Models for Specifying the Trapped Energetic Particle and Space Plasma Environment
Space Science Reviews, vol. 179, 579-615 (2013)
DOI: 10.1007/s11214-013-9964-y

[161] Johnston, W. R. et al.
AE9/AP9/SPM: new models for radiation belt and space plasma specification
Proceedings of the SPIE, Society of Photo-Optical Instrumentation Engineers (SPIE) Conference Series (2014)
DOI: 10.1117/12.2049836

[162] Johnston, W. Robert et al.
Recent Updates to the AE9/AP9/SPM Radiation Belt and Space Plasma Specification Model
IEEE Transactions on Nuclear Science, vol. 62, 2760-2766 (2015)
DOI: 10.1109/TNS.2015.2476470

[163] O'Brien, T. P. et al.
Changes in AE9/AP9-IRENE Version 1.5
IEEE Transactions on Nuclear Science, vol. 65, 462-466 (2018)
DOI: 10.1109/TNS.2017.2771324

[164] Ginet, Gregory P. et al.
Proton Flux Anisotropy in Low Earth Orbit
IEEE Transactions on Nuclear Science, vol. 54, 1975-1980 (2007)
DOI: 10.1109/TNS.2007.910041

[165] Alcaraz, J. et al.
Protons in near earth orbit
Physics Letters B, vol. 472, 215-226 (2000)
DOI: 10.1016/S0370-2693(99)01427-6

[166] Alcaraz, J. et al.
Leptons in near earth orbit
Physics Letters B, vol. 484, 10-22 (2000)
DOI: 10.1016/S0370-2693(00)00588-8

[167] Sanuki, T. et al.
Precise Measurement of Cosmic-Ray Proton and Helium Spectra with the BESS Spectrometer
The Astrophysical Journal, vol. 545, 1135-1142 (2000)
DOI: 10.1086/317873

[168] Yoon, Y. S. et al.
Cosmic-ray Proton and Helium Spectra from the First CREAM Flight
The Astrophysical Journal, vol. 728, 122 (2011)
DOI: 10.1088/0004-637X/728/2/122

[169] Ackermann, M. et al.
Fermi LAT observations of cosmic-ray electrons from 7 GeV to 1 TeV
Physical Review D, vol. 82, 092004 (2010)
DOI: 10.1103/PhysRevD.82.092004

[170] Ackermann, M. et al.
γ-Ray Observations of Earth's Limb
Physical Review Letters, vol. 112, 151103 (2014)
DOI: 10.1103/PhysRevLett.112.151103

[171] Aharonian, F. et al.
Energy Spectrum of Cosmic-Ray Electrons at TeV Energies
Physical Review Letters, vol. 101, 261104 (2008)
DOI: 10.1103/PhysRevLett.101.261104

[172] Martucci, M. et al.
Proton Fluxes Measured by the PAMELA Experiment from the Minimum to the Maximum Solar Activity for Solar Cycle 24
The Astrophysical Journal Letters, vol. 854, L2 (2018)
DOI: 10.3847/2041-8213/aaa9b2

[173] Space environment (natural and artificial) - Galactic cosmic ray model
2004

[174] Smart, D. F. et al.
A review of geomagnetic cutoff rigidities for earth-orbiting spacecraft
Advances in Space Research, vol. 36, 2012-2020 (2005)
DOI: 10.1016/j.asr.2004.09.015

[175] VanZ et al.
Magnetic apex coordinates: A magnetic coordinate system for the ionospheric F 2 layer
Journal of Geophysical Research, vol. 77, 2406 (1972)
DOI: 10.1029/JA077i013p02406

[176] Webber, W. R.
Cosmic ray electrons and positrons - A review of current measurements and some implications
NATO Advanced Science Institutes (ASI) Series C, NATO Advanced Science Institutes (ASI) Series C (1983)

[177] Moskalenko, I. V. et al.
Production and Propagation of Cosmic-Ray Positrons and Electrons
The Astrophysical Journal, vol. 493, 694-707 (1998)
DOI: 10.1086/305152

[178] Golden, R. L. et al.
Observations of Cosmic-Ray Electrons and Positrons Using an Imaging Calorimeter
The Astrophysical Journal, vol. 436, 769 (1994)
DOI: 10.1086/174951

[179] Jursa, Adolph S.
Handbook of geophysics and the space environment
1985

[180] Bidoli, V. et al.
Energy spectrum of secondary protons above the atmosphere measured by the instruments NINA and NINA-2
Annales Geophysicae, vol. 20, 1693 (2002)

[181] McIlwain, Carl E.
Coordinates for Mapping the Distribution of Magnetically Trapped Particles
Journal of Geophysical Research, vol. 66, 3681-3691 (1961)
DOI: 10.1029/JZ066i011p03681

[182] Atwood, W. B. et al.
The Large Area Telescope on the Fermi Gamma-Ray Space Telescope Mission
The Astrophysical Journal, vol. 697, 1071 (2009)
DOI: 10.1088/0004-637X/697/2/1071

[183] Zuccon, P. et al.
A Calculation of the Radiation Environment for Satellite Experiments Operating below the Van Allen Belts
Proceedings of the 28th International Cosmic Ray Conference (2003)

[184] Voronov, S. A. et al.
Energy spectra of high-energy electrons and positrons under the earth's radiation belt
Kosmicheskie Issledovaniia, vol. 29, 567 (1991)

[185] Mikhailov, V. V.
Low Energy Electron and Positron Spectra in the Earth Orbit Measured by Maria-2 Instrument
International Journal of Modern Physics A, vol. 17, 1695-1704 (2002)
DOI: 10.1142/S0217751X02011199

[186] Thompson, D. J.
A three-dimensional study of 30- to 300-MeV atmospheric gamma rays
Journal of Geophysical Research, vol. 79, 1309-1320 (1974)

DOI: 10.1029/JA079i010p01309

[187] Gurian, Iu. A. et al.
Investigation of hard gamma radiation of the atmosphere on Cosmos 461.
Geomagnetism and Aeronomy, vol. 19, 11-17 (1979)

[188] Ryan, J. M. et al.
Atmospheric gamma-ray angle and energy distributions from sea level to 3.5 g/cm^2 and 2 to 25 MeV
Journal of Geophysical Research, vol. 84, 5279-5288 (1979)
DOI: 10.1029/JA084iA09p05279

[189] Akyüz, A. et al.
Atmospheric gamma rays at geomagnetic latitudes of -29° and +43°
Journal of Geophysical Research, vol. 102, 17,359-17,364 (1997)
DOI: 10.1029/97JA01147

[190] Petry, Dirk
The Earth's Gamma-ray Albedo as observed by EGRET
High Energy Gamma-Ray Astronomy, American Institute of Physics Conference Series (2005)
DOI: 10.1063/1.1878488

[191] Abdo, A. A. et al.
Fermi large area telescope observations of the cosmic-ray induced γ-ray emission of the Earth's atmosphere
Physical Review D, vol. 80, 122004 (2009)
DOI: 10.1103/PhysRevD.80.122004

[192] Imhof, W. L. et al.
High-Resolution Measurements of Atmospheric Gamma Rays from a Satellite
Journal of Geophysical Research, vol. 81, 2835 (1976)
DOI: 10.1029/JA081i016p02835

[193] Sazonov, S. et al.
Hard X-ray emission of the Earth's atmosphere: Monte Carlo simulations
Monthly Notices of the Royal Astronomical Society, vol. 377, 1726-1736 (2007)
DOI: 10.1111/j.1365-2966.2007.11746.x

[194] Ait-Ouamer, Farid et al.
Atmospheric neutrons at 8.5-GV cutoff in the southern hemisphere
Journal of Geophysical Research, vol. 93, 2499-2510 (1988)
DOI: 10.1029/JA093iA04p02499

[195] Morris, D. J. et al.
Neutron measurements in near-Earth orbit with COMPTEL
Journal of Geophysical Research, vol. 100, 12243-12250 (1995)
DOI: 10.1029/95JA00475

[196] Lei, F. et al.
An Atmospheric Radiation Model Based on Response Matrices Generated by Detailed Monte Carlo Simulations of Cosmic Ray Interactions
IEEE Transactions on Nuclear Science, vol. 51, 3442-3451 (2004)
DOI: 10.1109/TNS.2004.839131

[197] Lei, F. et al.
Improvement to and Validations of the QinetiQ Atmospheric Radiation Model (QARM)
IEEE Transactions on Nuclear Science, vol. 53, 1851-1858 (2006)
DOI: 10.1109/TNS.2006.880567

[198] Armstrong, T. W. et al.
Predictions of induced radioactivity for spacecraft in low Earth orbit
International Journal of Radiation Applications and Instrumentation. Part D. Nuclear Tracks and Radiation Measurements, vol. 20, 101-130 (1992)
DOI: 10.1016/1359-0189(92)90089-E

[199] Fioretti, V. et al.
The low Earth orbit radiation environment and its impact on the prompt background of hard x-ray focusing telescopes
Proceedings of the SPIE, Society of Photo-Optical Instrumentation Engineers (SPIE) Conference Series (2012)
DOI: 10.1117/12.926248

[200] Torigoe, Kento et al.
Performance study of a large CsI(Tl) scintillator with an MPPC readout for nanosatellites used to localize gamma-ray bursts
Nuclear Instruments and Methods in Physics Research A, vol. 924, 316-320 (2019)
DOI: 10.1016/j.nima.2018.08.039

[201] Poole, C. M. et al.
A CAD Interface for GEANT4
Australasian Physical & Engineering Science in Medicine, vol. 35, 329-334 (2012)
DOI: 10.1007/s13246-012-0159-8

[202] Sullivan, J. D.
Geometrical factor and directional response of single and multi-element particle telescopes
Nuclear Instruments and Methods, vol. 95, 5-11 (1971)
DOI: 10.1016/0029-554X(71)90033-4

[203] Si, Hang
TetGen, a Delaunay-Based Quality Tetrahedral Mesh Generator
ACM Trans. on Mathematical Software, vol. 41, 11 (2015)
DOI: 10.1145/262969

[204] Feroci, Marco et al.
In-flight performances of the BeppoSAX gamma-ray burst monitor
EUV, X-Ray, and Gamma-Ray Instrumentation for Astronomy VIII, Society of Photo-Optical Instrumentation Engineers (SPIE) Conference Series (1997)
DOI: 10.1117/12.283768

[205] L. Band, David
A Gamma-Ray Burst Trigger Tool Kit
The Astrophysical Journal, vol. 578, 806-811 (2002)
DOI: 10.1086/342661

[206] Fenimore, E. E. et al.
The HETE Triggering Algorithm
Gamma-ray Bursts in the Afterglow Era (2001)
DOI: 10.1007/10853853_108

[207] Fenimore, E. E. et al.
The Trigger Algorithm for the Burst Alert Telescope on Swift
Gamma-Ray Burst and Afterglow Astronomy 2001: A Workshop Celebrating the First Year of the HETE Mission, American Institute of Physics Conference Series (2003)
DOI: 10.1063/1.1579409

[208] Feroci, M. et al.
SuperAGILE: The hard X-ray imager for the AGILE space mission
Nuclear Instruments and Methods in Physics Research A, vol. 581, 728-754 (2007)
DOI: 10.1016/j.nima.2007.07.147

[209] Fuschino, F. et al.
Search of GRB with AGILE Minicalorimeter
Nuclear Instruments and Methods in Physics Research A, vol. 588, 17-21 (2008)
DOI: 10.1016/j.nima.2008.01.004

[210] Smith, D. M. et al.
The RHESSI Spectrometer
Solar Physics, vol. 210, 33-60 (2002)
DOI: 10.1023/A:1022400716414

[211] M. Kokubun et al.
Activation of the ASTRO-E hard X-ray detector in low Earth orbit
IEEE Transactions on Nuclear Science, vol. 46, 371-376 (1999)

DOI: 10.1109/23.775546

[212] Gruber, D. E. et al.
Radioactivity observed in scintillation counters during the HEAO-1 mission
High-Energy Radiation Background in Space, American Institute of Physics Conference Series (1989)
DOI: 10.1063/1.38182

[213] Meegan, Charles et al.
The Fermi Gamma-ray Burst Monitor
The Astrophysical Journal, vol. 702, 791-804 (2009)
DOI: 10.1088/0004-637X/702/1/791

[214] Goldstein, Adam
The Importance of Fermi GBM in the Era of Gravitational-Wave Astronomy
AAS/High Energy Astrophysics Division, AAS/High Energy Astrophysics Division (2019)

[215] Collazzi, A. C. et al.
The Five Year Fermi/GBM Magnetar Burst Catalog
The Astrophysical Journal Supplement Series, vol. 218, 11 (2015)
DOI: 10.1088/0067-0049/218/1/11

[216] Ostgaard, N. et al.
First 10 Months of TGF Observations by ASIM
Journal of Geophysical Research (Atmospheres), vol. 124, 14,024-14,036 (2019)
DOI: 10.1029/2019JD031214

[217] Ostgaard, N. et al.
The ASIM Mission on the International Space Station
Space Science Revi, vol. "215", 26 (2019)
DOI: 10.1007/s11214-019-059

[218] Pendleton, Geoffrey N. et al.
The Intensity Distribution for Gamma-Ray Bursts Observed with BATSE
The Astrophysical Journal, vol. 464, 606 (1996)
DOI: 10.1086/177349

[219] Paciesas, William S. et al.
The Fourth BATSE Gamma-Ray Burst Catalog (Revised)
The Astrophysical Journal Supplement Series, vol. 122, 465-495 (1999)
DOI: 10.1086/313224

[220] Pendleton, G. N. et al.
The BATSE trigger efficiency as a function of intensity and energy range
Gamma-Ray Bursts, 4th Hunstville Symposium, American Institute of Physics Conference Series (1998)
DOI: 10.1063/1.55417

[221] Galgoczi, G. et al.
A software toolkit to simulate activation background for high energy detectors onboard satellites
Space Telescopes and Instrumentation 2020
Ultraviolet to Gamma Ray, vol. 11444 (2020)
DOI: 10.1117/12.2560829

[222] Evangelista, Y. et al.
The scientific payload on-board the HERMES-TP and HERMES-SP CubeSat missions
Space Telescopes and Instrumentation 2020
Ultraviolet to Gamma Ray, vol. 11444 (2020)
DOI: 10.48550/arXiv.2101.03032

[223] Odaka, H. et al.
Modeling of proton-induced radioactivation background in hard X-ray telescopes: Geant4-based simulation and its demonstration by Hitomi's measurement in a low Earth orbit
NIM A, vol. 891, 0920105 (2018)

DOI: 10.1016/j.nima.2018.02.071

[224] Bateman, H.
The solution of a system of differential equations occurring in the theory of radioactive transformations
Proc. Cambridge Philos. Soc., vol. 15., 423427 (1910)

[225] Sakano, M. et al.
Estimating the radiative activation characteristics of a Gd3Al2Ga3O12:Ce scintillator in low earth orbit
Journal of Instrumentation, vol. 9, 10003 (2014)
DOI: 10.1088/1748-0221/9/10/P10003

[226] Campana, R. et al.
The HERMES background and response simulations
Society of Photo-Optical Instrumentation Engineers (SPIE) Conference Series, vol. 11444 (2020)
DOI: 10.1117/12.2560365

[227] Walsh, B. M. et al.
Energetic particle impact on X-ray imaging with XMM-Newton
Space Weather, vol. 12, 387-394 (2014)
DOI: 10.1002/2014SW001046

[228] Salvetti, David et al.
A systematic analysis of the XMM-Newton background: II. Properties of the in-Field-Of-View excess component
Experimental Astronomy, vol. 44, 309-320 (2017)
DOI: 10.1007/s10686-017-9539-0

[229] Ghizzardi, Simona et al.
A systematic analysis of the XMM-Newton background: III. Impact of the magnetospheric environment
Experimental Astronomy, vol. 44, 273-285 (2017)
DOI: 10.1007/s10686-017-9554-1

[230] Kuntz, K. D. et al.
The EPIC-MOS particle-induced background spectra
A&A, vol. 478, 575-596 (2008)
DOI: 10.1051/0004-6361:20077912

[231] Elena A. Kronberg et al.
Prediction and Understanding of Soft-proton Contamination in XMM-Newton: A Machine Learning Approach
The Astrophysical Journa, vol. 903, 89 (2020)
DOI: 10.3847/1538-4357/abbb8f

[232] Marcos Bavdaz et al.
SPIE proceeding (2021)
DOI: 10.1117/12.2594689

[233] Maximilien J. Collon et al.
Silicon pore optics development for ATHENA
SPIE proceeding (2015)
DOI: 10.1117/12.2188988

[234] Fioretti, Valentina et al.
Magnetic Shielding of Soft Protons in Future X-Ray Telescopes: The Case of the ATHENA Wide Field Imager
The Astrophysical Journal, vol. 867, 9 (2018)
DOI: 10.3847/1538-4357/aade99

[235] Fioretti, Valentina et al.
Magnetic Shielding of Soft Protons in Future X-Ray Telescopes: The Case of the ATHENA Wide Field Imager
The Astrophysical Journal, vol. 867, 9 (2018)
DOI: 10.3847/1538-4357/aade99

[236] M. Laurenza et al.
Estimation of the Particle Radiation Environment at the L1 Point and in Near-Earth Space
The Astrophysical Journal, vol. 873, 112 (2019)

DOI: 10.3847/1538-4357/ab0410

[237] Budjas, Dusan et al.
Soft Proton Fluxes in and Around the Earth's Magnetotail
IEEE Transactions on Plasma Science, vol. 45, 1965-1971 (2017)
DOI: 10.1109/TPS.2017.2672202

[238] Ferreira, Ivo et al.
Design of the charged particle diverter for the ATHENA mission
Space Telescopes and Instrumentation 2018: Ultraviolet to Gamma Ray, Society of Photo-Optical Instrumentation Engineers (SPIE) Conference Series (2018)
DOI: 10.1117/12.2312226

[239] von Kienlin, Andreas et al.
Evaluation of the ATHENA/WFI instrumental background
Space Telescopes and Instrumentation 2018: Ultraviolet to Gamma Ray, Society of Photo-Optical Instrumentation Engineers (SPIE) Conference Series (2018)
DOI: 10.1117/12.2311987

[240] V. Fioretti et al.
Athena Charged Particle Diverter (CPD) scientific assessment: preliminary results on the WFI residual background
Internal document, from Athena Background Topical Panel (2021)

[241] Nandra, Karpal et al.
The Hot and Energetic Universe: A White Paper presenting the science theme motivating the Athena+ mission
ArXiv e-prints (2013)
DOI: 10.48550/ARXIV.1306.2307

[242] Allison, J. et al.
Geant4 developments and applications
IEEE Transactions on Nuclear Science, vol. 53, 270-278
DOI: 10.1109/TNS.2006.86982

[243] S. Agostinelli et al.
Nuclear Instruments and Methods in Physics Research Section A: Accelerators, Spectrometers, Detectors and Associated Equipment, vol. 506, 250-303 (2003)
DOI: 10.1016/S0168-9002(03)01368-8

[244] S. Agostinelli et al.
Nuclear Instruments and Methods in Physics Research Section A: Accelerators, Spectrometers, Detectors and Associated Equipment, vol. 506, 250-303 (2003)
DOI: 10.1016/S0168-9002(03)01368-8

[245] Fioretti, Valentina et al.
Geant4 simulations of soft proton scattering in X-ray optics
Experimental Astronomy, vol. 44, 413–435 (2017)
DOI: 10.1007/s10686-017-9559-9

[246] Galgoczi, G. et al.
Geant4 simulation of the residual background in the ATHENA Wide Field Imager from protons deflected by the Charged Particle Diverter
Astronomical Telescopes + Instrumentation (2022)
DOI: 10.1117/12.2629994

[247] Scattering efficiencies measurements of soft protons at grazing incidence from an Athena Silicon Pore
Roberta, Amato et al.
Experimental Astronom, vol. 52, 109–123 (2021)
DOI: 10.1007/s10686-021-09806-9

[248] Breuer, J.P. et al.
Athena charged particle diverter simulations: effects of micro-roughness on proton scattering using Geant4
Astronomical Telescopes + Instrumentation (2022)
DOI: 10.1117/12.2630076

[249] Peggs, S. et al.
ESS Technical Design Report

ESS 2013-001
ISBN: 9789198017328

[250] R. Garoby et al.
The European Spallation Source Design
Physica Scripta,vol. 93, 014001 (2018)
DOI: 10.1088/14024896/aa9bff

[251] Wacklin, H.
FREIA: Reflectometer concept for fast kinetics at ESS - ESS instrument proposal (2014)

[252] Stahn, J.
Estia: A truly focusing reflectometer." ESS instrument proposal (2014)

[253] Stahn, J. et al.
Focusing specular neutron reflectometry for small samples
Eur. Phys. J. Appl. Phys. vol 58. (2012)
DOI: 10.1051/epjap/2012110295

[254] Shea, D. A. et al.
The Helium-3 Shortage: Supply, Demand, and Options
Congress. Congressional Research Service (2010)

[255] Kirstein, O. et al.
Neutron Position Sensitive Detectors for the ESS
PoS (Vertex 2014) (2014)
DOI: https://doi.org/10.22323/1.227.0029

[256] Stefanescu, I. et al.
A ^{10}B-based neutron detector with stacked MultiWire Proportional Counters and macrostructured cathodes
JINST, vol. 8, 12003 (2013)
DOI:10.1088/1748-0221/8/12/P12003

[257] Lacy, J.L. et al.
The evolution of neutron straw detector applications in homeland security
IEEE Trans. Nucl. Sci. vol. 60, 1140 (2013)
DOI: 10.1109/TNS.2013.2248166

[258] Anastasopoulos, M. et al.
Multi-Grid Detector for Neutron Spectroscopy: Results Obtained on Time-of-Flight Spectrometer CNCS
JINST, vol. 12, 04030 (2017)
DOI: 10.1088/1748-0221/12/04/P04030

[259] Muraro, A. et al.
Performance of the high-efficiency thermal neutron BAND-GEM detector
Prog. Theor. Exp. Phys. 023H01 (2018)
DOI: 10.1093/ptep/pty005

[260] Margato, L. M. S. et al.
Boron-10 lined RPCs for sub-millimeter resolution thermal neutron detectors: conceptual design and performance considerations
JINST, vol. 13, 08007 (2018)
DOI: 10.1088/1748-0221/13/08/P08007

[261] Sykora, J. et al.
ZnO:Zn/^{6}LiF scintillator—A low afterglow alternative to ZnS:Ag/^{6}LiF for thermal neutron detection
NIM A 883, 075082, (2018) DOI: 10.1016/j.nima.2017.11.052

[262] Sykora, J. et al.
Large area wavelength shifting fibre thermal neutron detectors using 64 channel flat panel PMTs
Conference paper in IEEE NSS MIC conference (2015)
DOI: 10.1109/NSSMIC.2015.7581838

[263] Wang, C. L. et al.
Wavelength-Shifting-Fiber Scintillation Detectors for Thermal Neutron

Imaging at SNS
IEEE Nuclear Science Symposium Conference Record (2011)
DOI:10.1109/NSSMIC.2011.6152489

[264] Jaksch, S. et al.
Recent Developments SoNDe High-Flux Detector Project
JPS, Proceedings of International Conference on Neutron Optics (NOP2017) vol. 22, 011019, (2017)
DOI: 10.7566/JPSCP.22.011019

[265] M. Katagiri, *Neutron detectors with scintillators using ZnS: Ag phosphor: Development summary*, *IEEE NSS, Anaheim* **He-2-2** (2012).

[266] Sakasai, K. et al.
Development of neutron detector for engineering materials diffractometer at J-PARC, NIM, vol. 600, 157160 (2009) DOI: 10.1016/j.nima.2008.11.023

[267] Meo, S. Lo et al.
Study of silicon+^{6}LiF thermal neutron detectors: Geant4 simulations versus real data
NIM A, vol. 886, 048057 (2017)
DOI: 10.1016/j.nima.2017.04.029

[268] Piscitelli, F. et al. The Multi-Blade Boron-10-based neutron detector for high intensity neutron reflectometry at ESS
JINST, vol. 12, 03013 (2017)
DOI: 10.1088/1742-6596/513/2/022017

[269] Piscitelli, F. et al.
Multi-Blade 10B-based detector for neutron reflectometry at ESS: results obtained on the CRISP reflectometers at ISIS
IEEE Atlanta 2017 Conference Record (2017)

[270] Piscitelli, F.et al.
Analytical modeling of thin film neutron converters and its application

to thermal neutron gas detectors
JINST vol. 8, 04020 (2013)
DOI: 10.1088/1748-0221/8/04/P04020

[271] Buffet, J. C. et al.
Advances in detector for single crystal neutron diffraction
NIM A, vol. 554, 392405 (2005)
DOI: 10.1016/j.nima.2005.08.018

[272] Sauli, F. et al.
Principles of operation of multiwire proportional and drift chambers
Lectures given in the Academic Training Programme of CERN (1977)

[273] Galgóczi, G. et al.
Investigation of neutron scattering in the Multi-Blade detector with Geant4 simulations
JINST, vol. 13, 12031 (2018)
DOI: 10.1088/1748-0221/13/12/P12031

[274] Piscitelli, F. et al.
Neutron reflectometry on highly absorbing films and its application to 10B4C-based neutron detectors
Proceedings of the Royal Society A 472, vol. 2185, 03013 (2016)
DOI: 10.1098/rspa.2015.0711

[275] Kittelmann, T. et al.
Geant4 based simulations for novel neutron detector development, vol. 513, 022017 (2013)
DOI: 10.1088/1742-6596/513/2/022017

[276] Kanaki, K. et al.
Simulation tools for detector and instrument design
Physica B: Condensed Matter, vol. 551, 386389 (2018)
DOI: 10.1016/j.physb.2018.03.025

[277] Dian, E et al.
Scattered neutron background in thermal neutron detectors

NIM A, vol. 902, 173183 (2018)
DOI: 10.1016/j.nima.2018.04.055